Cell

Neutrophil profiling illuminates anti-tumor antigen-presenting potency

Graphical abstract

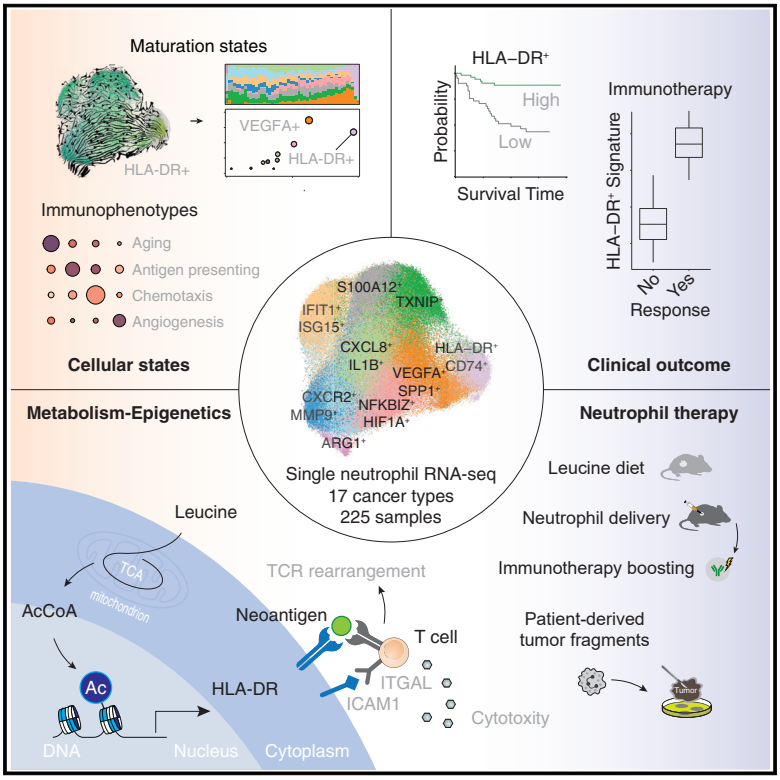

Highlights

- Neutrophils adopt 10 states across cancers, demonstrating tissue and phenotype plasticity
- Neutrophil maturation states span inflammation, angiogenesis, and antigen presentation
- Antigen-presenting program can be evoked by leucine and boosts T cell neoantigen response
- Delivering antigen-presenting neutrophils fuels immunotherapy and fine-tunes TME

Authors

Yingcheng Wu, Jiaqiang Ma, Xupeng Yang, ..., Jia Fan, Xiaoming Zhang, Qiang Gao

Correspondence

liyang_fudan@fudan.edu.cn (L.Y.), fan.jia@zs-hospital.sh.cn (J.F.), xmzhang@ips.ac.cn (X.Z.), gaoqiang@fudan.edu.cn (Q.G.)

In brief

Single-cell RNA sequencing analyses of neutrophils from 225 samples across 17 cancer types identify distinct clinically relevant transcriptional states. Metabolic analyses highlight the potential for delivery of leucine-activated antigen-presenting neutrophils in anti-tumor therapy.

Wu et al., 2024, Cell *187*, 1422–1439
March 14, 2024
https://doi.org/10.1016/j.cell.2024.02.005

CellPress

CellPress

Cell

Article

Neutrophil profiling illuminates anti-tumor antigen-presenting potency

Yingcheng Wu,[1,2,8] Jiaqiang Ma,[1,2,8] Xupeng Yang,[1,8] Fang Nan,[3,8] Tiancheng Zhang,[1,8] Shuyi Ji,[4] Dongning Rao,[1] Hua Feng,[3] Ke Gao,[1] Xixi Gu,[2] Shan Jiang,[2] Guohe Song,[1] Jiaomeng Pan,[1] Mao Zhang,[1] Yanan Xu,[1] Shu Zhang,[1] Yihui Fan,[5] Xiaoying Wang,[1] Jian Zhou,[1] Li Yang,[3,*] Jia Fan,[1,6,7,*] Xiaoming Zhang,[2,*] and Qiang Gao[1,6,7,9,*]

[1]Department of Liver Surgery and Transplantation and Key Laboratory of Carcinogenesis and Cancer Invasion, Ministry of Education, Liver Cancer Institute, Zhongshan Hospital, Fudan University, Shanghai 200032, China

[2]The Center for Microbes, Development and Health, Key Laboratory of Immune Response and Immunotherapy, Shanghai Institute of Immunity and Infection, Chinese Academy of Sciences, Shanghai 200031, China

[3]Center for Molecular Medicine, Children's Hospital of Fudan University and Shanghai Key Laboratory of Medical Epigenetics, International Laboratory of Medical Epigenetics and Metabolism, Ministry of Science and Technology, Institutes of Biomedical Sciences, Fudan University, Shanghai 200032, China

[4]Institute for Regenerative Medicine, Shanghai East Hospital, School of Life Sciences and Technology, Tongji University School of Medicine, Shanghai 200123, China

[5]Department of Pathogenic Biology and Basic Medical Research Center, School of Medicine, Nantong University, Nantong 226001, China

[6]Institutes of Biomedical Sciences, Fudan University, Shanghai 200032, China

[7]State Key Laboratory of Genetic Engineering, Fudan University, Shanghai 200433, China

[8]These authors contributed equally

[9]Lead contact

*Correspondence: liyang_fudan@fudan.edu.cn (L.Y.), fan.jia@zs-hospital.sh.cn (J.F.), xmzhang@ips.ac.cn (X.Z.), gaoqiang@fudan.edu.cn (Q.G.)

https://doi.org/10.1016/j.cell.2024.02.005

SUMMARY

Neutrophils, the most abundant and efficient defenders against pathogens, exert opposing functions across cancer types. However, given their short half-life, it remains challenging to explore how neutrophils adopt specific fates in cancer. Here, we generated and integrated single-cell neutrophil transcriptomes from 17 cancer types (225 samples from 143 patients). Neutrophils exhibited extraordinary complexity, with 10 distinct states including inflammation, angiogenesis, and antigen presentation. Notably, the antigen-presenting program was associated with favorable survival in most cancers and could be evoked by leucine metabolism and subsequent histone H3K27ac modification. These neutrophils could further invoke both (neo)antigen-specific and antigen-independent T cell responses. Neutrophil delivery or a leucine diet fine-tuned the immune balance to enhance anti-PD-1 therapy in various murine cancer models. In summary, these data not only indicate the neutrophil divergence across cancers but also suggest therapeutic opportunities such as antigen-presenting neutrophil delivery.

INTRODUCTION

Neutrophils are believed to be the cells that achieve the most rapid defense against pathogens.[1] They can sense diverse cancer signals, such as inflammation and wounding, to initiate the chemotaxis module toward the tumor microenvironment (TME).[2] However, human neutrophils are usually too short-lived to be profiled (half-life: 6–8 h),[3] rendering most single-cell RNA sequencing (scRNA-seq) approaches unable to achieve high-throughput profiling of these cells. Due to their lower mRNA content (neutrophils: 0.33 μg; macrophage and monocytes: 2.55 μg per million cells),[4] our understanding of the transcriptional diversity and spatiotemporal heterogeneity of human neutrophils remains rudimentary, despite the universal distribution of these cells across organs and tumors throughout the body.

In the field of cancer immunology, the paradox of whether neutrophils are generally suppressive or protective remains unresolved. Tumor-associated neutrophils are long believed to be immunosuppressive[5,6] and to exacerbate patient outcomes.[7–9] However, these cells were recently shown to kill cancer cells by releasing active elastase,[10] nitric oxide synthase,[11] or reactive oxygen species (ROS).[12] Alternatively, neutrophils also harbored anti-tumor immune phenotype that promotes autologous T cell responses[13] or interferon-related immunostimulatory effects.[14] These seemingly contradictory data raise critical but poorly understood questions around population composition and which subsets drive pro- or anti-tumor effects. Systematically decoding the cellular diversity of tumor-infiltrating neutrophils will identify their diverse gene expression patterns as well as their niche framework. In this context, single-cell profiling is uniquely suited for the characterization of neutrophil states and

provides the opportunity to create a data-driven map of neutrophil ontology.

To address this challenge, we here designed a neutrophil profiling strategy and generated the single neutrophil transcriptomes from 225 samples collected from 143 patients across 17 cancer types, including paired metastases from selected cancers. We found that neutrophils exhibit a complex and diverse transcriptional profile with 10 distinct cell states, among which three were potentially dominant across various cancer types, including inflammation, angiogenesis, and antigen presentation. In particular, antigen-presenting neutrophils showed unique immunophenotypes and metabolic features, which can induce T cell neoantigen reactivity. Our study not only generates cancer neutrophil transcriptomes but also unravels potential therapeutic opportunities such as antigen-presenting neutrophil delivery.

RESULTS

Neutrophils preferably infiltrate into certain cancer types

The extent of neutrophil infiltration into solid tumors varies widely,[15] but there still exists no consensus on the exact cancer types and infiltration level. To explore the infiltration patterns and choose the appropriate cancer types, we tested 8 common immune quantification algorithms and analyzed The Cancer Genome Atlas (TCGA) covering 8,766 samples across 31 solid cancers (STAR Methods). We developed a consensus neutrophil infiltration score based on three algorithms,[16–18] which revealed strong tissue-selective patterns of neutrophil infiltration that could be clustered into 3 subtypes (29.6% high, 30.0% heterogeneous, and 40.4% low; Figures 1A and S1A). For example, neutrophils show high infiltration in lung and kidney cancers and intermediate infiltration in gastrointestinal cancers, which was consistent in another pan-cancer dataset, Clinical Proteomic Tumor Analysis Consortium (CPTAC)[19] (Figures S1B and S1C). By comparing neutrophil levels among immune subtypes,[20,21] we observed preferential neutrophil infiltration in inflammatory or fibrotic suppressive TMEs (Figure 1B), in agreement with previously reported neutrophil infiltration patterns and functions.[15] Together, these data highlighted the diversity of neutrophil infiltration depending upon the tissue and cancer types, providing a basis for our subsequent neutrophil sampling strategy.

Following our initial findings, we devised a standardized sampling strategy focused on cancer types with high or medium neutrophil infiltration (sample statistics, Figure S1D), ensuring the inclusion of matched blood, adjacent normal tissues, and metastasis samples when available. Considering the short half-life and data quality, we further designed a neutrophil sorting protocol (Figure S1E) and an *in silico* strategy (STAR Methods). We successfully sequenced 103 samples from 64 patients that passed quality control (Table S1), including primary and metastatic samples as well as matched normal tissues and blood (STAR Methods). We further applied the standardized pipeline on published datasets and finally generated a neutrophil map of 225 samples from 143 patients across 17 cancer types, among which 12 cancer type data (70.59%) were newly generated or in-house (Figure 1C). After harmonizing the data batches, excluding the low-quality cells, and balancing the RNA dropouts, 1,79,908 single neutrophils finally passed quality control, of which 79.29% data were in-house or freshly released. Together, our single-cell profiling constitutes a potential resource for neutrophil investigation (available at http://www.pancancer.cn/neu/).

Transcriptional signatures across cancers

To decode the transcriptional signature, we clustered neutrophils and noted high heterogeneity across cancer and tissue types (Figures 1D and S1F). We observed 10 distinct states composed of S100A12$^+$, HLA-DR$^+$CD74$^+$, VEGFA$^+$SPP1$^+$, TXNIP$^+$, CXCL8$^+$IL1B$^+$, CXCR2$^+$, IFIT1$^+$ISG15$^+$, MMP9$^+$, NFKBIZ$^+$HIF1A$^+$, and ARG1$^+$ neutrophils (Figures 1E and 1F; Table S2). For example, HLA-DR$^+$CD74$^+$ subset showed high expression of major histocompatibility complex (MHC)-II molecules and universal infiltration across cancers. Conforming to the neutrophil biology,[15] we also identified clusters potentially representing inflammatory response (CXCL8$^+$IL1B$^+$) and specific chemotaxis (CXCR2$^+$) features (Figure 1F). By decoding neutrophil transcriptome into transcriptional programs (STAR Methods), we consistently confirmed their featured activation modes such as chemotaxis or inflammation (Figure S1G). Given the neutrophil single-cell profiles were only reported in certain cancer types, we computed the correlation with previously defined neutrophil states and subpopulations (STAR Methods) of 5 independent studies.[7,22–25] Some subsets of our data showed strong consistency with published states such as IFIT1$^+$ISG15$^+$ and hNeutro2 (Figure S1H). Together, our neutrophil map not only captured known neutrophil subpopulation features but also revealed potentially uncharacterized neutrophil subsets.

Molecular divergence and survival correlation

To explore the principles governing neutrophil clades, we computed the tree structure[26] and observed the scattered tree leaves of distinct subsets (Figure 2A). Based on Ro/e analysis (ratio of observed cell number to expected cell number) (Figure 2B), HLA-DR$^+$CD74$^+$ and VEGFA$^+$SPP1$^+$ neutrophils were the most cancer-enriched subsets overall (Figures 2B and S2A) but showed cancer type preferences. HLA-DR$^+$CD74$^+$ neutrophils were enriched in non-small cell lung cancer (NSCLC), bladder cancer (BLCA), and ovarian cancer (OV) while showing decreased infiltration in renal cell carcinoma (RCC) and oral squamous cell carcinoma (OSCC). In contrast, VEGFA$^+$SPP1$^+$ neutrophils showed sparse infiltration in NSCLC, BLCA, and OV but were enriched in RCC and stomach adenocarcinoma (STAD). These data were partly validated by flow cytometry (n = 24, see Table S1) and multiplex immunohistochemistry (mIHC) using an independent multi-cancer-TMA cohort (n = 68, see Table S1) comprising 8 cancer types, including breast invasive carcinoma (BRCA), colon adenocarcinoma (COAD), intrahepatic cholangiocarcinoma (ICC), hepatocellular carcinoma (HCC), STAD, NSCLC, RCC, and pancreatic adenocarcinoma (PAAD) (Figures 2C–2E and S2B).

To explore the association of neutrophil subsets with patient survival, we first analyzed the neutrophil subset signatures based on the TCGA pan-cancer dataset. Among the subsets,

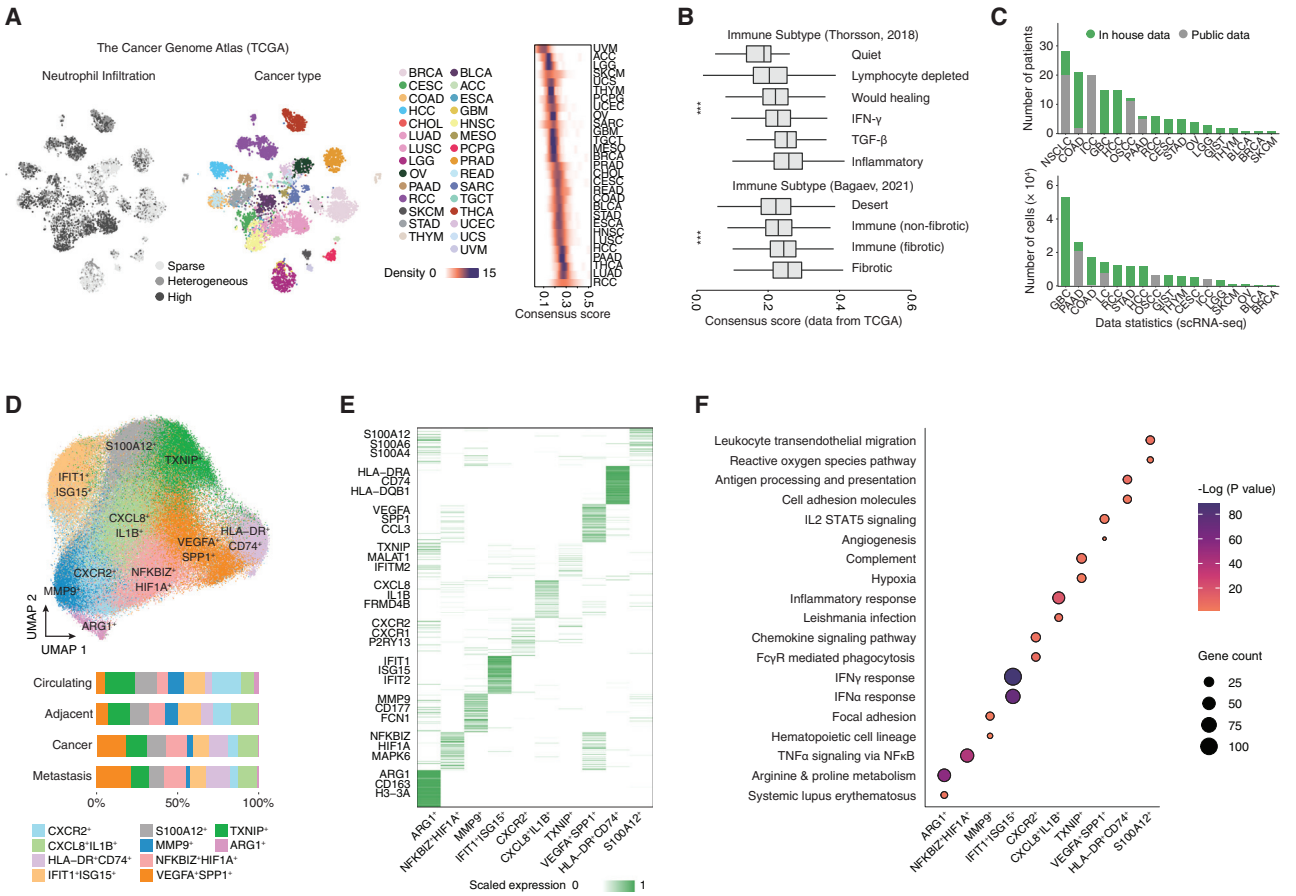

Figure 1. The generation of a pan-cancer single neutrophil atlas

(A) Neutrophil consensus infiltration level of pan-cancer samples (TCGA dataset), showing the neutrophil infiltration level (left), cancer types (middle), and ranked consensus score (right).

(B) Neutrophil consensus infiltration level according to immune subtypes (TCGA dataset).[20,21] ***$p < 0.001$; ANOVA test.

(C) Number of included patients and cells (green, in-house data; gray, public data). Healthy tissue controls were excluded.

(D) The UMAP plot (upper panel) and neutrophil proportion (lower panel).

(E) Gene expression heatmap (top 50 expressed) in neutrophil subsets.

(F) Enriched pathways of each neutrophil subset. The signature was from Kyoto Encyclopedia of Genes and Genomes (KEGG) and Hallmark databases.

See also Figure S1 and Tables S1 and S2.

VEGFA$^+$SPP1$^+$ subset was linked with the worst patient outcome (Figures 2F and S2C; 8-cancer-TMA cohort), whereas HLA-DR$^+$ was linked with the best. We further corroborated the prognostic relevance of HLA-DR$^+$ neutrophils through mIHC in an independent 8-cancer-TMA cohort (Figure 2G, n = 1,116; HCC, n = 357; COAD, n = 93; NSCLC, n = 90; STAD, n = 85; RCC, n = 150; OV, n = 160; BRCA, n = 129; BLCA, n = 52). These data indicated that HLA-DR$^+$ neutrophils may represent a key anti-tumor neutrophil subset across a majority of cancer types.

We next compared cytokine profiles of distinct neutrophil subsets (Figure 2H). HLA-DR$^+$CD74$^+$ neutrophils showed high CCL5, which can recruit T cells.[27] IFIT1$^+$ISG15$^+$ neutrophils were associated with high expression of PD-L1 (CD274), indicating its immunosuppressive role. Only HLA-DR$^+$CD74$^+$ neutrophils showed specific enrichment of MHC class II molecules such as HLA-DRA and HLA-DRB1 (Figure 2I). However, almost all neutrophil subsets expressed high levels of MHC class I molecules, aligning with their consensual expression on all nucleated cells.[28] In parallel, the immunophenotypic signature[29] of neutrophil subsets showed remarkable diversity (Figure 2J), whereas almost all subsets showed high aging signature, supporting the notion that tumor-associated neutrophils are mostly in a maturation state.[2] Reciprocally, we also identified the ubiquitous cell cycle gene expression among almost all subsets and the enrichment of interferon-related genes in IFIT1$^+$ISG15$^+$ neutrophils (Figure S2D). Given the known circadian features of neutrophil biology,[30,31] we further compared the phenotypic signatures sampled at different times of day and observed higher maturation and chemotaxis levels of neutrophils at daytime (Figure S2E). These data collectively highlighted the subset-specific molecular hallmark of neutrophils.

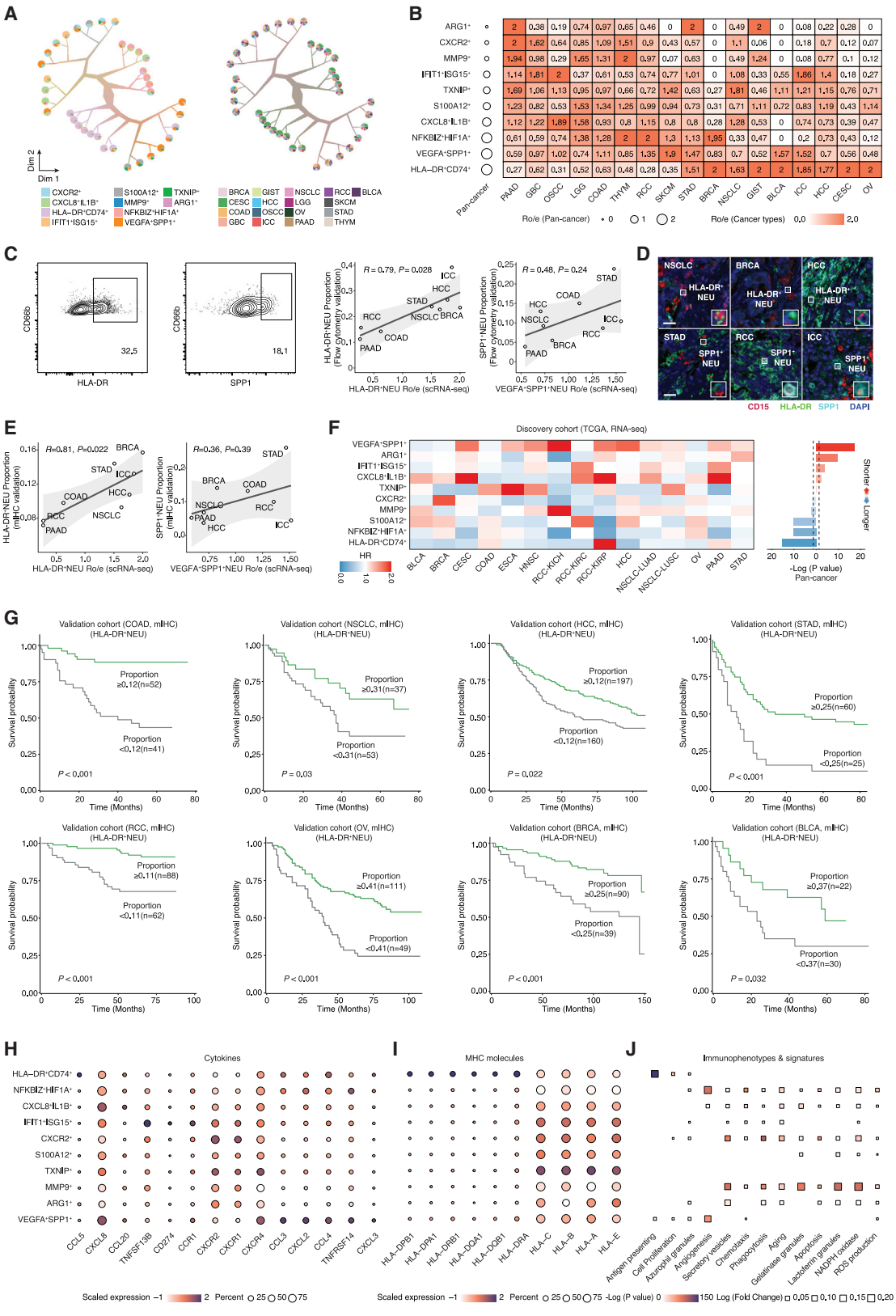

(legend on next page)

Given neutrophils' capacity against pathogens, we compared cell states between cancer and inflammatory conditions. As a result, IFIT1$^+$ISG15$^+$ neutrophils showed an expanded proportion in chronic pancreatitis and cholecystitis, which also exhibited high infiltration in pancreatic and gallbladder cancers (Figure S2F). Likewise, neutrophils in COVID-19 lung samples showed a specific spectrum of states, such as enrichment of inflammatory NFKBIZ$^+$HIF1A$^+$ subsets, which was also observed in lung cancer. This result may imply the shared tissue-restricted reprogramming across diverse disease conditions or a causal resemblance between inflammation and cancer in indicated organs. In contrast, certain subsets are highly tumor-specific (i.e., HLA-DR$^+$CD74$^+$ and VEGFA$^+$SPP1$^+$ subsets), indicating the TME-specific stimuli on reprogramming neutrophil states. Taken together, our data revealed the potential preference of neutrophil infiltration (i.e., HLA-DR$^+$CD74$^+$ and VEGFA$^+$SPP1$^+$ subsets) into certain cancer types and indicated the existence of cancer-imprinted transcriptional programs.

Maturation and metabolism states

Neutrophils have long been regarded as mature and terminally differentiated cells. However, it remains unknown how the diversity of their maturation states is achieved. To address this question, we applied a vector-field-based deep learning algorithm to infer the progressive steps of lineage specification and divergence.[32] We observed continuous differentiation along neutrophil states, with the most terminal pseudotime value observed for HLA-DR$^+$CD74$^+$ neutrophils (Figures 3A and S3A); this pattern was replicated by other algorithms, including monocle3,[33] CytoTRACE,[34] and Slingshot[35] (Figures 3A and S3A). We ranked neutrophils according to both their tumor specificity and pseudotime, finding that HLA-DR$^+$CD74$^+$ neutrophils potentially remained at the terminus (Figure 3B). To validate this finding, we first evaluated the maturation markers CD11b and CD16[36] using flow cytometry (Figure 3C) in intratumor neutrophils from 24 patients with 8 cancer types (Table S1). As a result, the HLA-DR$^+$ neutrophil subset showed significantly higher CD11b and CD16 expression. We subsequently confirmed the enhanced maturation markers' (CD11b and MPO)[36] expression in HLA-DR$^+$ neutrophils using mIHC across cancers (Figures 3D and 3E). Also, transcription factor RFX5 showed specific activation among the HLA-DR$^+$ subset, consistent with ChIP-seq and knockdown/overexpression assays (Figures S3B–S3E; STAR Methods). Taken together, these data indicated that HLA-DR$^+$ neutrophils were potentially one of the terminally mature neutrophil subsets.

A critical question is how pathway activity varies across tumor neutrophil subsets. To address this issue, we measured the pathway variance and observed the strong diversity of metabolic pathways (Figure S3F), which supports the potential metabolic regulation of neutrophil identity maintenance. Then, we quantified the metabolic pathway activity of the neutrophil subsets (Figures 3F and S3G; Table S3). Notably, HLA-DR$^+$ neutrophils showed remarkable enrichment of amino acid metabolism (i.e., valine, leucine, and isoleucine, Figure 3F). In parallel, the activation of vitamin metabolism and glycan metabolism were dominant among the immunosuppressive VEGFA$^+$SPP1$^+$ neutrophils. Together, these results supported the possibility that tumor neutrophils were metabolically coordinated, raising the idea that amino acid metabolism primes the HLA-DR programs.

Leucine metabolism governs the epigenetics of the antigen-presenting machinery

To systematically examine the effect of amino acids on neutrophils, we designed an *in vitro* screening strategy comprising all 20 amino acids and investigated their impact on antigen presentation (Figure 4A) in circulating neutrophils from healthy donors (STAR Methods). Particularly, leucine upregulated HLA-DR (Figure 4B) and costimulatory molecules such as CD80 (Figure 4C). Although arginine slightly upregulated HLA-DR, it cannot impact on costimulatory molecules (Figure S4A). We further expanded our analysis of leucine on the spectrum of antigen presentation processes by using PCR array analysis. Notably, leucine significantly promoted the gene expression of MHC-II complex assembly (Figure 4D), enhanced antigen processing protease (Figure 4E), and facilitated antigen-loading processes (Figure 4F). We confirmed that intracellular leucine levels did increase upon leucine treatment and that these effects were not due to contamination with other antigen-presenting cells (Figure S4B). RNA-seq analyses also confirmed the impact of leucine on MHC-II but not MHC-I (Figures 4G, S4C, and S4D). We also observed that leucine increased the *in vitro* survival of neutrophils

Figure 2. Molecular features and survival correlation of neutrophils

(A) Neutrophil tree structure according to cell subsets (left) and cancer types (right) using TooManyCells.[26]

(B) Neutrophil Ro/e (ratio of observed cell number to expected cell number) in different cancer types. The left dots represent the Ro/e of pan-cancer samples. The right heatmap represents the Ro/e in each cancer type. Ro/e > 2 was normalized to 2.

(C) The flow cytometry (first and second panel) and correlations between infiltration of HLA-DR$^+$ (third panel) or SPP1$^+$ neutrophil (fourth panel) based on scRNA-seq and flow cytometry. The y axis represents the proportion estimated by flow cytometry. Cells were gated on CD66b$^+$ cells. The x axis represents the neutrophil subset Ro/e estimated by scRNA-seq. n = 24.

(D) Imaging of HLA-DR$^+$ neutrophils in NSCLC, BRCA, and HCC (HLA-DR$^+$ neutrophil enriched cancer types) and SPP1$^+$ neutrophils in STAD, RCC, and ICC (SPP1$^+$ neutrophil enriched cancer types) using mIHC. Scale bars, 30 μm.

(E) Correlations between infiltration of HLA-DR$^+$ (left) or SPP1$^+$ neutrophil (right) based on scRNA-seq and mIHC. The y axis represents the proportion estimated by mIHC. The x axis represents the neutrophil subset Ro/e estimated by scRNA-seq. n = 68.

(F) The prognostic value of neutrophil signature (TCGA dataset), showing the hazard ratio value (left) and the −log (p value) of the neutrophil subset signature (right). The left and right sides of the x axis both represent positive values, as all −log (p value) are greater than zero.

(G) Survival analyses of HLA-DR$^+$CD15$^+$ neutrophil in 8-cancer-TMA cohort covering COAD, NSCLC, HCC, STAD, RCC, OV, BRCA, and BLCA using mIHC. Proportion of HLA-DR$^+$CD15$^+$ to CD15$^+$ cells was analyzed. p values were determined by log-rank test. For sample information, see Table S1.

(H–J) Expression profiles of differentially expressed cytokines (H), MHC molecules (I), immunophenotypes, and signatures (J).

See also Figure S2 and Table S1.

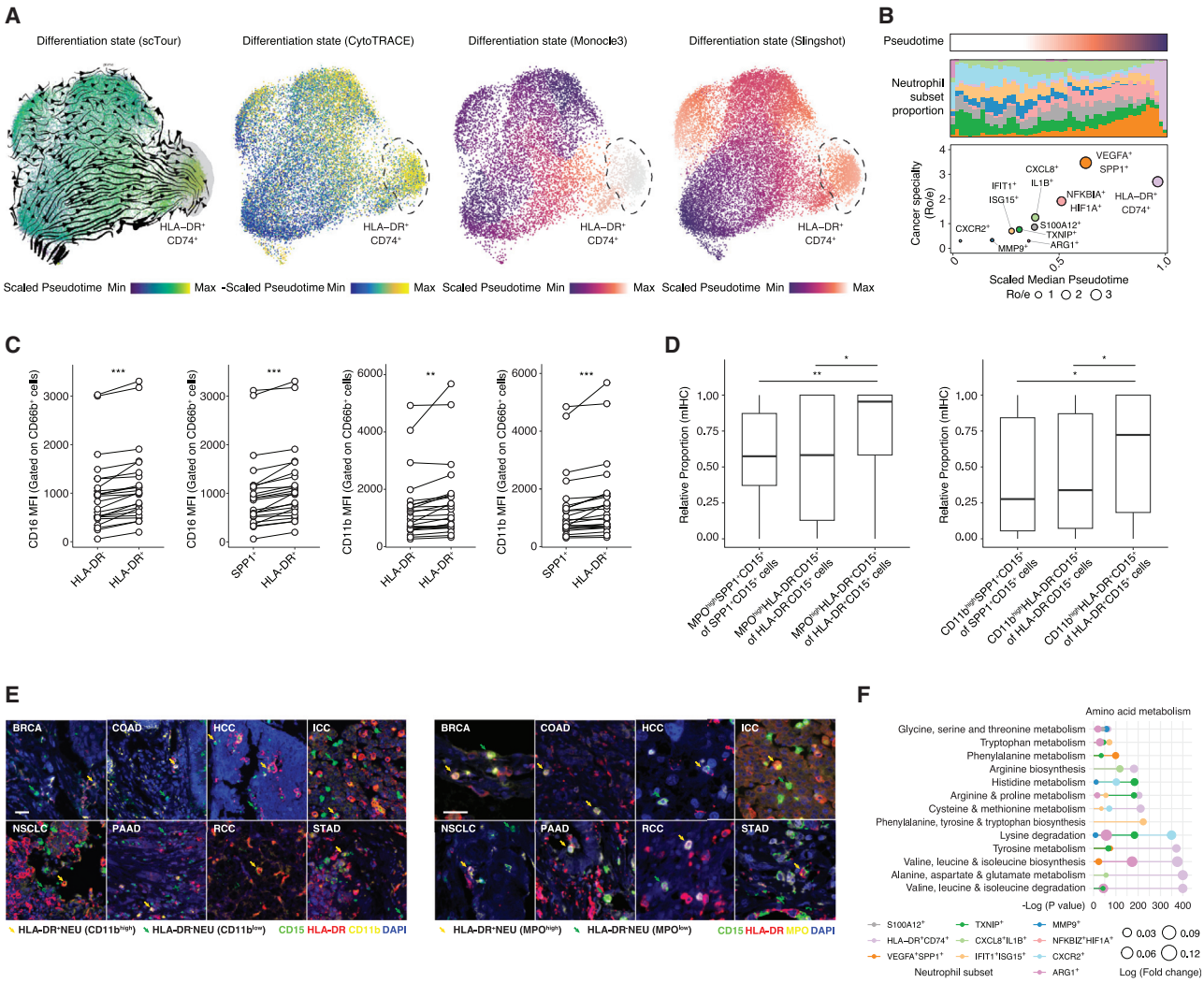

Figure 3. HLA-DR$^+$ neutrophils are terminally differentiated and metabolically reprogrammed

(A) Differentiation state estimated by scTour, CytoTRACE, monocle3, and Slingshot (STAR Methods).

(B) Neutrophil subsets ranked by cancer specialty (Ro/e) and differentiation state (pseudotime by scTour) (upper panel) and correlation between cancer specialty (Ro/e) and pseudotime (lower panel). The dot size represents the Ro/e value of each cell subset.

(C) Flow cytometry of CD11b and CD16 mean fluorescence intensity (MFI) in HLA-DR$^+$ and HLA-DR$^-$ neutrophils isolated from 24 tumor samples from 8 cancer types. **p < 0.01, ***p < 0.001, paired Student's t test. n = 24.

(D) CD11b^{high} and MPO^{high} neutrophil proportion among SPP1$^+$CD15$^+$, HLA-DR$^-$CD15$^+$, and HLA-DR$^+$CD15$^+$ neutrophils using mIHC in the multi-cancer-TMA cohort. *p < 0.05, **p < 0.01, Student's t test. n = 68.

(E) CD11b and MPO intensity in HLA-DR$^+$ and HLA-DR$^-$ neutrophils using mIHC in the multi-cancer-TMA cohort. Scale bars, 30 μm.

(F) Amino acid metabolism pathway activity of neutrophil subsets determined by scMetabolism.[37]

See also Figure S3 and Tables S1 and S3.

(Figure S4E). Among the matched clinical samples, the leucine concentration also showed a strong positive correlation with the HLA-DR$^+$ neutrophil signature (Figure S4F; STAR Methods). Collectively, these data supported the notion that leucine potently primes the neutrophil antigen-presenting program.

To probe how leucine feeds the metabolome and drives the antigen-presenting program, we performed the untargeted metabolomics and observed strong differences in ATP and fatty acid production (Figures 4H, S4G, and S4H; Table S4), partly congruent with the literature.[38] Considering that ATP generation mainly occurs in the mitochondria,[39,40] we hypothesized that leucine may trigger functional or phenotypic remodeling via mitochondria. Indeed, leucine administration caused mitochondria aggregation and altered phenotypes (i.e., mitochondrial quality, Ca^+, and ROS production) (Figures 4I and S4I–S4L). To test the dynamic impact of leucine on mitochondria, we examined the real-time changes in oxygen consumption rate (OCR) and observed that leucine stimulation significantly augmented the mitochondrial OCR (Figure 4J). Transmission electron microscopy (TEM) analysis showed that leucine treatment could

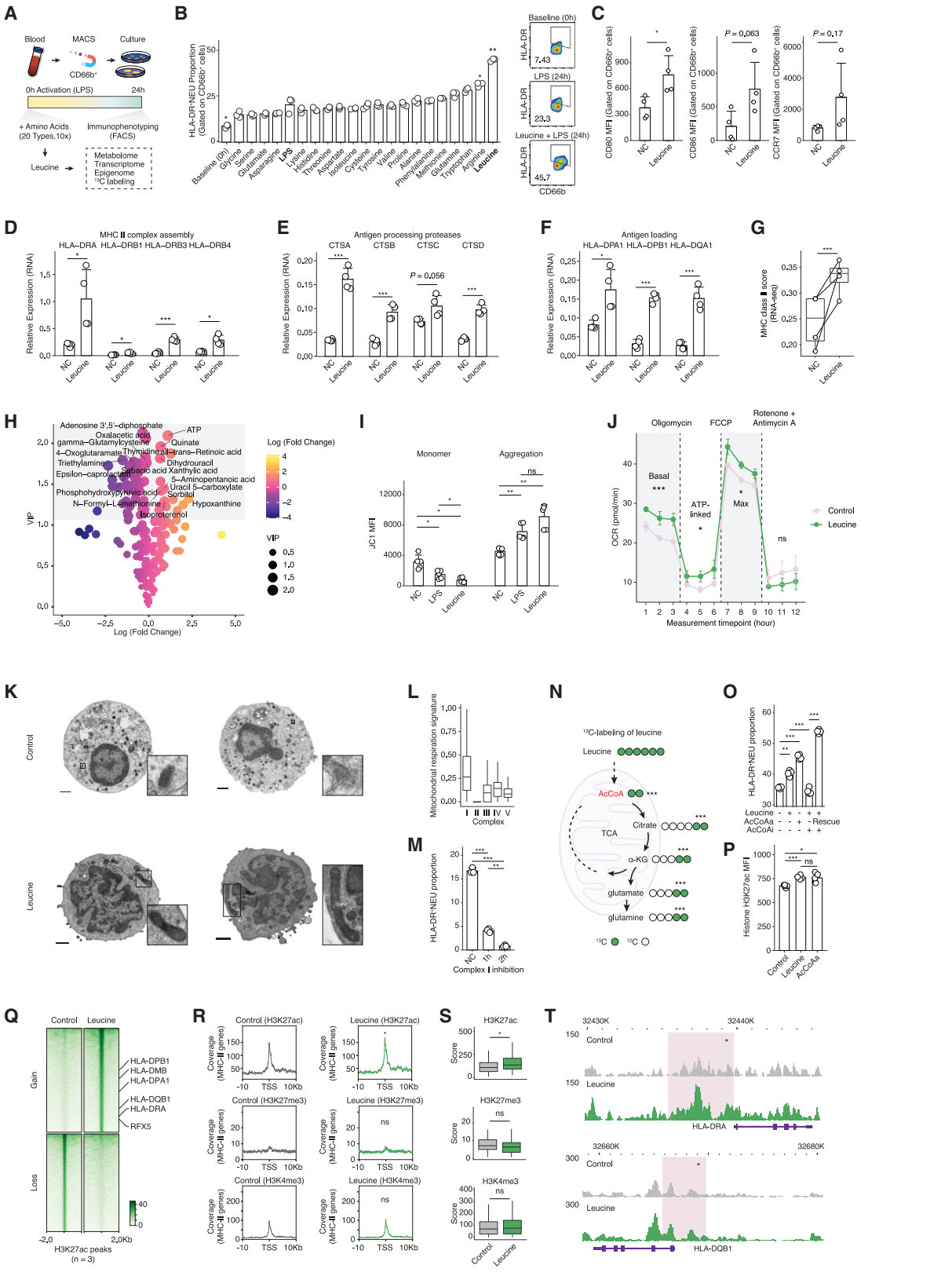

(legend on next page)

induce specific morphological features such as longer mitochondrial length and more pseudopods on the membrane (Figures 4K and S4M), indicating the increased intercellular contact potential.[41] These data were partly in line with the reported role of mitochondrial metabolism in regulating professional antigen-presenting cells.[42]

Given the complexity of the mitochondrial respiration and electron transport chain machinery, we explored the causal effect of leucine on specific mitochondrial subcomponents. By quantifying the mitochondrial respiration signature of single HLA-DR$^+$ neutrophils (Figure 4L), we observed that complex I, which is capable of transferring electrons from reduced nicotinamide adenine dinucleotide (NADH) and producing nicotinamide adenine dinucleotide (NAD),[43] showed higher activity upon leucine administration. However, complex III and IV signature activity was weak or moderate. This observation was supported by the stronger output of NAD by leucine-treated neutrophils (Figure S4N). We therefore inhibited the complex I activity and observed decreased mitochondrial membrane state and HLA-DR$^+$ neutrophil proportion (Figures 4M and S4O). Other mitochondria respiration inhibitors also showed coherent results (Figure S4P). Conversely, NAD supplementation caused higher HLA-DR intensity (Figure S4Q), further confirming the mitochondrial respiration-dependent function of leucine in the HLA-DR program.

We further asked how leucine was catabolized and enhanced HLA-DR expression. We initially fed neutrophils from healthy donor blood with ^{13}C-labeled leucine and found that leucine was catalyzed into acetyl-CoA, entered the tricarboxylic acid (TCA) cycle, and generated an increased amount of glutamate and glutamine (Figure 4N), using the reported catabolism route.[44] Consistently, CoA biosynthesis signature was primed during leucine treatment (Figure S4R), and the acetyl-CoA activator significantly upregulated HLA-DR (Figure 4O). Acetyl-CoA inhibition significantly reduced HLA-DR level while its restoration rescued HLA-DR, indicating the acetyl-CoA-dependent regulation on HLA-DR. Given the known link between acetyl-CoA and histone H3 lysine 27 acetylation (H3K27ac),[45–47] we examined the total H3K27ac level and observed the enhanced H3K27ac upon leucine treatment (Figure 4P), without changes in histones H3 themselves (Figure S4S). Further, CUT&Tag showed significantly upregulated H3K27ac on MHC-II genes (Figure 4Q), but not H3K27me3 and H3K4me3 (Figures 4R and 4S). These data supported the notion that leucine can impact H3K27ac and thereby activate MHC-II genes (i.e., HLA-DRA and HLA-DQB1), its transcription factor, and its regulatory element (i.e., MHC-II super-enhancer[48]) (Figures 4T and S4T). Consistently, the chromatin accessibility of MHC-II genes was also enhanced by leucine treatment (Figure S4U). Overall, our data pointed to the dependency of leucine catabolism for antigen-presenting machinery initiation through mitochondria modeling and metabolism-epigenetic regulation such as the acetyl-CoA/H3K27ac/MHC-II axis.

Antigen-presenting neutrophils spatially link with and fuel T cell responses

Because HLA-DR$^+$ neutrophils favor prognosis, we asked about the mechanisms underlying their potential anti-tumor effects. We first performed bulk RNA-seq of matched tumor samples, deconvoluted[18] the immune cell profile, clustered the immune cell proportions, and observed patterned neutrophil-T cell infiltration profiles (Figures 5A and S5A). In particular, HLA-DR$^+$ neutrophils co-localized with a broad spectrum of anti-tumor T cell subsets (i.e., CD4$^+$ effector memory T cells, CD8$^+$ effector memory T cells, and CD8$^+$ central memory T cells). We fetched 50 spatial transcriptomics datasets covering 1,78,330 spots derived from 9

Figure 4. Leucine primes HLA-DR$^+$ neutrophil generation through metabolic-epigenetic regulation

(A) *In vitro* screening strategy of 20 amino acids to explore their correlation with neutrophil immunophenotypes.

(B) HLA-DR$^+$ neutrophil proportion under the stimulation of each amino acid (control, LPS alone). The right panel shows the HLA-DR level neutrophils under leucine and control conditions. Neutrophils were sorted from healthy donors' blood. n = 3.

(C) Comparison of CD80, CD86, and CCR7 expression on neutrophils between leucine and control groups. n = 4.

(D–F) Relative RNA expression of MHC-II complex assembly genes (D), antigen processing protease genes (E), and MHC-II antigen-loading genes (F) using PCR array. HLA-DRB2, other HLA-DPA family genes, other HLA-DPB family genes, and other HLA-DQA family genes were excluded due to low expression (CT > 35). n = 4.

(G) MHC class II signature of RNA-seq in leucine-treated and control groups. The signature was from Gene Ontology (GO) database. n = 4.

(H) Metabolite comparison between leucine-treated neutrophils and control group. The y axis represents the variable importance in projection (VIP) value. VIP > 1 was regarded as statistical significance (highlighted in gray). The x axis represents the log (fold change) of each metabolite. n = 4.

(I) Mitochondrial aggregation levels using flow cytometry (monomer, fluorescein isothiocyanate (FITC); aggregation, PE) in leucine-treated neutrophils and control group. n = 5.

(J) Real-time oxygen consumption rate (OCR) between leucine-treated neutrophils and control. n = 3.

(K) Mitochondria imaging by transmission electron microscopy of leucine and control groups. Scale bars, 2 μm.

(L) Mitochondrial respiration complex signature based on scRNA-seq data of HLA-DR$^+$ neutrophils. The signature was from the wikipathways database.

(M) Mitochondrial respiration complex I inhibition reduced HLA-DR$^+$ proportion. n = 3.

(N) ^{13}C-labeling of leucine showing its catabolism into acetyl-CoA, TCA cycle, and glutamine. Replicates were merged for analysis. n = 4.

(O) The leucine acetyl-CoA-dependent regulation of HLA-DR$^+$ neutrophils. AcCoAa, AcCoA activator; AcCoAi, AcCoA inhibitor. n = 4.

(P) Histone H3K27ac level between control, leucine-treated, and AcCoAa (AcCoA activator) groups. The MFI was determined by flow cytometry. n = 5.

(Q) Heatmap of H3K27ac peaks of leucine and control groups using CUT&Tag. n = 3. Replicates were merged for visualization.

(R and S) The H3K27ac, H3K27me3, and H3K4me3 coverage (R) and score comparison (S) on MHC-II gene transcription start site (TSS). The MHC-II gene list was from the GO gene set database. Replicates were merged for visualization.

(T) H3K27ac modification on HLA-DRA and HLA-DQB1 locus of leucine and control groups. n = 3.

Data in the bar plots are presented as mean ± standard deviation (B–F, I, M, O, and P) and mean ± standard error (J). ns, not significant, *p < 0.05, **p < 0.01, ***p < 0.001; Student's t test (B–F, I, M, O, and P), paired Student's t test (G), and Wilcox test (R–T).

See also Figure S4 and Table S4.

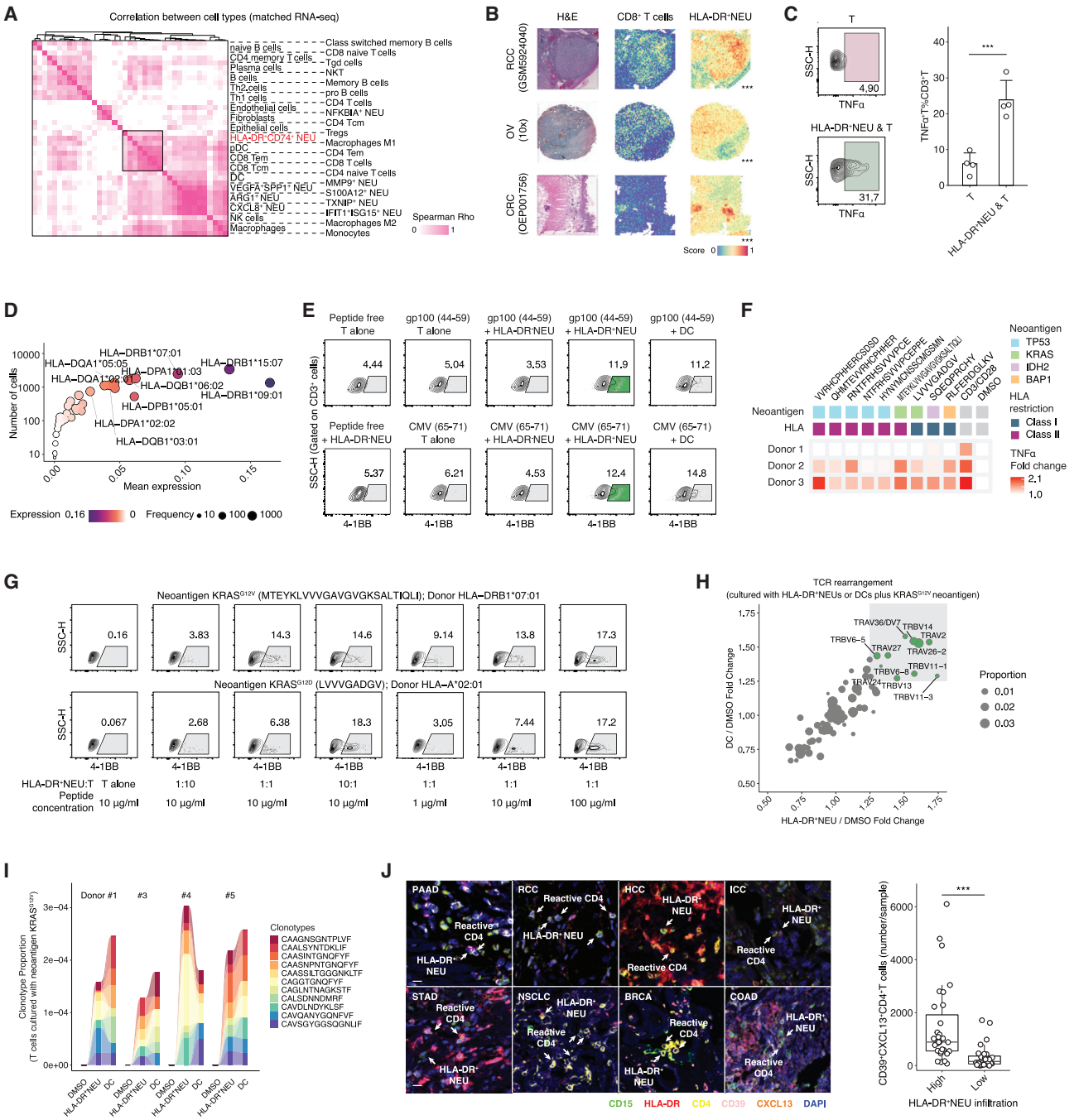

Figure 5. HLA-DR$^+$ neutrophils and related T cell responses

(A) Correlation between immune cell types (estimated from matched RNA-seq) and neutrophil subsets. n = 25.

(B) Spatial co-localization between HLA-DR$^+$ neutrophil signature and CD8$^+$ T cells in RCC, OV, and CRC samples. ***p < 0.001; Spearman-Rho test.

(C) T cell TNFα intensity (gated on CD3$^+$ T cells) coculturing with tumor-infiltrated HLA-DR$^+$ neutrophils or none. The bar plot is mean ± standard deviation. Neutrophils and autologous T cells were sorted from tumors (HCC and COAD) and matched blood samples respectively. n = 4. ns, not significant, ***p < 0.001; Student's t test.

(D) MHC-II allele quantification of tumor-infiltrating neutrophils based on scRNA-seq data.

(E) T cell reactiveness (4-1BB intensity) when coculturing with leucine-treated neutrophils (HLA-DR$^+$ neutrophils), non-treated neutrophils (HLA-DR$^-$ neutrophils), autologous DCs, or negative controls. MHC-II peptides (gp100, 44–59; CMV, 65–71) were added.

(F) T cell cytotoxicity (TNFα intensity) when coculturing with HLA-DR$^+$ neutrophils fed with neoantigens. Autologous leucine-induced HLA-DR$^+$ neutrophils, autologous DCs, and T cells were sorted from healthy donors' blood. n = 3.

(legend continued on next page)

cancer types (BRCA, SKCM, CESC, COAD, OV, PRAD, LGG, HCC, and RCC, Table S5) and computed the correlation between HLA-DR$^+$ neutrophils and major immune lineages (STAR Methods). CD8$^+$ T cells and CD4$^+$ T cells ranked highly among the major lineages (Figure S5B). Of note, in RCC samples (GSM5924040), CD8$^+$ T cells showed strong co-localization with HLA-DR$^+$ neutrophils, with similar results observed in OV (10x) and colorectal cancer (CRC) (OEP001756) samples (Figure 5B). These observations implied that antigen-presenting neutrophils are spatially linked with T cells.

To decode the effect of HLA-DR$^+$ neutrophils on T cells, we co-cultured neutrophil subsets (sorted from the tumor) with autologous CD3$^+$ T cells (sorted from PBMCs) for 3 days, indicating that HLA-DR$^+$ neutrophils can promote T cells to express TNFα (Figure 5C). Given their capacity for antigen presentation, we then quantified the allele-specific HLA gene expression at the single-cell level (Figures 5D and S5C). HLA-DRB1, HLA-DPA1, and HLA-DQB1 showed high frequency, where these loci were reported with T cell epitope restricted reactiveness (HLA-DRB1*09:01)[49] or cytokine production (HLA-DPB1*05:01).[50] We further confirmed the antigen uptake ability of HLA-DR$^+$ neutrophils using OVA fluorescent proteins (Figures S5D and S5E). We hence fed the neutrophils with human MHC-II antigens (gp100, 44–59; CMV, 65–71) and cocultured them with autologous T cells (Figure 5E). Notably, sorted HLA-DR$^+$ neutrophils gave rise to the antigen-specific response of autologous T cells, although more weakly than positive controls (DCs). These data naturally raise the possibility that HLA-DR$^+$ neutrophils are likely to present tumor neoantigens and elicit reactive T cell responses. To test this hypothesis, HLA-DR$^+$ neutrophils were incubated with mutation-derived neoantigens (*TP53*, *KRAS*, *IDH2*, and *BAP1*)[51–53] for 24 h and were further cocultured with autologous CD3$^+$ T cells (Figure 5F). We observed the stimulated T cell responses of most of the neoantigens, although the responses were variable across donors. For example, *KRAS*^{G12V} neoantigen (MTEYKLVVVGAVGVGKSALTIQLI)[53] was associated with strong neutrophil-triggered T cell activation in donors 2 and 3. Our reported *KRAS*^{G12D} neoantigen (LVVVGADGV)[52] also led to reactive T cell responses. Focusing on these two peptides, we performed coculture in which the ratio of neutrophil to T cells and the concentration of peptides were controlled in a donor with HLA−DRB1*07:01 and HLA−A*02:01 types (Figure 5G). When the ratio of HLA-DR$^+$ neutrophils to T cells was 10:1, a potent neoantigen response of T cells was activated with *KRAS*^{G12V} or *KRAS*^{G12D} neoantigens. By sequencing the TCR repertoire of KRAS^{G12V} neoantigen-activated T cells, we observed strong reactive TCR gene rearrangement with HLA-DR$^+$ neutrophil stimulation (negative control, T cell alone; positive control, autologous DCs) (Figures 5H and S5F), which was comparable with DCs (Figure 5I). We finally authenticated the co-localization of reactive T cells (CD39$^+$CXCL13$^+$CD4$^+$ T cells and CD39$^+$CXCL13$^+$CD8$^+$ T cells) and antigen-presenting neutrophils (HLA-DR$^+$CD15$^+$ neutrophils) in the multi-cancer-TMA cohort (Figures 5J and S5G). Together, these data indicated that antigen-presenting neutrophils can effectively generate reactive T cell responses.

We next asked whether neutrophil-elicited T cell activation is dependent on the antigen. By coculturing leucine-stimulated neutrophils with autologous T cells from healthy donors (removing leucine after 24 h of neutrophil stimulation), we observed consistent but slightly weaker T cell activation (Figure S5H) and killing ability for cell lines derived from multiple cancers (Figure S5I), raising the hypothesis that HLA-DR$^+$ neutrophils activate T cells in a nonspecific manner. Subsequently, we tested distinct coculture methods (i.e., in a medium, in a transwell chamber, or directly) and examined the T cell activation levels (Figure S5J). Interestingly, only direct coculture was associated with T cell activation, whereas coculture via medium or transwell system was not. We also neutralized neutrophil-related cytokines but did not observe T cell immunophenotype changes (Figure S5K). These results indicated that HLA-DR$^+$ neutrophils may directly activate T cells mainly via ligand-receptor interactions.

To identify the ligand that drives T cell activation, we ranked the *in silico* results according to interaction frequency and gene expression percentage and focused on the candidate ligands such as ICAM1 and CXCL10 (Figures S5L and S5M). Upon inhibiting the ICAM1 and its interaction with ITGAL, we observed significantly reduced T cell activation (Figure S5N). Meanwhile, ICAM1 and HLA-DR were co-expressed and co-up-regulated by leucine (Figure S5O). In contrast, CXCL10 inhibition showed a negligible effect on T cell activation (Figure S5N). In summary, HLA-DR$^+$ neutrophils are associated with an active TME and can broadly trigger T cell activation, (neo)antigen reactivity, and cytotoxicity, raising the possibility that these cells could be delivered to fuel T cell responses.

Exploring neutrophil-based immunotherapy to fire up TME

Another critical question is whether HLA-DR$^+$ neutrophils have the potential to enhance immunotherapy *in vivo*. To this end, we first evaluated the conservation of neutrophil subsets within mouse TME by collecting mouse scRNA-seq data from 7 murine cancer types (Table S5). We observed similar subsets such as Cd74$^+$, Spp1$^+$Vegfa$^+$, and Isg15$^+$ neutrophils in mice (Figure 6A) as recently reported (Figure S6A).[7,11,14] We further observed

(G) T cell reactiveness (4-1BB intensity) when coculturing with HLA-DR$^+$ neutrophils fed with neoantigens of *KRAS*^{G12V} (MTEYKLVVVGAVGVGKSALTIQLI) or *KRAS*^{G12D} (LVVVGADGV) at different NEU:T ratio and peptide concentration.

(H and I) TCR rearrangement (H) and TCR clonotype proportion (I) of T cells stimulated by HLA-DR$^+$ neutrophils or DCs fed with neoantigens of *KRAS*^{G12V} (MTEYKLVVVGAVGVGKSALTIQLI). CD3/CD28 dynabeads were simultaneously added (4:1 to T cells), and the coculture was performed for 7 days. n = 4. Samples failing quality control were excluded.

(J) Association between HLA-DR$^+$ neutrophils (HLA-DR$^+$CD15$^+$) and reactive CD4 T cells (CXCL13$^+$CD39$^+$CD4$^+$) using mIHC in multi-cancer-TMA cohort covering 8 cancer types. Scale bars, 30 μm. The right panel represents the number of CD39$^+$CXCL13$^+$CD4$^+$T cells among HLA-DR$^+$ neutrophil high/low samples. n = 62 (low-quality images excluded). ***p < 0.001; Student's t test.

See also Figure S5 and Table S5.

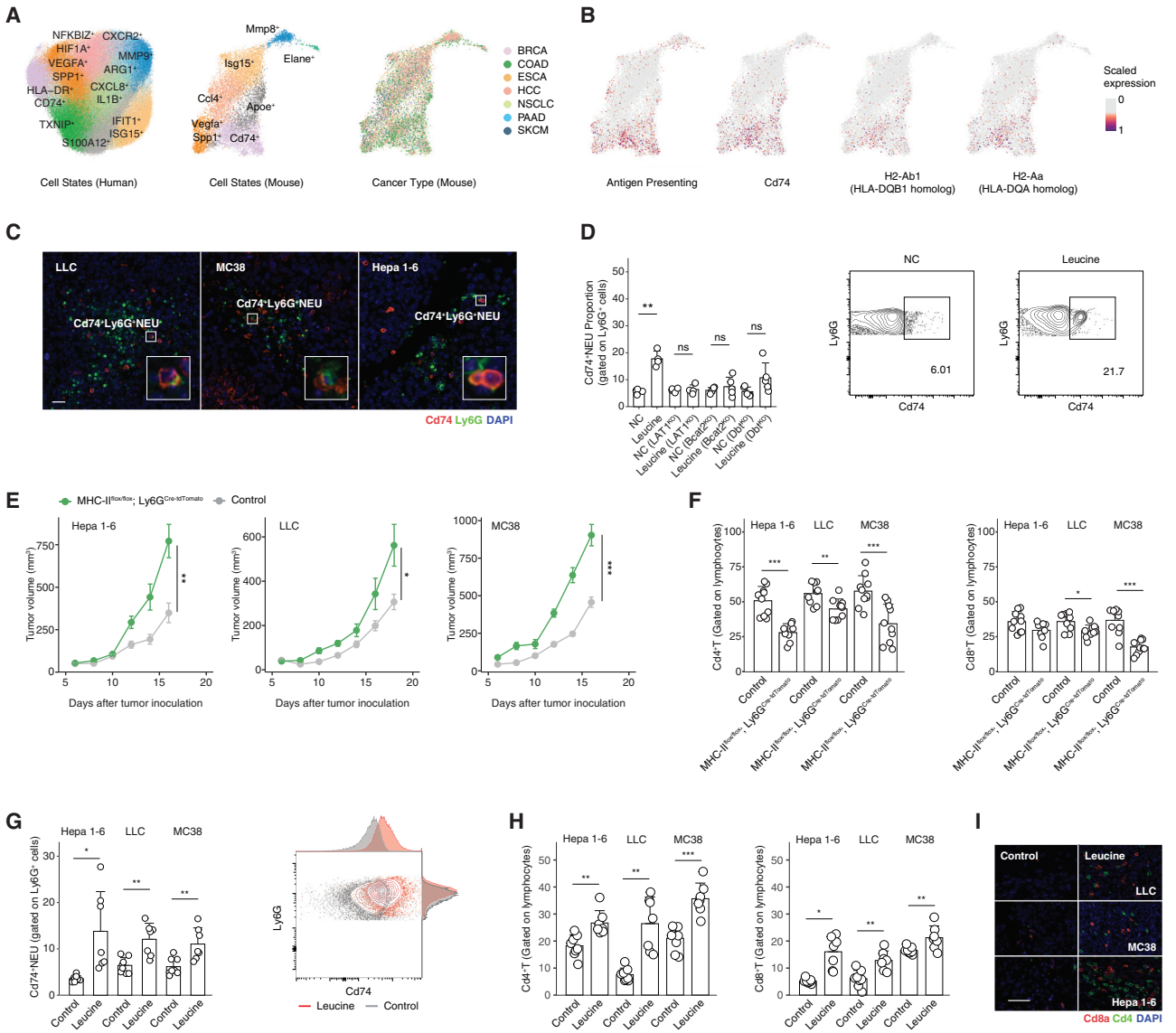

Figure 6. Correlation between antigen-presenting neutrophils and associated *in vivo* immunophenotypes

(A) UMAP of integrated mouse tumor infiltrated neutrophils according to their marker genes and cancer types, in comparison with human neutrophil subsets.

(B) Antigen-presenting gene expression and signature of mouse neutrophils.

(C) Representative mIHC images of Cd74^{+} neutrophils (LLC, MC38, and Hepa 1–6). Scale bars, 50 μm.

(D) Cd74^{+} neutrophil proportion between leucine treated and control neutrophils from the blood of LAT1^{KO}, Bcat2^{KO}, Dbt^{KO}, and wild-type mice. n = 4.

(E) Comparison of tumor volume between MHC-II$^{flox/flox}$; Ly6G$^{Cre\text{-}tdTomato}$ mice and wild-type mice (MHC-II$^{flox/flox}$ Ly6G$^{Cre\text{-}tdTomato}$: LLC, n = 10; Hepa 1–6, n = 8, MC38: n = 10; wild-type: LLC, n = 9; Hepa 1–6, n = 10, MC38: n = 10).

(F) Intratumor Cd8a^{+}T and Cd4^{+}T cell proportion between MHC-II$^{flox/flox}$; Ly6G$^{Cre\text{-}tdTomato}$ mice and wild-type mice in LLC, MC38, and Hepa 1–6 subcutaneous models. Samples were collected on day 16 (MC38 and Hepa 1–6) and day 18 (LLC).

(G) Leucine diet induced higher Cd74^{+} proportion of intratumor neutrophils in LLC, MC38, and Hepa 1–6 subcutaneous models (leucine: LLC, n = 7; Hepa 1–6, n = 7, MC38: n = 7; wild-type: LLC, n = 8; Hepa 1–6, n = 8, MC38: n = 8) by using flow cytometry. Samples were collected on day 12.

(H) Intratumor Cd8a^{+}T and Cd4^{+}T cell proportion between leucine diet and control group in LLC, MC38, and Hepa 1–6 subcutaneous models. Samples were collected on day 12.

(I) Representative mIHC images of Cd4 and Cd8a positive cells between leucine diet and control group in LLC, MC38, and Hepa 1–6 groups. Scale bars, 50 μm. Samples were collected on day 12.

Data are presented as mean ± standard deviation (D–H). ns, not significant, *p < 0.05, **p < 0.01, ***p < 0.001; Student's t test (D–H).

See also Figure S6 and Table S1.

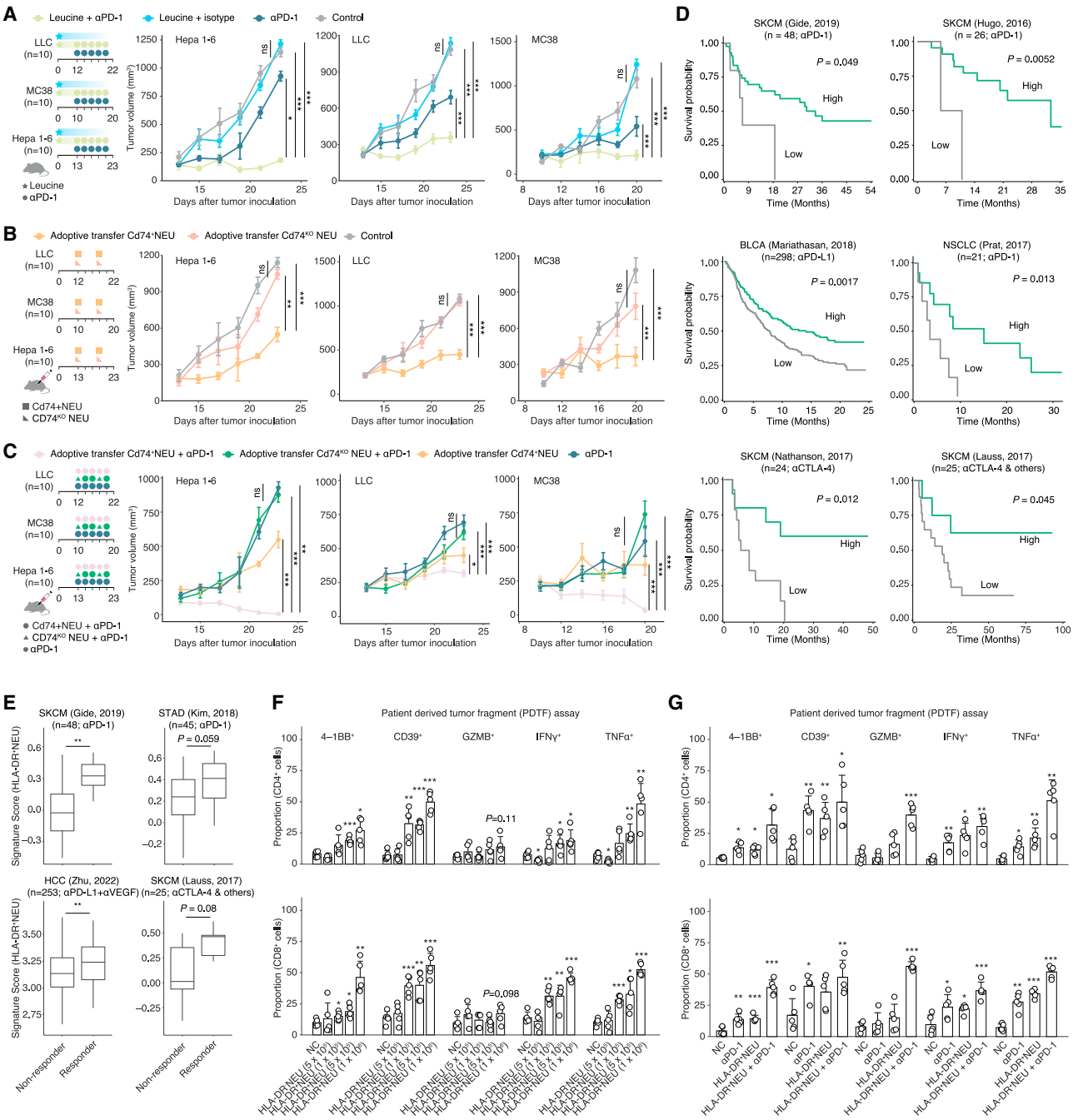

Figure 7. Examination of the therapeutic value of antigen-presenting neutrophils

(A) Tumor volume in leucine diet plus αPD-1 treatment, leucine diet plus isotype treatment, αPD-1 treatment alone, and control groups. n = 10.

(B) Tumor volume in Cd74$^+$ neutrophil adoptive delivering, Cd74-KO neutrophil adoptive delivering, and control groups. The control group is the same as the control group in Figure 7A. n = 10.

(C) Tumor volume in Cd74$^+$ neutrophil adoptive delivering plus αPD-1 treatment, Cd74-KO neutrophil adoptive delivering plus αPD-1 treatment, and αPD-1 treatment alone groups. The αPD-1 alone group is the same as that in Figure 7A. The adoptive transfer Cd74$^+$NEU group is the same as that in Figure 7B. Data in Figures 7A–7C were conducted in the same batch. n = 10.

(D and E) HLA-DR$^+$CD74$^+$ neutrophil signature association with immunotherapy-treated patient survival (D) and responsive pattern (E).[54–61]

(F and G) Proportion of 4-1BB$^+$, CD39$^+$, GZMB$^+$, IFNγ$^+$, and TNFα$^+$ subsets among CD4$^+$ cells (upper panel) and CD8$^+$ cells (lower panel) in PDTF models stimulated by autologous HLA-DR$^+$ neutrophils and HLA-DR$^-$ neutrophils from patient blood at different cell number (F) and HLA-DR$^+$ neutrophils from patient blood, PD-1 antibody, or their combination (G). n = 5.

(legend continued on next page)

H2-Aa (HLA-DQA homolog), H2-Ab1 (HLA-DQB1 homolog), Cd74 (CD74 homolog) expression, and antigen-presenting signature in $Cd74^+$ subsets (Figure 6B) and confirmed this subset using mIHC (Figure 6C). These results not only highlighted the conserved role of antigen-presenting neutrophils but also hinted at the opportunities for investigating these cell subsets *in vivo*.

Given the role of leucine demonstrated above, we stimulated mouse circulating neutrophils with leucine *in vitro* and observed the upregulation of Cd74, Cd80, and Cd86 (Figures 6D and S6B). However, circulating neutrophils from knockout mice lacking the leucine transporter or catabolism enzymes ($Lat1^{KO}$, $Bcat2^{KO}$, and Dbt^{KO}) did not respond to leucine treatment (Figure 6D), again supporting the role of leucine in MHC-II processes.

We subsequently investigated the *in vivo* association between antigen-presenting neutrophils and tumor phenotypes. Initially, we generated the MHC-$II^{flox/flox}$; $Ly6G^{Cre\text{-}tdTomato}$ mice with specific deletion of antigen-presenting neutrophils (Figures 6E and S6C), subcutaneously injecting murine cancer cells (LLC, MC38, and Hepa 1–6), and observed increased tumor growth. Interestingly, intratumor Cd4 and Cd8 T cells both showed significantly decreased infiltration in MHC-$II^{flox/flox}$; $Ly6G^{Cre\text{-}tdTomato}$ group (Figure 6F). We next attempted to increase the antigen-presenting neutrophils *in vivo* by giving mice the leucine-rich diet (1.5% leucine in water) and observed increased $Cd74^+$ neutrophils (Figure 6G), but this short-term diet did not impact cancer volume or body weight (Figures S6D and S6E). We also tested other amino acids (arginine, cysteine, glutamine, and tryptophan) but did not find consistently increased $Cd74^+$ neutrophils (Figure S6F).

We further analyzed the TME profile of the leucine diet using scRNA-seq (Figure S6G), which confirmed the expanded $Cd74^+$ proportion upon leucine treatment (Figure S6H). In addition to antigen-presenting, leucine-stimulated neutrophils also exhibited upregulated chemokines and Toll-like receptor pathways (Figure S6I). Within the cancer cells themselves (Figure S6J), the leucine metabolism signature was also upregulated, along with the robust activity of the epithelial-mesenchymal-transition and TNFα. Given that $CD74^+$ neutrophils can activate T cells, we examined T cell infiltration and observed their increased infiltration (Figures 6H and 6I). Together, these data indicated that a short-term leucine diet was beneficial for anti-TME and induced mild changes in cancer cell phenotypes, raising its potential therapeutic usage.

Then, we explored the therapeutic effect of $Cd74^+$ neutrophils in murine cancers. Notably, leucine diet plus anti-PD-1 therapy significantly reduced tumor volumes and enabled the achievement of stable disease (Figure 7A). Conversely, neutrophil deletion diminished the efficacy of this combination therapy (Figure S7A). We also investigated the delivery of antigen-presenting neutrophils into the TME as another therapeutic option. We isolated mouse circulating neutrophils, stimulated them using leucine, and confirmed their Cd74 upregulation. Delivering those $Cd74^+$ neutrophils into the tumors significantly reduced tumor size but still did not generate stable disease outcomes (Figure 7B), even when the number of neutrophils was increased to 1×10^7 (Figure S7B). When transferring Cd74-deficient neutrophils, we found significantly diminished anti-tumor effects (Figure 7B). We also assessed the lifespan of the antigen-presenting neutrophils upon delivering Cd45.1 neutrophils into Cd45.2 mice and estimated their half-life to be potentially longer (Figure S7C). Upon combining anti-PD-1 antibody and $Cd74^+$ neutrophil delivery (Figure 7C), we observed robust anti-tumor efficacy in all tumor models. Notably, in the MC38 and Hepa 1–6 models, a significant proportion of tumors showed complete responses (MC38, 4 of 10; Hepa 1–6, 6 of 10). In contrast, Cd74-knockout neutrophils showed weak efficacy in combination with anti-PD-1.

We finally examined antigen-presenting neutrophils in clinical immunotherapy data. In 8 cohorts receiving immunotherapy spanning SKCM, STAD, HCC, BLCA, and NSCLC patients,[54–61] we observed significant positive correlations of the HLA-DR^+ neutrophil signature with better survival or responses (Figures 7D and 7E). Next, we tested the adoptive delivery *ex vivo* in anti-PD-1 immunotherapy-resistant HCC samples following the patient-derived tumor fragment (PDTF) strategy.[62] After 3 days of coculture, both CD4 and CD8 T cells displayed upregulation of cytotoxic molecules (IFNγ and TNFα) as well as reactive molecules (4-1BB and CD39) (Figure 7F). Combing antigen-presenting neutrophils and PD-1 antibodies also generated greater T cell reactiveness and cytotoxicity (Figure 7G). Altogether, these *in vivo* and human-sample-derived data highlighted the synergy of antigen-presenting neutrophils in immunotherapy and suggested therapeutic opportunities such as adoptive delivery.

DISCUSSION

High-dimensional single-cell profiling has revolutionized cancer immunology with its scale and ability to decode complex microenvironment[63] and is leading to organ-wide profiling of certain cell types such as T cells or macrophages.[64,65] For neutrophils, the opportunity is now here to orchestrate a unified data-driven framework for defining neutrophil ontology. Here, we integrated the neutrophil transcriptomes of 225 samples from 143 patients across 17 cancer types and observed high transcriptional heterogeneity composed of 10 cell states. Notably, the HLA-DR program could be stimulated by leucine treatment, which induced higher mitochondrial respiration, acetyl-coenzyme A output, and epigenetic activation of antigen-presenting genes. As such, a leucine diet or adoptive delivery strategy could boost cancer immunotherapeutic efficacy and may serve as a potential neutrophil-based therapeutic strategy.

Profiling single human neutrophils in an unbiased manner remains a major challenge. Both mouse and human neutrophils are short-lived[3,66] and hence have been largely neglected in previous cancer single-cell profiling studies. Our strategy of neutrophil sorting plus single-cell sequencing has made it possible to explore the spectra of neutrophil states, the heterogeneity of cell subsets, and their temporal changes throughout cancer

Data are presented as mean ± standard error (A–C) and mean ± standard deviation (F and G). ns, not significant, *$p < 0.05$, **$p < 0.01$, ***$p < 0.001$; Wilcox test (E), Student's t test (A, B, C, F, and G), and log-rank test (D).
See also Figure S7.

stages. Our cross-species integration of neutrophil data could help establish a hierarchy of neutrophils that is conserved in humans and mice, providing a potential foundation for the application of murine models in exploring neutrophil-based therapies.

The cancer-immune cycle is initiated by antigen presentation processes[67]; however, impaired antigen-presenting machineries within the TME, such as DC dysfunction and HLA downregulation, can drive immune evasion.[68] Our high-resolution mapping approach identified HLA-DR$^+$CD74$^+$ neutrophils as alternative antigen-presenting cells across various cancer types. A similar subset of neutrophils was discovered in early-stage lung cancer in 2016,[69] and an independent group recently reported that an anti-FcγRIIIB-antigen conjugate may convert neutrophils into antigen-presenting cells.[70] In line with this functional plasticity, our work provides further evidence of metabolic regulation of antigen presentation, demonstrating the role of amino acids in promoting neutrophil antigen presentation, whereas fatty acid or glucose nutrient stress was essential in regulating macrophage antigen-presenting function.[71,72] Compared with other professional antigen-presenting cells like dendritic cells, B cells, and certain macrophage subsets, neutrophils expressing HLA-DR may have some advantages in certain contexts. For example, neutrophils are often one of the first responders to sites of inflammation.[1] Uniquely, neutrophils possess active phagocytic capabilities and chemotaxis features.[1] This attribute potentially empowers them to efficiently migrate and degrade antigens, thus bolstering their role as antigen-presenting cells. Another crucial feature of neutrophils is their short half-life, which potentially minimizes the chance of their being reprogrammed into immunosuppressive cells by the TME. This is a risk that other longer-lived immune cells might face. These distinctive characteristics underscore the potential value of neutrophils in anti-tumor immune response. Further studies may explore direct comparisons of antigen presentation capabilities between HLA-DR$^+$ neutrophils and other professional APCs.

Importantly, our results may offer opportunities for superior immunotherapy. First, different from neutrophil depletion therapies, our neutrophil delivery strategy requires only the sorting of autologous circulating neutrophils and short-term *ex vivo* stimulation, making it a safer alternative that does not leave patients susceptible to infection. Second, HLA-DR$^+$ neutrophils can be loaded with a broad spectrum of (neo)antigens without the need for complex genetic engineering, which is a potential advantage over CAR-T cells with limited target antigens, complicated purification processes, and costly T cell engineering. However, the adverse events of such therapy are still worth studying. Third, given the short half-life of neutrophils, the side effects of this therapy might be transient and manageable. This characteristic might minimize the duration of any potential side effects, allowing for timely intervention and treatment alteration. Comprehensive preclinical and clinical studies will be needed to fully understand the safety profile of this promising therapy.

In summary, our dataset adds to the growing evidence that the cellular neighborhood within tumors is critical for shaping immune responses. Neutrophil transcriptome profiling allows for simultaneously looking at what cell states are, via the gene program they express, and how they reside across diverse cancer types. Our data will help unravel the cellular circuit of neutrophil subsets as well as potentially bridge the gap separating metabolism, epigenetic modification, and innate immune cell phenotypes. Our study may provide opportunities for modulating (neo)antigen-specific immune responses by developing neutrophil therapy that could potentially complement existing cancer immunotherapies.

Limitations of the study

The exploration of state-switching in tumor-associated neutrophils (e.g., generation of HLA-DR$^+$ neutrophils) continues to be valuable in a variety of contexts, including tumors with diverse genetic backgrounds, immunotherapy-treatment refractory tumors, and metastatic tumors. Our studies covered a relatively limited sample size (i.e., multi-cancer TMA cohort containing 8 cancer types), and further validation of neutrophil states across larger cohorts is needed to support the generalizability of these findings. Although our study demonstrated that leucine can enhance neutrophil-dependent antigen presentation and anti-tumor immunity, the potential adverse effects of a leucine-rich diet remain poorly defined. It also remains elusive why leucine intensity varies among different tumors and whether the antigen-presenting function of neutrophils can be lost in leucine-poor tumors. In addition, the potential metabolic variation among neutrophil subsets remains unclear. For example, although HLA-DR$^+$ neutrophils showed increases in leucine metabolism, the TXNIP$^+$ subset displayed unique enrichment in histidine, arginine, and proline metabolism. Testing whether neutrophils can preferentially take up or utilize these amino acids could provide insights into their functional differences.

We observed increased T cell proliferation with HLA-DR$^+$ neutrophils; further work is needed to detail how they directly activate T cells. Testing antigen presentation to T cells *in vitro* and analyzing CD4$^+$/CD8$^+$ T cell responses *in vivo* could elucidate this. Tracking adoptively transferred HLA-DR$^+$ neutrophils would also shed light on their migration patterns and ability to reach draining lymph nodes. Although our data demonstrate HLA-DR+ neutrophils can activate T cells and express high CCL5, which can recruit T cells, the relationship between localized neutrophil-T cell interactions versus broader effects on T cell infiltration warrants further exploration. It is also interesting to explore the junctions and synapses between T cells and antigen-presenting neutrophils to provide further insight into their intercellular communication beyond static snapshot analyses. Tracing the half-life of neutrophils (in the tumor, blood, and lymph nodes) will be informative for their clinical applicability. Future research should focus on developing more effective strategies for reprogramming neutrophils into anti-tumor states such as antigen-presenting states.

STAR★METHODS

Detailed methods are provided in the online version of this paper and include the following:

- KEY RESOURCES TABLE
- RESOURCE AVAILABILITY
  - Lead contact
  - Materials availability
  - Data and code availability

- EXPERIMENTAL MODEL AND STUDY PARTICIPANT DETAILS
  - Patient inclusion and sample collection
  - Mouse models
- METHOD DETAILS
  - Standardized cell sorting protocol
  - Single-cell sequencing
  - ScRNA-seq data quality control, processing, annotation, and visualization
  - Single-cell transcriptional program feature gene analysis and signature quantification
  - Single-cell HLA-type quantification
  - Single-cell metabolism quantification
  - Cell-cell communication, cell trajectory, and cell clade analysis
  - Generating the pan-cancer neutrophil infiltration consensus
  - Transcription factor activity analysis
  - Multiplex immunohistochemistry analysis
  - Cell culture
  - Flow cytometry
  - PCR array analysis of MHC class I and II antigen presentation genes
  - Metabolomics LC-MS analysis and leucine tracing
  - Mitochondrial functional and phenotypic characterization
  - Seahorse assays
  - Transmission electron microscopy (TEM)
  - Confocal imaging
  - Bulk RNA-seq
  - H3K27ac, H3K27me3, and H3K4me3 CUT&Tag
  - ATAC-seq
  - Spatial transcriptomics
  - Neoantigen, T cell, and neutrophil coculture system
  - Reactive T cell response evaluated by TCR-seq
  - Cancer cell, T cell, and neutrophil coculture system
  - Mouse model
  - Patient-derived tumor fragment
  - Web server
  - Data visualization
- QUANTIFICATION AND STATISTICAL ANALYSIS

SUPPLEMENTAL INFORMATION

Supplemental information can be found online at https://doi.org/10.1016/j.cell.2024.02.005.

ACKNOWLEDGMENTS

This study was supported by the National Natural Science Foundation of China (nos. 82130077, 81961128025, 82121002, and 82341008) to Q.G.; the National Natural Science Foundation of China (nos. 82394450, U23A6010) to J.F.; the National Natural Science Foundation of China (31925011) to L.Y.; The Research Projects from the Science and Technology Commission of Shanghai Municipality (nos. 21JC1410100, 21JC1401200, 20JC1418900, and 20YF1407400) to J.F., Q.G., and S.Z.; the Shanghai Municipal Science and Technology Major Project to Q.G.; the Strategic Priority Research Program (XDPB0303) of the Chinese Academy of Sciences, Program of Shanghai Academic Research Leader (23XD1404300), and the Shanghai Municipal Science and Technology Major Project (no. 2019SHZDZX02) to X.Z.; and the Science and Technology Commission of Shanghai Municipality (22ZR1479100) to S.J. We thank Claude Leclerc (Pasteur Institute), Andrew Zhu (Massachusetts General Hospital), Feng Wang, Jing Wang (Shanghai Institute of Immunology), Qunying Lei, Di Zhu, Liangqing Dong, Youpei Lin, Haichao Zhao, Xia Shen, Fanfan Fan, Shuaixi Yang, and Zijian Yang (Fudan University) for their support. We thank Shanghai Biochip Co., Ltd. for technical assistance. We thank the computing platform of the Medical Research Data Center of Shanghai Medical College Fudan University.

AUTHOR CONTRIBUTIONS

Conceptualization, J.F., X.Z., and Q.G.; methodology, Y.W., J.M., X.Y., F.N., T.Z., and S.J.; software, Y.W., J.M., X.Y., F.N., T.Z., and S.J.; validation, Y.W., J.M., X.Y., F.N., T.Z., and S.J.; investigation, Y.W., J.M., X.Y., F.N., T.Z., and S.J.; formal analysis, Y.W., J.M., X.Y., and F.N.; writing – original draft, Y.W., F.N., J.M., L.Y., X.Z., and Q.G.; writing – review & editing, Y.W., J.M., X.Y., F.N., T.Z., S.J., D.R., H.F., K.G., X.G., S.J., G.S., J.P., M.Z., Y.X., S.Z., Y.F., X.W., J.Z., L.Y., J.F., X.Z., and Q.G.; visualization, Y.W., J.M., X.Y., F.N., T.Z., and S.J.; funding acquisition, Y.W., F.N., S.J., S.Z., L.Y., J.F., X. Z., and Q.G.; resources, X.W., J.Z., L.Y., J.F., X.Z., and Q.G.; and supervision, L.Y., J.F., X.Z., and Q.G.

DECLARATION OF INTERESTS

The authors declare no potential conflicts of interest.

Received: April 11, 2023
Revised: September 20, 2023
Accepted: February 5, 2024
Published: March 5, 2024

REFERENCES

1. Burn, G.L., Foti, A., Marsman, G., Patel, D.F., and Zychlinsky, A. (2021). The Neutrophil. Immunity *54*, 1377–1391.
2. Hedrick, C.C., and Malanchi, I. (2022). Neutrophils in cancer: heterogeneous and multifaceted. Nat. Rev. Immunol. *22*, 173–187.
3. Summers, C., Rankin, S.M., Condliffe, A.M., Singh, N., Peters, A.M., and Chilvers, E.R. (2010). Neutrophil kinetics in health and disease. Trends Immunol. *31*, 318–324.
4. Wigerblad, G., Cao, Q., Brooks, S., Naz, F., Gadkari, M., Jiang, K., Gupta, S., O'Neil, L., Dell'orso, S., Kaplan, M.J., et al. (2022). Single-Cell Analysis Reveals the Range of Transcriptional States of Circulating Human Neutrophils. J. Immunol. *209*, 772–782.
5. Grover, A., Sanseviero, E., Timosenko, E., and Gabrilovich, D.I. (2021). Myeloid-Derived Suppressor Cells: A Propitious Road to Clinic. Cancer Discov. *11*, 2693–2706.
6. Ng, M.S.F., Kwok, I., Tan, L., Shi, C., Cerezo-Wallis, D., Tan, Y., Leong, K., Calvo, G.F., Yang, K., Zhang, Y., et al. (2024). Deterministic reprogramming of neutrophils within tumors. Science *383*, eadf6493.
7. Xue, R., Zhang, Q., Cao, Q., Kong, R., Xiang, X., Liu, H., Feng, M., Wang, F., Cheng, J., Li, Z., et al. (2022). Liver tumour immune microenvironment subtypes and neutrophil heterogeneity. Nature *612*, 141–147.
8. Jia, K., Chen, Y., Xie, Y., Chong, X., Li, Y., Wu, Y., Yuan, J., Li, Y., Feng, X., Hu, Y., et al. (2023). Multidimensional immune profiling in Gastric Cancer Multiplex Immunohistochemistry Atlas from Peking University Cancer Hospital project informs PD-1/PD-L1 blockade efficacy. Eur. J. Cancer *189*, 112931.
9. Chen, Y., Jia, K., Sun, Y., Zhang, C., Li, Y., Zhang, L., Chen, Z., Zhang, J., Hu, Y., Yuan, J., et al. (2022). Predicting response to immunotherapy in gastric cancer via multi-dimensional analyses of the tumour immune microenvironment. Nat. Commun. *13*, 4851.
10. Cui, C., Chakraborty, K., Tang, X.A., Zhou, G., Schoenfelt, K.Q., Becker, K.M., Hoffman, A., Chang, Y.F., Blank, A., Reardon, C.A., et al. (2021).

Neutrophil elastase selectively kills cancer cells and attenuates tumorigenesis. Cell *184*, 3163–3177.e21.

11. Hirschhorn, D., Budhu, S., Kraehenbuehl, L., Gigoux, M., Schröder, D., Chow, A., Ricca, J.M., Gasmi, B., De Henau, O., Mangarin, L.M.B., et al. (2023). T cell immunotherapies engage neutrophils to eliminate tumor antigen escape variants. Cell *186*, 1432–1447.e17.
12. Kalafati, L., Kourtzelis, I., Schulte-Schrepping, J., Li, X., Hatzioannou, A., Grinenko, T., Hagag, E., Sinha, A., Has, C., Dietz, S., et al. (2020). Innate Immune Training of Granulopoiesis Promotes Anti-tumor Activity. Cell *183*, 771–785.e12.
13. Singhal, S., Bhojnagarwala, P.S., O'Brien, S., Moon, E.K., Garfall, A.L., Rao, A.S., Quatromoni, J.G., Stephen, T.L., Litzky, L., Deshpande, C., et al. (2016). Origin and Role of a Subset of Tumor-Associated Neutrophils with Antigen-Presenting Cell Features in Early-Stage Human Lung Cancer. Cancer Cell *30*, 120–135.
14. Gungabeesoon, J., Gort-Freitas, N.A., Kiss, M., Bolli, E., Messemaker, M., Siwicki, M., Hicham, M., Bill, R., Koch, P., Cianciaruso, C., et al. (2023). A neutrophil response linked to tumor control in immunotherapy. Cell *186*, 1448–1464.e20.
15. Jaillon, S., Ponzetta, A., Di Mitri, D., Santoni, A., Bonecchi, R., and Mantovani, A. (2020). Neutrophil diversity and plasticity in tumour progression and therapy. Nat. Rev. Cancer *20*, 485–503.
16. Becht, E., Giraldo, N.A., Lacroix, L., Buttard, B., Elarouci, N., Petitprez, F., Selves, J., Laurent-Puig, P., Sautès-Fridman, C., Fridman, W.H., et al. (2016). Estimating the population abundance of tissue-infiltrating immune and stromal cell populations using gene expression. Genome Biol. *17*, 218.
17. Finotello, F., Mayer, C., Plattner, C., Laschober, G., Rieder, D., Hackl, H., Krogsdam, A., Loncova, Z., Posch, W., Wilflingseder, D., et al. (2019). Molecular and pharmacological modulators of the tumor immune contexture revealed by deconvolution of RNA-seq data. Genome Med. *11*, 34.
18. Aran, D., Hu, Z., and Butte, A.J. (2017). xCell: digitally portraying the tissue cellular heterogeneity landscape. Genome Biol. *18*, 220.
19. Li, Y., Porta-Pardo, E., Tokheim, C., Bailey, M.H., Yaron, T.M., Stathias, V., Geffen, Y., Imbach, K.J., Cao, S., Anand, S., et al. (2023). Pan-cancer proteogenomics connects oncogenic drivers to functional states. Cell *186*, 3921–3944.e25.
20. Thorsson, V., Gibbs, D.L., Brown, S.D., Wolf, D., Bortone, D.S., Ou Yang, T.H., Porta-Pardo, E., Gao, G.F., Plaisier, C.L., Eddy, J.A., et al. (2018). The Immune Landscape of Cancer. Immunity *48*, 812–830.e14.
21. Bagaev, A., Kotlov, N., Nomie, K., Svekolkin, V., Gafurov, A., Isaeva, O., Osokin, N., Kozlov, I., Frenkel, F., Gancharova, O., et al. (2021). Conserved pan-cancer microenvironment subtypes predict response to immunotherapy. Cancer Cell *39*, 845–865.e7.
22. Salcher, S., Sturm, G., Horvath, L., Untergasser, G., Kuempers, C., Fotakis, G., Panizzolo, E., Martowicz, A., Trebo, M., Pall, G., et al. (2022). High-resolution single-cell atlas reveals diversity and plasticity of tissue-resident neutrophils in non-small cell lung cancer. Cancer Cell *40*, 1503–1520.e8.
23. Zilionis, R., Engblom, C., Pfirschke, C., Savova, V., Zemmour, D., Saatcioglu, H.D., Krishnan, I., Maroni, G., Meyerovitz, C.V., Kerwin, C.M., et al. (2019). Single-Cell Transcriptomics of Human and Mouse Lung Cancers Reveals Conserved Myeloid Populations across Individuals and Species. Immunity *50*, 1317–1334.e10.
24. Luca, B.A., Steen, C.B., Matusiak, M., Azizi, A., Varma, S., Zhu, C., Przybyl, J., Espín-Pérez, A., Diehn, M., Alizadeh, A.A., et al. (2021). Atlas of clinically distinct cell states and ecosystems across human solid tumors. Cell *184*, 5482–5496.e28.
25. Wang, L., Liu, Y., Dai, Y., Tang, X., Yin, T., Wang, C., Wang, T., Dong, L., Shi, M., Qin, J., et al. (2023). Single-cell RNA-seq analysis reveals BHLHE40-driven pro-tumour neutrophils with hyperactivated glycolysis in pancreatic tumour microenvironment. Gut *72*, 958–971.
26. Schwartz, G.W., Zhou, Y., Petrovic, J., Fasolino, M., Xu, L., Shaffer, S.M., Pear, W.S., Vahedi, G., and Faryabi, R.B. (2020). TooManyCells identifies and visualizes relationships of single-cell clades. Nat. Methods *17*, 405–413.
27. Huffman, A.P., Lin, J.H., Kim, S.I., Byrne, K.T., and Vonderheide, R.H. (2020). CCL5 mediates CD40-driven CD4+ T cell tumor infiltration and immunity. JCI Insight *5*, e137263.
28. Hewitt, E.W. (2003). The MHC class I antigen presentation pathway: strategies for viral immune evasion. Immunology *110*, 163–169.
29. Xie, X., Shi, Q., Wu, P., Zhang, X., Kambara, H., Su, J., Yu, H., Park, S.Y., Guo, R., Ren, Q., et al. (2020). Single-cell transcriptome profiling reveals neutrophil heterogeneity in homeostasis and infection. Nat. Immunol. *21*, 1119–1133.
30. Adrover, J.M., Aroca-Crevillén, A., Crainiciuc, G., Ostos, F., Rojas-Vega, Y., Rubio-Ponce, A., Cilloniz, C., Bonzón-Kulichenko, E., Calvo, E., Rico, D., et al. (2020). Programmed 'disarming' of the neutrophil proteome reduces the magnitude of inflammation. Nat. Immunol. *21*, 135–144.
31. Adrover, J.M., Del Fresno, C., Crainiciuc, G., Cuartero, M.I., Casanova-Acebes, M., Weiss, L.A., Huerga-Encabo, H., Silvestre-Roig, C., Rossaint, J., Cossío, I., et al. (2019). A Neutrophil Timer Coordinates Immune Defense and Vascular Protection. Immunity *50*, 390–402.e10.
32. Li, Q. (2022). scTour: a deep learning architecture for robust inference and accurate prediction of cellular dynamics. Preprint at bioRxiv. https://www.biorxiv.org/content/10.1101/2022.04.17.488600v1.
33. Qiu, X., Mao, Q., Tang, Y., Wang, L., Chawla, R., Pliner, H.A., and Trapnell, C. (2017). Reversed graph embedding resolves complex single-cell trajectories. Nat. Methods *14*, 979–982.
34. Gulati, G.S., Sikandar, S.S., Wesche, D.J., Manjunath, A., Bharadwaj, A., Berger, M.J., Ilagan, F., Kuo, A.H., Hsieh, R.W., Cai, S., et al. (2020). Single-cell transcriptional diversity is a hallmark of developmental potential. Science *367*, 405–411.
35. Street, K., Risso, D., Fletcher, R.B., Das, D., Ngai, J., Yosef, N., Purdom, E., and Dudoit, S. (2018). Slingshot: cell lineage and pseudotime inference for single-cell transcriptomics. BMC Genomics *19*, 477.
36. Scapini, P., Marini, O., Tecchio, C., and Cassatella, M.A. (2016). Human neutrophils in the saga of cellular heterogeneity: insights and open questions. Immunol. Rev. *273*, 48–60.
37. Wu, Y., Yang, S., Ma, J., Chen, Z., Song, G., Rao, D., Cheng, Y., Huang, S., Liu, Y., Jiang, S., et al. (2022). Spatiotemporal Immune Landscape of Colorectal Cancer Liver Metastasis at Single-Cell Level. Cancer Discov. *12*, 134–153.
38. Newgard, C.B. (2012). Interplay between lipids and branched-chain amino acids in development of insulin resistance. Cell Metab. *15*, 606–614.
39. Rath, E., Moschetta, A., and Haller, D. (2018). Mitochondrial function - gatekeeper of intestinal epithelial cell homeostasis. Nat. Rev. Gastroenterol. Hepatol. *15*, 497–516.
40. Martínez-Reyes, I., and Chandel, N.S. (2020). Mitochondrial TCA cycle metabolites control physiology and disease. Nat. Commun. *11*, 102.
41. Francis, E.A., and Heinrich, V. (2018). Extension of chemotactic pseudopods by nonadherent human neutrophils does not require or cause calcium bursts. Sci. Signal. *11*, eaal4289.
42. Cervantes-Silva, M.P., Carroll, R.G., Wilk, M.M., Moreira, D., Payet, C.A., O'Siorain, J.R., Cox, S.L., Fagan, L.E., Klavina, P.A., He, Y., et al. (2022). The circadian clock influences T cell responses to vaccination by regulating dendritic cell antigen processing. Nat. Commun. *13*, 7217.
43. Fiedorczuk, K., and Sazanov, L.A. (2018). Mammalian Mitochondrial Complex I Structure and Disease-Causing Mutations. Trends Cell Biol. *28*, 835–867.
44. Zaganjor, E., Yoon, H., Spinelli, J.B., Nunn, E.R., Laurent, G., Keskinidis, P., Sivaloganathan, S., Joshi, S., Notarangelo, G., Mulei, S., et al. (2021). SIRT4 is an early regulator of branched-chain amino acid catabolism that promotes adipogenesis. Cell Rep. *36*, 109345.

45. Lauterbach, M.A., Hanke, J.E., Serefidou, M., Mangan, M.S.J., Kolbe, C.C., Hess, T., Rothe, M., Kaiser, R., Hoss, F., Gehlen, J., et al. (2019). Toll-like Receptor Signaling Rewires Macrophage Metabolism and Promotes Histone Acetylation via ATP-Citrate Lyase. Immunity *51*, 997–1011.e7.

46. Li, L., Chen, K., Wang, T., Wu, Y., Xing, G., Chen, M., Hao, Z., Zhang, C., Zhang, J., Ma, B., et al. (2020). Glis1 facilitates induction of pluripotency via an epigenome-metabolome-epigenome signalling cascade. Nat. Metab. *2*, 882–892.

47. Wu, Y., Liu, Y., Hao, Z., and Liu, X. (2022). NAD^+ is critical for maintaining acetyl-CoA and H3K27ac in embryonic stem cells by Sirt1-dependent deacetylation of AceCS1. Life Med. *1*, 401–405.

48. Cavalli, G., Hayashi, M., Jin, Y., Yorgov, D., Santorico, S.A., Holcomb, C., Rastrou, M., Erlich, H., Tengesdal, I.W., Dagna, L., et al. (2016). MHC class II super-enhancer increases surface expression of HLA-DR and HLA-DQ and affects cytokine production in autoimmune vitiligo. Proc. Natl. Acad. Sci. USA *113*, 1363–1368.

49. Liu, S.D., Zhang, S.M., Wang, H., He, J.C., Yang, X.F., Du, X.L., and Ma, L. (2016). Identification of HLA-DRB1*09:01-restricted Mycobacterium tuberculosis $CD4^+$ T-cell epitopes. FEBS Lett. *590*, 4541–4549.

50. Lin, Y., Fujiki, F., Katsuhara, A., Oka, Y., Tsuboi, A., Aoyama, N., Tanii, S., Nakajima, H., Tatsumi, N., Morimoto, S., et al. (2013). HLA-DPB1*05:01-restricted WT1332-specific TCR-transduced $CD4^+$ T lymphocytes display a helper activity for WT1-specific CTL induction and a cytotoxicity against leukemia cells. J. Immunother. *36*, 159–170.

51. Malekzadeh, P., Pasetto, A., Robbins, P.F., Parkhurst, M.R., Paria, B.C., Jia, L., Gartner, J.J., Hill, V., Yu, Z., Restifo, N.P., et al. (2019). Neoantigen screening identifies broad TP53 mutant immunogenicity in patients with epithelial cancers. J. Clin. Invest. *129*, 1109–1114.

52. Lin, Y., Peng, L., Dong, L., Liu, D., Ma, J., Lin, J., Chen, X., Lin, P., Song, G., Zhang, M., et al. (2022). Geospatial Immune Heterogeneity Reflects the Diverse Tumor-Immune Interactions in Intrahepatic Cholangiocarcinoma. Cancer Discov. *12*, 2350–2371.

53. Yossef, R., Tran, E., Deniger, D.C., Gros, A., Pasetto, A., Parkhurst, M.R., Gartner, J.J., Prickett, T.D., Cafri, G., Robbins, P.F., et al. (2018). Enhanced detection of neoantigen-reactive T cells targeting unique and shared oncogenes for personalized cancer immunotherapy. JCI Insight *3*, e122467.

54. Gide, T.N., Quek, C., Menzies, A.M., Tasker, A.T., Shang, P., Holst, J., Madore, J., Lim, S.Y., Velickovic, R., Wongchenko, M., et al. (2019). Distinct Immune Cell Populations Define Response to Anti-PD-1 Monotherapy and Anti-PD-1/Anti-CTLA-4 Combined Therapy. Cancer Cell *35*, 238–255.e6.

55. Hugo, W., Zaretsky, J.M., Sun, L., Song, C., Moreno, B.H., Hu-Lieskovan, S., Berent-Maoz, B., Pang, J., Chmielowski, B., Cherry, G., et al. (2016). Genomic and Transcriptomic Features of Response to Anti-PD-1 Therapy in Metastatic Melanoma. Cell *165*, 35–44.

56. Mariathasan, S., Turley, S.J., Nickles, D., Castiglioni, A., Yuen, K., Wang, Y., Kadel, E.E., III, Koeppen, H., Astarita, J.L., Cubas, R., et al. (2018). TGFbeta attenuates tumour response to PD-L1 blockade by contributing to exclusion of T cells. Nature *554*, 544–548.

57. Prat, A., Navarro, A., Paré, L., Reguart, N., Galván, P., Pascual, T., Martínez, A., Nuciforo, P., Comerma, L., Alos, L., et al. (2017). Immune-Related Gene Expression Profiling After PD-1 Blockade in Non-Small Cell Lung Carcinoma, Head and Neck Squamous Cell Carcinoma, and Melanoma. Cancer Res. *77*, 3540–3550.

58. Nathanson, T., Ahuja, A., Rubinsteyn, A., Aksoy, B.A., Hellmann, M.D., Miao, D., Van Allen, E., Merghoub, T., Wolchok, J.D., Snyder, A., et al. (2017). Somatic Mutations and Neoepitope Homology in Melanomas Treated with CTLA-4 Blockade. Cancer Immunol. Res. *5*, 84–91.

59. Lauss, M., Donia, M., Harbst, K., Andersen, R., Mitra, S., Rosengren, F., Salim, M., Vallon-Christersson, J., Törngren, T., Kvist, A., et al. (2017). Mutational and putative neoantigen load predict clinical benefit of adoptive T cell therapy in melanoma. Nat. Commun. *8*, 1738.

60. Kim, S.T., Cristescu, R., Bass, A.J., Kim, K.M., Odegaard, J.I., Kim, K., Liu, X.Q., Sher, X., Jung, H., Lee, M., et al. (2018). Comprehensive molecular characterization of clinical responses to PD-1 inhibition in metastatic gastric cancer. Nat. Med. *24*, 1449–1458.

61. Zhu, A.X., Abbas, A.R., de Galarreta, M.R., Guan, Y., Lu, S., Koeppen, H., Zhang, W., Hsu, C.H., He, A.R., Ryoo, B.Y., et al. (2022). Molecular correlates of clinical response and resistance to atezolizumab in combination with bevacizumab in advanced hepatocellular carcinoma. Nat. Med. *28*, 1599–1611.

62. Voabil, P., de Bruijn, M., Roelofsen, L.M., Hendriks, S.H., Brokamp, S., van den Braber, M., Broeks, A., Sanders, J., Herzig, P., Zippelius, A., et al. (2021). An ex vivo tumor fragment platform to dissect response to PD-1 blockade in cancer. Nat. Med. *27*, 1250–1261.

63. Liu, Z., and Zhang, Z. (2022). Mapping cell types across human tissues. Science *376*, 695–696.

64. Cheng, S., Li, Z., Gao, R., Xing, B., Gao, Y., Yang, Y., Qin, S., Zhang, L., Ouyang, H., Du, P., et al. (2021). A pan-cancer single-cell transcriptional atlas of tumor infiltrating myeloid cells. Cell *184*, 792–809.e23.

65. Zheng, L., Qin, S., Si, W., Wang, A., Xing, B., Gao, R., Ren, X., Wang, L., Wu, X., Zhang, J., et al. (2021). Pan-cancer single-cell landscape of tumor-infiltrating T cells. Science *374*, abe6474.

66. Ballesteros, I., Rubio-Ponce, A., Genua, M., Lusito, E., Kwok, I., Fernández-Calvo, G., Khoyratty, T.E., van Grinsven, E., González-Hernández, S., Nicolás-Ávila, J.Á., et al. (2020). Co-option of Neutrophil Fates by Tissue Environments. Cell *183*, 1282–1297.e18.

67. Chen, D.S., and Mellman, I. (2013). Oncology meets immunology: the cancer-immunity cycle. Immunity *39*, 1–10.

68. Bandola-Simon, J., and Roche, P.A. (2019). Dysfunction of antigen processing and presentation by dendritic cells in cancer. Mol. Immunol. *113*, 31–37.

69. Singhal, S., Bhojnagarwala, P.S., O'Brien, S., Moon, E.K., Garfall, A.L., Rao, A.S., Quatromoni, J.G., Stephen, T.L., Litzky, L., Deshpande, C., et al. (2016). Origin and Role of a Subset of Tumor-Associated Neutrophils with Antigen-Presenting Cell Features in Early-Stage Human Lung Cancer. Cancer Cell *30*, 120–135. https://doi.org/10.1016/j.ccell.2016.06.001.

70. Mysore, V., Cullere, X., Mears, J., Rosetti, F., Okubo, K., Liew, P.X., Zhang, F., Madera-Salcedo, I., Rosenbauer, F., Stone, R.M., et al. (2021). FcγR engagement reprograms neutrophils into antigen cross-presenting cells that elicit acquired anti-tumor immunity. Nat. Commun. *12*, 4791.

71. Hu, Z., Zhao, T.V., Huang, T., Ohtsuki, S., Jin, K., Goronzy, I.N., Wu, B., Abdel, M.P., Bettencourt, J.W., Berry, G.J., et al. (2022). The transcription factor RFX5 coordinates antigen-presenting function and resistance to nutrient stress in synovial macrophages. Nat. Metab. *4*, 759–774.

72. Liu, P.S., Chen, Y.T., Li, X., Hsueh, P.C., Tzeng, S.F., Chen, H., Shi, P.Z., Xie, X., Parik, S., Planque, M., et al. (2023). CD40 signal rewires fatty acid and glutamine metabolism for stimulating macrophage anti-tumorigenic functions. Nat. Immunol. *24*, 452–462.

73. Qian, J., Olbrecht, S., Boeckx, B., Vos, H., Laoui, D., Etlioglu, E., Wauters, E., Pomella, V., Verbandt, S., Busschaert, P., et al. (2020). A pan-cancer blueprint of the heterogeneous tumor microenvironment revealed by single-cell profiling. Cell Res. *30*, 745–762. https://doi.org/10.1038/s41422-020-0355-0.

74. Chan, J.M., Quintanal-Villalonga, Á., Gao, V.R., Xie, Y., Allaj, V., Chaudhary, O., Masilionis, I., Egger, J., Chow, A., Walle, T., et al. (2021). Signatures of plasticity, metastasis, and immunosuppression in an atlas of human small cell lung cancer. Cancer Cell *39*, 1479–1496.e18. https://doi.org/10.1016/j.ccell.2021.09.008.

75. Yang, L., He, Y.-T., Dong, S., Wei, X.-W., Chen, Z.-H., Zhang, B., Chen, W.-D., Yang, X.-R., Wang, F., Shang, X.-M., et al. (2022). Single-cell transcriptome analysis revealed a suppressive tumor immune microenvironment

in EGFR mutant lung adenocarcinoma. J. Immunother. Cancer *10*, e003534. https://doi.org/10.1136/jitc-2021-003534.

76. Hu, S., Lu, H., Xie, W., Wang, D., Shan, Z., Xing, X., Wang, X.-M., Fang, J., Dong, W., Dai, W., et al. (2022). TDO2+ myofibroblasts mediate immune suppression in malignant transformation of squamous cell carcinoma. J. Clin. Invest. *132*, e157649. https://doi.org/10.1172/JCI157649.
77. Jones, R.C., Karkanias, J., Krasnow, M.A., Pisco, A.O., Quake, S.R., Salzman, J., Yosef, N., Bulthaup, B., Brown, P., et al.; Tabula Sapiens Consortium (2022). The Tabula Sapiens: A multiple-organ, single-cell transcriptomic atlas of humans. Science *376*, eabl4896. https://doi.org/10.1126/science.abl4896.
78. Butler, A., Hoffman, P., Smibert, P., Papalexi, E., and Satija, R. (2018). Integrating single-cell transcriptomic data across different conditions, technologies, and species. Nat. Biotechnol. *36*, 411–420.
79. Korsunsky, I., Millard, N., Fan, J., Slowikowski, K., Zhang, F., Wei, K., Baglaenko, Y., Brenner, M., Loh, P.R., and Raychaudhuri, S. (2019). Fast, sensitive and accurate integration of single-cell data with Harmony. Nat. Methods *16*, 1289–1296.
80. Kinker, G.S., Greenwald, A.C., Tal, R., Orlova, Z., Cuoco, M.S., McFarland, J.M., Warren, A., Rodman, C., Roth, J.A., Bender, S.A., et al. (2020). Pan-cancer single-cell RNA-seq identifies recurring programs of cellular heterogeneity. Nat. Genet. *52*, 1208–1218.
81. Hafemeister, C., and Satija, R. (2019). Normalization and variance stabilization of single-cell RNA-seq data using regularized negative binomial regression. Genome Biol. *20*, 296.
82. Andreatta, M., and Carmona, S.J. (2021). UCell: Robust and scalable single-cell gene signature scoring. Comput. Struct. Biotechnol. J. *19*, 3796–3798.
83. Kanehisa, M., Furumichi, M., Tanabe, M., Sato, Y., and Morishima, K. (2017). KEGG: new perspectives on genomes, pathways, diseases and drugs. Nucleic Acids Res. *45*, D353–D361.
84. Liberzon, A., Birger, C., Thorvaldsdóttir, H., Ghandi, M., Mesirov, J.P., and Tamayo, P. (2015). The Molecular Signatures Database (MSigDB) hallmark gene set collection. Cell Syst. *1*, 417–425.
85. Ashburner, M., Ball, C.A., Blake, J.A., Botstein, D., Butler, H., Cherry, J.M., Davis, A.P., Dolinski, K., Dwight, S.S., Eppig, J.T., et al. (2000). Gene ontology: tool for the unification of biology. The Gene Ontology Consortium. Nat. Genet. *25*, 25–29.
86. Linderman, G.C., Zhao, J., Roulis, M., Bielecki, P., Flavell, R.A., Nadler, B., and Kluger, Y. (2022). Zero-preserving imputation of single-cell RNA-seq data. Nat. Commun. *13*, 192.
87. Efremova, M., Vento-Tormo, M., Teichmann, S.A., and Vento-Tormo, R. (2020). CellPhoneDB: inferring cell-cell communication from combined expression of multi-subunit ligand-receptor complexes. Nat. Protoc. *15*, 1484–1506.
88. Goldman, M.J., Craft, B., Hastie, M., Repečka, K., McDade, F., Kamath, A., Banerjee, A., Luo, Y., Rogers, D., Brooks, A.N., et al. (2020). Visualizing and interpreting cancer genomics data via the Xena platform. Nat. Biotechnol. *38*, 675–678.
89. Chen, B., Khodadoust, M.S., Liu, C.L., Newman, A.M., and Alizadeh, A.A. (2018). Profiling Tumor Infiltrating Immune Cells with CIBERSORT. Methods Mol. Biol. *1711*, 243–259.
90. Yoshihara, K., Shahmoradgoli, M., Martínez, E., Vegesna, R., Kim, H., Torres-Garcia, W., Treviño, V., Shen, H., Laird, P.W., Levine, D.A., et al. (2013). Inferring tumour purity and stromal and immune cell admixture from expression data. Nat. Commun. *4*, 2612.
91. Charoentong, P., Finotello, F., Angelova, M., Mayer, C., Efremova, M., Rieder, D., Hackl, H., and Trajanoski, Z. (2017). Pan-cancer Immunogenomic Analyses Reveal Genotype-Immunophenotype Relationships and Predictors of Response to Checkpoint Blockade. Cell Rep. *18*, 248–262.
92. Li, B., Severson, E., Pignon, J.C., Zhao, H., Li, T., Novak, J., Jiang, P., Shen, H., Aster, J.C., Rodig, S., et al. (2016). Comprehensive analyses of tumor immunity: implications for cancer immunotherapy. Genome Biol. *17*, 174.
93. Racle, J., de Jonge, K., Baumgaertner, P., Speiser, D.E., and Gfeller, D. (2017). Simultaneous enumeration of cancer and immune cell types from bulk tumor gene expression data. eLife *6*.
94. Lee, B.T., Barber, G.P., Benet-Pagès, A., Casper, J., Clawson, H., Diekhans, M., Fischer, C., Gonzalez, J.N., Hinrichs, A.S., Lee, C.M., et al. (2022). The UCSC Genome Browser database: 2022 update. Nucleic Acids Res. *50*, D1115–D1122.
95. Lin, J., Dai, Y., Sang, C., Song, G., Xiang, B., Zhang, M., Dong, L., Xia, X., Ma, J., Shen, X., et al. (2022). Multimodule characterization of immune subgroups in intrahepatic cholangiocarcinoma reveals distinct therapeutic vulnerabilities. J. Immunother. Cancer *10*.
96. Song, G., Shi, Y., Meng, L., Ma, J., Huang, S., Zhang, J., Wu, Y., Li, J., Lin, Y., Yang, S., et al. (2022). Single-cell transcriptomic analysis suggests two molecularly subtypes of intrahepatic cholangiocarcinoma. Nat. Commun. *13*, 1642.
97. Ding, G.Y., Ma, J.Q., Yun, J.P., Chen, X., Ling, Y., Zhang, S., Shi, J.Y., Chang, Y.Q., Ji, Y., Wang, X.Y., et al. (2022). Distribution and density of tertiary lymphoid structures predict clinical outcome in intrahepatic cholangiocarcinoma. J. Hepatol. *76*, 608–618.
98. Ye, Y., Chen, Z., Jiang, S., Jia, F., Li, T., Lu, X., Xue, J., Lian, X., Ma, J., Hao, P., et al. (2022). Single-cell profiling reveals distinct adaptive immune hallmarks in MDA5+ dermatomyositis with therapeutic implications. Nat. Commun. *13*, 6458.
99. Shen, X., Wang, C., Liang, N., Liu, Z., Li, X., Zhu, Z.J., Merriman, T.R., Dalbeth, N., Terkeltaub, R., Li, C., et al. (2021). Serum Metabolomics Identifies Dysregulated Pathways and Potential Metabolic Biomarkers for Hyperuricemia and Gout. Arthritis Rheumatol. *73*, 1738–1748.
100. Wang, Z., Lu, Z., Lin, S., Xia, J., Zhong, Z., Xie, Z., Xing, Y., Qie, J., Jiao, M., Li, Y., et al. (2022). Leucine-tRNA-synthase-2-expressing B cells contribute to colorectal cancer immunoevasion. Immunity *55*, 1748.
101. Zhang, M., Huang, Y., Pan, J., Sang, C., Lin, Y., Dong, L., Shen, X., Wu, Y., Song, G., Ji, S., et al. (2023). An Inflammatory Checkpoint Generated by IL1RN Splicing Offers Therapeutic Opportunity for KRAS-Mutant Intrahepatic Cholangiocarcinoma. Cancer Discov. *13*, 2248–2269.
102. Wu, Y., Zhao, J., Zhu, H., Fan, Z., Yuan, X., Chen, S., Mao, R., and Fan, Y. (2020). SPACE: a web server for linking chromatin accessibility with clinical phenotypes and the immune microenvironment in pan-cancer analysis. Cell. Mol. Immunol. *17*, 1294–1296.
103. Wu, Y., Yang, Y., Gu, H., Tao, B., Zhang, E., Wei, J., Wang, Z., Liu, A., Sun, R., Chen, M., et al. (2020). Multi-omics analysis reveals the functional transcription and potential translation of enhancers. Int. J. Cancer *147*, 2210–2224.

STAR★METHODS

KEY RESOURCES TABLE

REAGENT or RESOURCE	SOURCE	IDENTIFIER
Antibodies		
Biotin anti-human CD66b antibody, Clone G10F5	BioLegend	Cat#305120, RRID: AB_2566608
PE anti-human CD66b antibody, Clone G10F5	BioLegend	Cat#305105, RRID: AB_10550093
HLA-DR anti-human antibody, Clone LN3	Thermo Fisher	Cat#14-9956, RRID: AB_468638
CD15 anti-human antibody	Abnova	Cat#MAB-0015
Rabbit Cd74 antibody, reacts with: mouse, Clone EPR25399-94	Abcam	Cat#ab289885
Rabbit Ly6G antibody, reacts with: mouse, Clone EPR22909-135	Abcam	Cat#ab238132
Biotin anti-human CD3 antibody, Clone UCHT1	Biolegend	Cat#300404, RRID: AB_314058
PerCP/Cyanine5.5 anti-human CD66b antibody, Clone G10F5	Biolegend	Cat#305108, RRID: AB_2077855
PE anti-human CD66b antibody, Clone G10F5	Biolegend	Cat#305105, RRID: AB_10550093
FITC anti-human CD66b antibody, Clone G10F5	Biolegend	Cat#305104, RRID: AB_314496
Brilliant Violet 421™ anti-human HLA-DR antibody, Clone L243	Biolegend	Cat#307636, RRID: AB_2561831
eFluor660 anti-human Osteopontin (SPP1) antibody, Clone 2F10	Invitrogen	Cat#50-9096-41
Alexa Fluor(R) 488 anti-human CD182 (CXCR2) antibody, Clone 5E8/CXCR2	Biolegend	Cat#320712, RRID: AB_492938
PEcy5 anti-human CD62L antibody, Clone DREG-56	Invitrogen	Cat#1946541
PE anti-human CD54 (ICAM1) antibody, Clone HCD54	Biolegend	Cat#322708, RRID: AB_535980
APC anti-human CD3 antibody, Clone UCHT1	Biolegend	Cat#300458, RRID: AB_2564151
Brilliant Violet 785™ anti-human CD8a antibody, Clone RPA-T8	Biolegend	Cat#301046, RRID: AB_2563264
APC/Fire™ 750 anti-human CD4 antibody, Clone SK3	Biolegend	Cat#344638, RRID: AB_2572097
PE/Dazzle™ 594 anti-human/mouse Granzyme B Recombinant antibody, Clone QA16A02	Biolegend	Cat#372216, RRID: AB_2728383
Brilliant Violet 711™ anti-human IFN-gamma antibody, Clone 4S.B3	Biolegend	Cat#502539, RRID: AB_11218602
BV650 TNF-α antibody, MAb11	BD	Cat#563418, RRID: AB_2738194
FITC anti-human 4-1BB (CD137) antibody, Clone 4B4	eBioscience	Cat#11-1379-42
BV605 anti-human CD69 antibody, Clone FN50	BD	Cat#562989, RRID: AB_2737935
Histone H3 (D1H2) XP®Rabbit mAb(Alexa Fluor®647 Conjugate) antibody, Clone D1H2	Cell Signaling	Cat#12230S, RRID: AB_2797852
Acetyl-Histone H3 (Lys27) (D5E4) XP® Rabbit mAb (Alexa Fluor® 647 Conjugate) antibody, Clone D5E4	Cell Signaling	Cat#39030S, RRID: AB_2799145
FITC-conjugated OVA	Sangon	Cat#D110528
PE anti-mouse Ly-6G antibody, Clone 1A8	Biolegend	Cat#127608, RRID: AB_1186099
Alexa Fluor(R) 488 anti-mouse CD74 (CLIP) antibody, Clone In1/CD74	Biolegend	Cat#151006, RRID: AB_2750326
Alexa Fluor(R) 647 anti-mouse CD74 (CLIP) antibody, Clone In1/CD74	Biolegend	Cat#151004, RRID: AB_2632609

(*Continued on next page*)

Continued

REAGENT or RESOURCE	SOURCE	IDENTIFIER
FITC Anti-Mouse Cd45 antibody	Tonbo	Cat#35-0451-U025
Alexa Fluor® 700 anti-mouse CD3 antibody	BD	Cat#561388, RRID: AB_10642588
BV711 anti-mouse Cd8a antibody, Clone 53-6.7	BD	Cat#563046, RRID: AB_2737972
PEcy5 anti-mouse Cd4 antibody, Clone RM4-5	BD	Cat#553050, RRID: AB_394586
APC anti-mouse CD62L (L-Selectin) antibody, Clone MEL-14	eBioscience	Cat#17-0621-83, RRID: AB_469411
PE/Cyanine7 anti-mouse CD19 antibody, Clone 6D5	Biolegend	Cat#115519, RRID: AB_313654
BV395 anti-mouse Cd11b antibody, Clone M1/70	BD	Cat#563553, RRID: AB_2738276
PerCP-Cyanine5.5 anti-mouse Ly6C antibody, Clone HK1.4	eBioscience	Cat#45-5932-82, RRID: AB_2723343
Brilliant Violet 785™ anti-mouse F4/80 antibody, Clone BM8	Biolegend	Cat#123141, RRID: AB_2563667
Brilliant Violet 421™ anti-mouse CD279 (PD-1) antibody, Clone 29F.1A12	Biolegend	Cat#135221, RRID: AB_2562568
PE-Cyanine5.5 anti-mouse CD11c antibody, Clone N418	eBioscience	Cat#35-0114-82, RRID: AB_469709
Emapalumab (anti-IFNγ) antibody	Selleck	Cat#A2041
TNFα neutralizing antibody	Sino Biological	Cat#10602-MM0N1
IL-6 neutralizing antibody	Sino Biological	Cat#10395-R508
IL-17 neutralizing antibody	Sino Biological	Cat#12047-M237
IL-23 neutralizing antibody	Sino Biological	Cat#CT035-mh066
Ultra-LEAF™ Purified anti-mouse CD279 (PD-1), Clone 29F.1A12	BioLegend	Cat#135248
Ultra-LEAF™ Purified Rat IgG2a, κ Isotype Ctrl	BioLegend	Cat#400565
InVivoPlus anti-mouse Ly6G/Ly6C (Gr-1) antibody, clone RB6-8C5	Bio X Cell	Cat#BE0075, RRID: AB_10312146
Chemicals, peptides, and recombinant proteins		
Alanine	Sangon	Cat#A600022-0100
Arginine	Sangon	Cat#A600205-0100
Asparagine	Sangon	Cat#A694341-0100
Aspartate	Sangon	Cat#A600091-0250
Cysteine	Sangon	Cat#A600132-0100
Glutamine	Sangon	Cat#A100374-0050
Glutamate	Sangon	Cat#A600221-0500
Glycine	Sangon	Cat#A610235-0500
Histidine	Sangon	Cat#A604351-0050
Isoleucine	Sangon	Cat#A100803-0050
Leucine	Sangon	Cat#A600922-0100
Lysine	Sangon	Cat#A602759-0025
Methionine	Sangon	Cat#A610346-0100
Phenylalanine	Sangon	Cat#A600991-0025
Proline	Sangon	Cat#A600923-0100
Serine	Sangon	Cat#A601479-0100
Threonine	Sangon	Cat#A610919-0100
Tryptophan	Sangon	Cat#A601911-0050
Tyrosine	Sangon	Cat#A601932-0100
Valine	Sangon	Cat#A600172-0025
L-Leucine-$^{13}C_6$	Sigma	Cat#605239
Dichloroacetate	Sigma	Cat#2156-56-1

(*Continued on next page*)

Continued

REAGENT or RESOURCE	SOURCE	IDENTIFIER
ACSS2-IN-2	MCE	Cat#2332820-04-7
TMRE Fluorescent Mitochondrial Probe	Sigma	Cat#87917-25MG
NAO nonyl bromide	Sigma	Cat#A7847-100MG
Fluo 3	Sigma	Cat#73881-1MG
JC1	AAT Bioquest	Cat#22200
Brite™ HPF *Optimized for Detecting Reactive Oxygen Species (ROS)	AAT Bioquest	Cat#16051
Trizol	Thermo Fisher Scientific	Cat#15596018
NEBNext UltraTM RNA Library Prep Kit	NEB	Cat#E7490
Collagenase IV	STEMCELL technologies	Cat#07909_C
RPMI1640	Gibco	Cat#11875500BT
Peptide VVRHCPHHERCSDSD	China Peptides Inc.	N/A
Peptide QHMTEVVRHCPHHER	China Peptides Inc.	N/A
Peptide RNTFRHSVVVPCE	China Peptides Inc.	N/A
Peptide NTFRHSVVVPCEPPE	China Peptides Inc.	N/A
Peptide HYNYMCNSSCMGSMN	China Peptides Inc.	N/A
Peptide MTEYKLVVVGAVGVGKSALTIQLI	China Peptides Inc.	N/A
Peptide LVVVGADGV	China Peptides Inc.	N/A
Peptide SQEQPRCHY	China Peptides Inc.	N/A
Peptide RLFERDGLKV	China Peptides Inc.	N/A
Peptide LVVVGADGV	China Peptides Inc.	N/A
Peptide gp100 (44-59)	China Peptides Inc.	N/A
Peptide CMV (6571)	China Peptides Inc.	N/A
MHC class II antigen presentation Gene Expression PCR Array	Wcgene biotech	Cat#WC-MRNA0283-H
MHC class I antigen presentation Gene Expression PCR Array	Wcgene biotech	Cat#WC-MRNA0282-H
DAPI	BioLegend	Cat#422801
Critical commercial assays		
Chromium™ Single Cell 5′ Library Construction Kit	10x Genomics	Cat#1000020
Chromium™ Next GEM Single Cell 5′ Library and Gel Bead Kit v1.1	10x Genomics	Cat#1000165
MojoSort™ Whole Blood Human Neutrophil Isolation Kit	BioLegend	Cat#480152
Anti-Biotin MicroBeads	Miltenyi Biotec	Cat#130-090-485
EasySep™ Direct Human PBMC Isolation Kit	StemCell Technologies	Cata#19654
Chromium Next GEM Single Cell 3′ Kit v3.1	10x Genomics	Cat#1000268
KC-digital™ stranded TCR-seq library prep kit	Seqhealth Technology Co., Ltd	Cat#DT0813-02
Experimental models: Cell line		
Human: HepG2 cells	Cell Bank of Type Culture Collection Chinese Academy of Sciences (CBTCCCAS)	SCSP-510
Human: A549 cells	CBTCCCAS	SCSP-503
Human: HCT116 cells	CBTCCCAS	SCSP-5076
Human: PANC1 cells	CBTCCCAS	SCSP-535
Human: MCF7 cells	CBTCCCAS	SCSP-531
Human: dHL-60 cells	Genomeditech Co. Ltd.	N/A
Mouse: MC38 cells	Shanghai Model Organisms Center	N/A
Mouse: Hepa 1–6 cells	Shanghai Model Organisms Center	N/A

(*Continued on next page*)

Continued

REAGENT or RESOURCE	SOURCE	IDENTIFIER
Mouse: LLC cells	Shanghai Model Organisms Center	N/A
Experimental models: Organisms/strains		
Mouse: C57BL/6J wildtype	Shanghai Model Organisms Center	SM-001
Mouse: C57BL/6J Cd45.1	Shanghai Model Organisms Center	NM-KI-210226
Mouse: C57BL/6J Cd74-KO	Shanghai Model Organisms Center	NM-KO-200715
Mouse: C57BL/6J MHC-II$^{flox/flox}$	Nanjing GemPharmatech Co. Ltd.	T019085
Mouse: C57BL/6J Ly6G$^{Cre-tdTomato}$	Shanghai Model Organisms Center	NM-KI-200219
Mouse: C57BL/6J Lat1(Slc7a5)-KO	Nanjing GemPharmatech Co. Ltd.	T031657
Mouse: C57BL/6J Bcat2-KO	Nanjing GemPharmatech Co. Ltd.	T049844
Mouse: C57BL/6J Dbt-KO	Nanjing GemPharmatech Co. Ltd.	T031427
Biological samples		
Neutrophil in-house single-cell RNA-seq data (n = 155; 103 samples were newly generated data)	Zhongshan Hospital, Fudan University Summarized in Table S1	N/A
Neutrophil single-cell RNA-seq data derived from public data (n = 70, cancer patients; n = 5, healthy donor)	Summarized in Table S1	N/A
Spatial transcriptomics data derived from public data (n = 50)	Summarized in Table S5	N/A
Tissue microarray (8-Cancer-TMA) cohort with survival information (n = 1,116)	Zhongshan Hospital, Fudan University; Shanghai Outdo Biotech Co. Ltd. Summarized in Table S1	N/A
Tissue microarray (Multi-Cancer-TMA) cohort (n = 68)	Shanghai Outdo Biotech Co. Ltd. Summarized in Table S1	N/A
Blood from healthy donor (n = 44)	Zhongshan Hospital, Fudan University	N/A
Hepatocellular carcinoma samples treated with neoadjuvant immunotherapy (n = 5)	Zhongshan Hospital, Fudan University	N/A
Deposited data		
scRNA-Seq of neutrophils	This paper	PRJCA020880; http://pancancer.cn/neu
scRNA-Seq of neutrophils	Qian, J. et al.[73]	E-MTAB-8107, E-MTAB-6149 and E-MTAB-6653
scRNA-Seq of neutrophils	Chan, J. et al.[74]	Human Tumor Atlas Network (HTAN)
scRNA-Seq of neutrophils	Yang, L. et al.[75]	GSE171145
scRNA-Seq of neutrophils	Zilionis et al.[23]	GSE127465
scRNA-Seq of neutrophils	Wang et al.[25]	OEP003254
scRNA-Seq of neutrophils	Hu, S. et al.[76]	HRA001006
scRNA-Seq of neutrophils	Xue et al.[7]	PRJCA007744
scRNA-Seq of neutrophils	Tabula Sapiens Consortium et al.[77]	GSE201333
Spatial transcriptomics	Summarized in Table S5	10X Genomics website; http://lifeome.net/supp/livercancer-st/data.htm; https://zenodo.org/record/4739739; GSE144239; GSE175540
RNA-seq for inferring the neutrophil consensus infiltration	The Cancer Genome Atlas	N/A
RNA-seq for inferring the neutrophil consensus infiltration	Clinical Proteomic Tumor Analysis Consortium	N/A
RNA-seq of neutrophils (leucine treatment and control)	This paper	PRJCA020880

(*Continued on next page*)

Continued

REAGENT or RESOURCE	SOURCE	IDENTIFIER
ATAC-seq of neutrophils (leucine treatment and control)	This paper	PRJCA020880
CUT&Tag of neutrophils (leucine treatment and control)	This paper	PRJCA020880
TCR-seq (antigen-presenting neutrophil stimulating T-cell response)	This paper	PRJCA020880
scRNA-Seq of mouse tumors	Summarized in Table S5	N/A
RNA-seq of immunotherapy-treated samples (SKCM)	Gide et al.[54]	PRJEB23709
RNA-seq of immunotherapy-treated samples (SKCM)	Hugo et al.[55]	GSE78220
RNA-seq of immunotherapy-treated samples (BLCA)	Mariathasan et al.[56]	EGAS00001002556
RNA-seq of immunotherapy-treated samples (NSCLC)	Prat et al.[57]	GSE93157
RNA-seq of immunotherapy-treated samples (SKCM)	Nathanson et al.[58]	N/A
RNA-seq of immunotherapy-treated samples (SKCM)	Lauss et al.[59]	GSE100797
RNA-seq of immunotherapy-treated samples (STAD)	Kim et al.[60]	PRJEB25780
RNA-seq of immunotherapy-treated samples (HCC)	Zhu et al.[61]	EGAS00001005503
Software and algorithms		
CellRanger V7	10x Genomics	https://10xgenomics.com
Seurat V4.0.4	CRAN	https://cran.r-project.org/web/packages/Seurat/index.html
harmony V0.1.0	CRAN	https://cran.r-project.org/web/packages/harmony/index.html
ggplot2 V3.3.5	CRAN	https://cran.r-project.org/web/packages/ggplot2/index.html
dittoSeq V1.5.2	Bioconductor	https://bioconductor.org/packages/dittoSeq/
GSVA V1.40.1	Bioconductor	https://www.bioconductor.org/packages/GSVA/
Monocle3 V1.0.0	Github	https://github.com/cole-trapnell-lab/monocle3
shiny V1.6.0	CRAN	https://cran.r-project.org/package=shiny
TooManyCells V2.0.0.0	github	https://github.com/GregorySchwartz/too-many-cells
SingleR V1.7.1	Bioconductor	https://bioconductor.org/packages/SingleR
ggpubr V0.4.0	CRAN	https://cran.r-project.org/package=ggpubr
ggsignif V0.6.3	CRAN	https://cran.r-project.org/web/packages/ggsignif/index.html
pheatmap V1.0.12	CRAN	https://cran.r-project.org/web/packages/pheatmap/index.html
ComplexHeatmap V2.15.1	Bioconductor	https://bioconductor.org/packages/release/bioc/html/ComplexHeatmap.html
cowplot V1.1.1	CRAN	https://cran.r-project.org/web/packages/cowplot/index.html
sctour V0.1.3	Pypi	https://pypi.org/project/sctour/
xCell V1.1.0	Github	https://github.com/dviraran/xCell
dorothea V1.10.0	Bioconductor	https://bioconductor.org/packages/release/data/experiment/html/dorothea.html

(*Continued on next page*)

Continued

REAGENT or RESOURCE	SOURCE	IDENTIFIER
UCell V1.3.1	Bioconductor	https://bioconductor.org/packages/release/bioc/html/UCell.html
ScMetabolism	Github	https://github.com/wu-yc/scMetabolism
doubletFinder V2.0.3	Github	https://github.com/chris-mcginnis-ucsf/DoubletFinder
Other		
Code	This paper	https://github.com/wu-yc/neutrophil (https://doi.org/10.5281/zenodo.10531210)
ScProgram	This paper	https://github.com/wu-yc/scProgram (https://doi.org/10.5281/zenodo.10531218)

RESOURCE AVAILABILITY

Lead contact

Further information and requests for resources and reagents should be directed to and will be fulfilled by the lead contact, Qiang Gao (gaoqiang@fudan.edu.cn).

Materials availability

This study did not generate new unique reagents.

Data and code availability

- Processed gene expression data can be queried and downloaded at http://www.pancancer.cn/neu and raw sequencing data are available at the China National Center for Bioinformation (accession: PRJCA020880) with the permission at Human Genetic Resources Service System of Ministry of Science and Technology. To request access to raw sequencing data, please apply at Human Genetic Resources Service System of Ministry of Science and Technology (https://apply.hgrg.net/) according to the law of Regulations on management of human genetic resources of China. This paper analyzed existing, publicly available data, where the accession numbers are listed in the key resources table.
- All original code has been deposited at GitHub and Zenodo and is available at https://github.com/wu-yc/neutrophil (https://doi.org/10.5281/zenodo.10531210) and https://github.com/wu-yc/scProgram (https://doi.org/10.5281/zenodo.10531218).
- Any additional information required to reanalyze the data reported in this paper is available from the lead contact upon request.

EXPERIMENTAL MODEL AND STUDY PARTICIPANT DETAILS

Patient inclusion and sample collection

We collected fresh samples from Zhongshan Hospital Fudan University with written consent and approval from the Institutional Review Board-approved protocols (B2021-381, B2021-084, B2020-348R, B2023-350). After quality control, a total of 103 samples from 64 patients were included in the analyses. The median age of the patients was 59.6 years, and the cohort consisted of 26 females and 38 males, and the detailed information was included in Table S1. Patient inclusion criteria were as follows: Patients with treatment-naïve primary tumors who underwent surgery; patients without major underlying diseases that may seriously affect neutrophils (such as autoimmune diseases and acute infection). The 8-Cancer-TMA (n = 1,116; diameter: 1.5 mm; sample information see Table S1) and Multi-Cancer-TMA (n = 68; diameter: 1.5 mm; tumor and peritumor samples) were from the patients from Zhongshan Hospital Fudan University and Shanghai Outdo Biotech (Table S1) and approval from Shanghai Outdo Biotech Ethics Committee (SHYJS-CP-2210040, SHYJS-CP-1910002, SHYJS-CP-1804011, SHYJS-CP-1510001, SHYJS-CP-1701016, SHYJS-CP-1404018). As for PDTF analysis, samples from 5 HCC patients with pathologic nonresponse (residual viable tumor rates of 95%, 95%, 90%, 90%, and 90% respectively; treatment: anti-PD-1 plus anti-VEGF agent) were included.

Mouse models

5-week-old male C57BL/6 mice, CD74 KO, CD45.1 mice, and Ly6G$^{Cre\text{-}tdTomato}$ were obtained from the Shanghai Model Organisms Center, Inc. MHC-II$^{flox/flox}$ mice, LAT1^{KO}, Bcat2^{KO}, Dbt^{KO} mice were obtained from Nanjing GemPharmatech Co. Ltd. We housed them under pathogen-free conditions with a maximum of five mice per cage. We strictly adhered to animal care principles and ethics and received approval from the Institutional Animal Care and Use Committee of the Shanghai Model Organisms Center (approval number 2019-0011).

METHOD DETAILS

Standardized cell sorting protocol

Tumor and matched normal samples were dissected into small pieces with a diameter < 1mm, and dissociated using Collagenase IV (STEMCELL technologies; 07909_C) plus 0.4 mg/mL hyaluronidase in RPMI 1640 (Gibco; 11875093) with a GentleMACS Dissociator for 60 minutes. The resulting cells were filtered through a 400 μm filter and washed with DPBS (500g and 10 minutes). To isolate $CD66b^+$ neutrophils, we employed a two-step sorting strategy. First, cells were stained with CD66b Biotin antibody (Biolegend, 305120), and then sorted with MS columns (Miltenyi Biotec, 130-042-201). Next, cells were stained with CD66b PE antibody (Biolegend, 305105) and sorted again by flow cytometry (BD FACS Aria II). Sorted cells were immediately sent for single-cell RNA sequencing. For samples with a sufficient number of cells, we also sorted $CD45^+$ cells and sequenced them. As for the neutrophils derived from blood, we incubated the peripheral blood with red blood cell lysis buffer (Sangon, B541001) for 10 minutes and washed it with DPBS (500g and 10 minutes). The resulting cell suspension was then stained with CD66b PE antibody (Biolegend, 305105) and sorted using flow cytometry (BD FACS Aria II).

Single-cell sequencing

The sorted cells were sequenced using the 10x Chromium single-cell platform with 5′ Reagent Kits following the manufacturer's protocol. Single-cell libraries were then sequenced on the NovaSeq platform from Illumina. To trace the sample source, we used TotalSeq C from BioLegend (399905), which allowed us to distinguish between tumor, adjacent normal, and blood cells. CellRanger V7 was used for processing the barcodes, aligning the data, and generating initial clusters of the raw scRNA-seq profiles.

ScRNA-seq data quality control, processing, annotation, and visualization

Raw fastq files were firstly aligned to human genome (GRCh38, ENSEMBL) by CellRanger V7 following the 10X Genomics neutrophil tutorial (https://support.10xgenomics.com/single-cell-gene-expression/software/pipelines/latest/tutorials/neutrophils), we retained the intronic regions by using the parameter of "–include-introns" and set the "–force-cells=20000" in CellRanger. We then used Seurat (V4.0.4)[78] to process the UMI count matrix. We performed doublet removal by using doubletFinder (V2.0.3). The mitochondrial gene percentage was assessed by PercentageFeatureSet(object, pattern = "MT-") function and cells with mitochondrial gene percentage over 10% were removed. Excluding genes in a blacklist as described before,[65] the top 5000 genes were identified as highly variable genes (HVG) using FindVariableFeatures function of Seurat.[78] We integrated all cells according to sample ID by using harmony (V0.1.0).[79] We performed clustering analysis and only reserved the neutrophils defined by markers CSF3R, FPR1, FCGR3B, NAMPT, and MNDA following the 10X Genomics neutrophil tutorial. We further used SingleR (V1.7.1) to confirm the input cells are real neutrophils. In the second round of doublet removal, we observed clusters with high expression of CD3D (T cell), CD79A (B cell), and CD68 (macrophage). We next computed the marker genes using FindAllMarker function of Seurat.[78]

Single-cell transcriptional program feature gene analysis and signature quantification

We followed a well-established computational strategy designed for decoding single-cell heterogeneity.[80] In detail, we first normalized the data matrix using scTransform[81] and one-by-one performed NMF analysis (parameter: k = 100). We clustered the Jaccard index of H matrix and visualized it using pheatmap (V1.0.12). We performed the differential gene analysis to find the feature genes of each program. Further gene set enrichment analysis was performed using the highly expressed genes. As for the signature quantification, we used UCell[82] to quantify the signature/pathway activity of neutrophils. KEGG,[83] hallmark,[84] Gene Ontology (GO),[85] and neutrophil immunophenotype signatures[29] were included for analysis. As for the circadian analysis of neutrophil signature, the sampling time refers to the surgery time of tumor samples.

Single-cell HLA-type quantification

We employed scHLAcount (V0.2.0, available at https://github.com/10XGenomics/scHLAcount) with default parameters to count the molecules of class I genes HLA-A, B, and C; and class II genes DPA1, DPB1, DRA1, DRB1, DQA1, and DQB1.

Single-cell metabolism quantification

To explore the featured pathway among $HLA\text{-}DR^+$ neutrophils, we first computed the pathway variance (Gini index, metric entropy, Shannon entropy, and Simpson index). The formula for the Gini index is: G = (2A)/(nB), where G is the Gini index; A is the area between the Lorenz curve and the line of perfect equality of pathway score (the diagonal line from the bottom left to the top right corner of the graph); B is the total area under the line of perfect equality of pathway score; n is the total number of cells. The formula for the Simpson index is: $D = 1 - \Sigma(ni(ni-1))/N(N-1)$, where: D is the Simpson index; ni is the number of cells in a given pathway. The formula for Shannon entropy is: $H = -\Sigma P(x) \log_2 P(x)$, where H is the entropy in bits, P(x) is the probability distribution of pathway scores. The major metabolism subtype quantification was performed using *scMetabolism* as we developed before[37] (parameter: imputation = T, metabolism.type = "KEGG").

Cell-cell communication, cell trajectory, and cell clade analysis

To understand how HLA-DR$^+$ neutrophils interact with T cells, we first performed the down-sampling analysis (to 20,000 cells), impute expression matrix by using ALRA,[86] and used CellPhoneDB[87] to infer the interactions (parameter: cellphonedb method statistical_analysis –iterations=100 –threads=48). We next ranked the ligand expressed on neutrophils by the gene expression proportion and frequency. We used scTour to infer the differentiation state of neutrophils.[32] To validate the trajectory, we next used monocle3,[33] CytoTRACE,[34] and Slingshot[35] to separately infer the pseudotime of neutrophil subsets. To compare the hierarchy difference between neutrophils derived from blood, cancer, and adjacent tissues, we split the expression matrix containing 3000 variable genes and performed clustering analysis using TooManyCells[26] (parameter: make-tree PieRing).

Generating the pan-cancer neutrophil infiltration consensus

We download the gene expression matrix of pan-cancer solid tumors by using UCSC Xena[88] (data type: HTSeq - FPKM-UQ). We first tested 8 common immune quantification algorithms covering CIBERSORT, ESTIMATE, Quantiseq, MCPCounter, IPS, TIMER, EPIC, and xCell.[16–18,89–93] We found that 3 of them support the quantification of neutrophil level (MCPCounter, Quantiseq, and xCell). We clustered the pan-cancer samples according to neutrophil level generated by three algorithms and designed the consensus neutrophil score based on the consensus rank of these scores. In detail, as for the samples ranked at the upper quantile or low quantile in three algorithms, we then label the samples as high or low neutrophil consensus samples. While the samples without reaching the consensus among three algorithms are labeled as heterogeneous samples. We ordered the samples according to the consensus score and rank them according to cancer types. We also performed the dimensional reduction analysis using t-SNE embedded in Seurat[78] and labeled samples according to their neutrophil consensus status.

Transcription factor activity analysis

For scRNA-seq data, we used dorothea (V1.10.0) to infer the transcription factor activity. As for the ChIP-seq of RFX5 transcription factor, we fetched published RFX5 ChIP-seq data (accession number: SRX150635, SRX150644, SRX150384, SRX186620, SRX186634, SRX150462, and SRX150639) and analyzed it using UCSC Genome Browser.[94] The neutrophil-like differentiated HL-60 (dHL-60) cells were obtained by adding 1% DMSO to the HL-60 culture medium for six days.[25] We obtained the knockdown and overexpression plasmids of RFX5 from Genomeditech (Shanghai, China). Empty vector was used as the negative control. Each condition was performed with 3 replicates.

Multiplex immunohistochemistry analysis

We performed the immunohistochemistry using Osteopontin/SPP1 (Abcam; ab214050; species reactivity: Human), HLA-DR (thermofisher; 14-9956; species reactivity: Human), CD15 (MAB-0015; species reactivity: Human), Cd74 (Abcam; ab289885; species reactivity: Mouse), Ly6G (Abcam; ab238132; species reactivity: Mouse), CXCL13 (Abcam; ab246518; species reactivity: Human), CD39 (Abcam; ab300065; species reactivity: Human), CD4 (Biolynx; BX50023; species reactivity: Human), CD8 (Dako; M7103; species reactivity: Human), MPO (Abcam; ab300650; species reactivity: Human), CD11b (Abcam; ab133357; species reactivity: Human), DAPI (BioLegend; 422801) antibodies. We scanned the slides using the PerkinElmer Vectra3 platform and quantified the results by using PerkinElmer Vectra3 platform as previously described.[52,95–97] The 8-Cancer-TMA cohort with matched prognosis metadata (HCC, COAD, NSCLC, STAD, RCC, OV, BRCA, and BLCA) and Multi-Cancer-TMA cohort (PAAD, RCC, HCC, ICC, STAD, NSCLC, BRCA, and COAD) were included. The detailed clinicopathological features were described in Table S1.

Cell culture

We performed Ficoll Paque experiment on blood derived from healthy donors using Ficoll Paque Plus agent (GE, 17-1440-03). Neutrophils were separated by staining with CD66b Biotin antibody (Biolegend, 305120), adding biotin magnetic beads, and sorting with MS columns (Miltenyi Biotec, 130-042-201). T cells were separated by staining with CD3 Biotin antibody (Biolegend, 300404), adding biotin magnetic beads, and sorting with MS columns (Miltenyi Biotec, 130-042-201). Cells (5×10^4) were added to 96-well cell culture plates in a total volume of 200 μL of culture medium. To maintain neutrophil activity, we added Lipopolysaccharides (LPS, MCE, HY-D1056) at a concentration of 100 ng/mL. Additionally, we supplemented the medium with 20 types of amino acids and performed the neutrophil culture for 24 hours (Sangon, A600022-0100, A600205-0100, A694341-0100, A600091-0250, A600132-0100, A100374-0050, A600221-0500, A610235-0500, A604351-0050, A100803-0050, A600922-0100, A602759-0025, A610346-0100, A600991-0025, A600923-0100, A601479-0100, A610919-0100, A601911-0050, A601932-0100, A600172-0025). The concentration of each amino acid was set to match the physiological plasma concentration, as reported by healthmatters.io: Alanine (681 μmol/L), Arginine (137 μmol/L), Asparagine (90 μmol/L), Aspartate (12.6 μmol/L), Cysteine (360 μmol/L), Glutamine (876 μmol/L), Glutamate (214 μmol/L), Glycine (518 μmol/L), Histidine (114 μmol/L), Isoleucine (104 μmol/L), Leucine (196 μmol/L), Lysine (318 μmol/L), Methionine (48 μmol/L), Phenylalanine (95 μmol/L), Proline (363 μmol/L), Serine (172 μmol/L), Threonine (216 μmol/L), Tryptophan (83 μmol/L), Tyrosine (110 μmol/L), Valine (370 μmol/L). Dichloroacetate (mitochondrial acetyl-CoA activator, 0.1 mM; 2156-56-1), ACSS2-IN-2 (acetyl-CoA inhibitor, 5 nM; 2332820-04-7) were used respectively. Each condition was performed with 3-4 replicates. As for the HLA-DR$^+$ neutrophil cocultured with T cells, neutrophils were sorted from samples of hepatocellular carcinoma, colorectal cancer, and non-small cell lung cancer; while T cells were sorted from the PBMC from the same patient.

Flow cytometry

To perform surface staining, we mixed the appropriate antibodies with the cells at room temperature for 15 minutes and washed them with DPBS (500g, 10 minutes). For intracellular staining, we used the Fixation Permeabilization Kit (BD, 554714) to fix and permeabilize the cells, followed by staining with the appropriate antibodies in the Permeabilization buffer for 30 minutes at 4°C, as previously described.[98] The following antibodies were used: CD66b PerCP-Cy5.5 (Biolegend 305108), CD66b PE (Biolegend 305105), CD66b FITC (Biolegend 305104), HLA-DR BV421 (Biolegend 307636), Osteopontin (SPP1) eFluor660 (Invitrogen 50-9096-41), CXCR2 A488 (Biolegend 320712), CD62L PEcy5 (invitrogen 1946541), CD54 (ICAM1) PE (Biolegend 322708), CD3 APC (Biolegend 300458), CD8a BV785 (Biolegend 301046), CD4 APC/Fire750 (Biolegend 344638), Granzyme B PE/Dazzle594 (Biolegend 372216), IFN-γ BV711 (Biolegend 502539), TNF-α BV650 (BD 563418), 4-1BB (CD137) FITC (eBioscience 11-1379-42), CD69 BV605 (BD 562989), Histone H3 A647 (Cell Signaling 12230S), Acetyl-Histone H3 Lys27 A647 (Cell Signaling 39030S), OVA FITC (sangon D110528), Ly6G PE (Biolegend 127608), Cd74 A488 (Biolegend 151006), Cd74 A647 (Biolegend 151004), Cd45 FITC (TONBO 35-0451-U025), Cd3 A700 (BD 561388), Cd8a BV711 (BD 563046), Cd4 PEcy5 (BD 553050), Cd62L APC (eBioscience 17-0621-83), Cd19 PEcy7 (Biolegend 115519), Cd11b BV395 (BD 563553), Ly6C PerCPCy5.5 (eBioscience 45-5932-82), F4/80 BV785 (Biolegend 123141), Cd279 BV421 (Biolegend 135221), CD11c PEcy5.5 (eBioscience 35-0114-82), CD16 BV711 (Biolegend 302044). Cells were further analyzed using flow cytometry (BD LSRFortessa) and Flowjo software (BD).

PCR array analysis of MHC class I and II antigen presentation genes

We stimulated neutrophils from healthy donors' blood with leucine for 24 hours. Gene expression profiling was carried out using the human MHC class I antigen presentation Gene Expression PCR Array (Wcgene Biotech, Shanghai, China) and human MHC class II antigen presentation Gene Expression PCR Array (Wcgene Biotech, Shanghai, China) following the manufacturer's protocol.

Metabolomics LC-MS analysis and leucine tracing

The Thermo Vanquish ultra-high performance liquid phase system (Thermo Fisher Scientific, USA) equipped with an ACQUITY UPLC® HSS T3 column (2.1×150 mm, 1.8 μm) (Waters, Milford, MA, USA) was utilized. The system operated with a flow rate of 0.25 mL/min, a column temperature of 40 °C, and an injection volume of 2 μL. Mass spectral data was collected using the Thermo Orbitrap Exploris 120 mass spectrometer detector (Thermo Fisher Scientific) with electrospray ionization source (ESI). Both positive and negative ion modes were used for data collection, with a positive ion spray voltage of 3.50 kV and a negative ion spray voltage of -2.50 kV. The sheath gas and auxiliary gas were set to 30 arb and 10 arb, respectively. The primary full scan was performed at a resolution of 60,000 over the m/z range of 100-1000, and HCD was utilized for secondary fragmentation with a collision voltage of 30%. The secondary resolution was set to 15,000. The MS data analysis were conducted following a previously established protocol.[99] Raw MS data were converted to the mzXML format using ProteoWizard software (http://proteowizard.sourceforge.net). Peaks were extracted using R package XCMS (V3.20.0). The peak table and MS2 files in mgf format (converted using ProteoWizard) were uploaded to the MetDNA web server (http://metdna.zhulab.cn/) for metabolite identification. The identifications were assigned levels 1-3 and unknown, following the MSI (Metabolomics Standard Initiative) guidelines. For the tissue samples, 10 scRNA-seq-matched samples (HCC, n=4; NSCLC, n=2; OV, n=3; STAD, n=1) passed QC and was prepared for LC-MS. As for the neutrophils, autologous neutrophils from blood were separated by staining with CD66b Biotin antibody (Biolegend, 305120), added with biotin magnetic beads, sorted with MS columns (Miltenyi Biotec, 130-042-201), and underwent stimulation with leucine for 24 hours.

For ^{13}C leucine tracing, we treated neutrophils with L-Leucine-$^{13}C_6$ (Sigma 605239) for 24 hours following the published protocol.[44] The untreated neutrophils were used as controls. Each condition was performed with 3-4 replicates.

Mitochondrial functional and phenotypic characterization

TMRE (Sigma 87917-25MG), NAO nonyl bromide (Sigma A7847-100MG), Fluo 3 (Sigma 73881-1MG), JC1 (AAT Bioquest 22200), and ROS (AAT Bioquest 16051) were suspended with neutrophils at room temperature for 30min and washed using DPBS (500g, 10 minutes). Cells were further analyzed using flow cytometry (BD LSRFortessa) and Flowjo software (BD). Leica TCS SP5 laser confocal microscope was also used to image neutrophil mitochondria. Each condition was performed with 3 replicates.

Seahorse assays

Autologous neutrophils from blood were separated by staining with CD66b Biotin antibody (Biolegend, 305120), added with biotin magnetic beads, and sorted with MS columns (Miltenyi Biotec, 130-042-201). Post-separation, the neutrophils underwent stimulation with leucine for 24 hours. Cultured plates were used to plate 5×10^5 neutrophils sorted from healthy donors' blood. The neutrophils were then stimulated with leucine for 24 hours, and OCR was measured using an XF24 Seahorse Extracellular Flux Analyzer following the manufacturer's instructions. In the seahorse assays, the neutrophils were treated with oligomycin (0.25 μM), FCCP (0.25 μM), rotenone (0.25 μM), and antimycin A (0.25 μM). Each condition was performed with 3 replicates.

Transmission electron microscopy (TEM)

The neutrophils were fixed in 1% osmium tetroxide in PBS in the dark at room temperature for 2 hours, washed with PBS (pH 7.4) three times for 15 minutes each, and then dehydrated in a series of alcohol concentrations (30%-50%-70%-80%-90%-95%-100%-100%) for 15 minutes each. The cells were then embedded in epoxy resin. The resin blocks were sectioned into ultrathin

sections (60-80 nm) using an ultramicrotome, and collected on 150-mesh copper grids. The grids were stained with 2% uranyl acetate in saturated alcohol solution in the dark for 8 minutes, washed three times with 70% alcohol and three times with ultra-pure water, and then stained with 2.6% lead citrate for 8 minutes. For each treatment group, we performed the TEM for 5 cells. Images were obtained using a SUHT7700 electron microscope (hitachi) and subsequently analyzed using ImageJ Fiji (V2.11.0). In detail, we select the "Straight line" tool and measure the mitochondrial length. The exported length was then analyzed using R.

Confocal imaging

To stain the neutrophils with JC1, we incubated them in a staining solution for 30 minutes at 37°C. After removing the staining solution, we washed the cells with assay buffer to remove any unbound dye. We utilized an Olympus SpinSR10 Ixplore confocal microscope to capture images of the cells. Subsequently, we employed ImageJ Fiji (V2.11.0) software to analyze the images.

Bulk RNA-seq

As for the scRNA-seq-matched samples, sufficient remaining fresh specimens were quickly frozen in liquid nitrogen. As for the neutrophil samples, autologous neutrophils from blood were separated by staining with CD66b Biotin antibody (Biolegend, 305120), added with biotin magnetic beads, and sorted with MS columns (Miltenyi Biotec, 130-042-201). Post-separation, the neutrophils underwent stimulation with leucine for 24 hours. Samples were subjected to RNA extraction using Trizol (Thermo Fisher Scientific, 15596018). Library preparation was performed using NEBNext UltraTM RNA Library Prep Kit (NEB #E7490), followed by library purification using beads (AMPure XP system). Finally, sequencing was conducted using NovaSeq 6000 with PE150. For alignment, the STAR software was employed (https://github.com/alexdobin/STAR). The raw expression levels of each gene (based on fragment counts) were calculated using htseq-count (https://htseq.readthedocs.io/en/release_0.11.1). The selection criteria for significantly differentially expressed genes were: $|\log_2 FC| > 1$ and P-value < 0.05. Neutrophil RNA-seq was performed with 4 replicates. For the immune deconvolution analysis, we use the xCell method.[18] First, xCell includes the most types of T cells among the methods we tested, providing us with a more comprehensive view of the T cell landscape in our samples. Secondly, xCell is one of the most widely used immune cell quantification methods in the field.[18]

H3K27ac, H3K27me3, and H3K4me3 CUT&Tag

Autologous neutrophils from blood were separated by staining with CD66b Biotin antibody (Biolegend, 305120), added with biotin magnetic beads, and sorted with MS columns (Miltenyi Biotec, 130-042-201). Post-separation, the neutrophils underwent stimulation with leucine for 24 hours. After this, procedures of cell permeabilization, antibody incubation, tagmentation, DNA extraction, and sequencing were carried out (Shanghai Jiayin Biotech). For data filtering, the raw reads were processed using Trimmomatic (V0.35, http://www.usadellab.org/cms/?page=trimmomatic). BWA software https://bio-bwa.sourceforge.net/ was used for alignment. Fragment sizes for read pairs were calculated using the BAM file from aligned paired-end sequencing data. The summary statistics on fragment lengths were estimated by sampling several regions, depending on the size of the genome and number of processors. MACS2 (V2.2.7.1, https://pypi.org/project/MACS2/) was used for peak calling in this analysis, Bedtools (V2.30.0, https://bedtools.readthedocs.io/en/latest/) were mainly used for peak annotation analysis.

ATAC-seq

Autologous neutrophils from blood were separated by staining with CD66b Biotin antibody (Biolegend, 305120), added with biotin magnetic beads, and sorted with MS columnsMiltenyi Biotec130-042-201Post-separation, the neutrophils underwent stimulation with leucine for 24 hours. Cell nuclei were subsequently extracted and underwent a transposition reaction via the Tn5 enzyme (Illumina) on 40,000 cell nuclei. Sequencing was performed on an Illumina Novaseq6000using a PE150 sequencing strategy (Shanghai Jiayin Biotech)The raw reads were filtered using Trimmomatic(V0.35, http://www.usadellab.org/cms/?page=trimmomatic)Data alignment was conducted using the BWA softwarehttps://bio-bwa.sourceforge.net/Then the aligned reads in BAM file were used to calculate the fragment sizes for read pairsThe estimation of summary statistics on fragment lengths was done by sampling various regions, with the selection depending on the genome size and number of processorsMACS2(V2.2.7.1, https://pypi.org/project/MACS2/) was used for peak calling in this analysis. Lastly, peak annotation analysis primarily employed Bedtools (V2.30.0, https://bedtools.readthedocs.io/en/latest/).

Spatial transcriptomics

We processed the space ranger output files using Seurat (V4.0.4). The sample information was summarized in Table S5. Afterward, we utilized Seurat's SCTransform function for data normalization, RunPCA function for dimension reduction, and FindNeighbors and FindClusters function for ST spot clustering. To score the cell types, we employed xCell (V1.1.0) and estimated the neutrophil signature using GSVA (V1.40.1).

Neoantigen, T cell, and neutrophil coculture system

Neutrophils were autonomously harvested from the blood of healthy donor through a process involving CD66b Biotin antibody (Biolegend, 305120) staining, the addition of biotin magnetic beads, and sorting using MS columns (Miltenyi Biotec, 130-042-201). Post-harvesting, these neutrophils were stimulated with leucine for 24 hours. Afterward, synthesized peptides were added at a

concentration of 10 μg/ml and the antigen-presenting neutrophils were allowed to uptake and process them for 12 hours. Following this, the neutrophils were cocultured with autologous T cells sorted from PBMC for 24 hours. The following neutralizing antibodies were used: TNFα (sinobiological, 10602-MM0N1), IL-6 (sinobiological, 10395-R508), IL-17 (sinobiological, 12047-M237), IL-23 (sinobiological, CT035-mh066), IFNγ (Selleck A2041). Each condition was performed with 3 replicates.

Reactive T cell response evaluated by TCR-seq

Autologous neutrophils from healthy donors' blood were separated by staining with CD66b Biotin antibody (Biolegend, 305120), added with biotin magnetic beads, and sorted with MS columns (Miltenyi Biotec, 130-042-201). Post-separation, the neutrophils underwent stimulation with leucine for 24 hours. We cocultured the leucine-induced HLA-DR^{+} neutrophils with autologous T cells (negative control: T cell alone, positive control: DCs) and KRAS^{G12V} neoantigen (MTEYKLVVVGAVGVGKSALTIQLI) for 7 days from 4 donors. CD3/CD28 dynabeads were simultaneously added (4:1 to T cells). The T cells were subsequently subjected to TCR-seq. 2 μg of total RNA from each sample was utilized for the preparation of the TCR sequencing library. This process was conducted using the KC-Digital™ Stranded TCR-seq Library Prep Kit (provided by Seqhealth Technology Co., Ltd., Wuhan, China, DT0813-02), in accordance with the manufacturer's guidelines. The library products, with lengths ranging from 250-500 base pairs, were subsequently enriched and quantified. Finally, these samples were sequenced using the NovaSeq platform (Illumina). Sequences during PCR amplification were removed. Subsequently, these sequences were aligned to IMGT by using TRUST4 (https://github.com/liulab-dfci/TRUST4). The data was then analyzed and visualized utilizing the immunarch (V1.0.0, https://immunarch.com/index.html).

Cancer cell, T cell, and neutrophil coculture system

Initially, neutrophils were incubated with leucine for 24 hours. Then, the neutrophils were cocultured with autologous T cells sorted from PBMC for 24 hours. We then add the cancer cell lines (HepG2, A549, HCT116, PANC1, and MCF7) and cultured them together for 48 hours. We finally performed the flow cytometry (PI, AnexinV) to assess the apoptosis level of cancer cells. Cancer cells were gated based on SSC and FSC channels by using Flowjo software (BD). Each condition was performed with 3 replicates.

Mouse model

We obtained 5-week-old male C57BL/6 mice, CD74 KO, CD45.1 mice, and Ly6G$^{Cre\text{-}tdTomato}$ from the Shanghai Model Organisms Center, Inc. MHC-II$^{flox/flox}$ mice, LAT1^{KO}, Bcat2^{KO}, Dbt^{KO} mice were obtained from Nanjing GemPharmatech Co. Ltd. We housed them under pathogen-free conditions with a maximum of five mice per cage. We strictly adhered to animal care principles and ethics and received approval from the Institutional Animal Care and Use Committee of the Shanghai Model Organisms Center (approval number 2019-0011). MC38, Hepa 1-6, and LLC cells (5 × 10^{6}) were injected at day 0 subcutaneously. For the amino acid diet group, 1.5% amino acids were added to the drinking water.[100] As for the PD-1 treatment group, Ultra-LEAF™ Purified anti-mouse CD279 (PD-1) (BioLegend, 135248) were injected intraperitoneally (100μg per mouse), and Ultra-LEAF™ Purified Rat IgG2a, κ Isotype Ctrl (BioLegend, 400565) was used in control groups (100μg per mouse). As for the Ly6G antibody treatment group, mice were injected with 50 μg of anti-Ly6G Ab (BE0075, BioXCell).[101] As for the neutrophil adoptive delivering group, we split neutrophils from the blood of 5-week-old male C57 mice, stimulated the neutrophils with LPS and leucine for 24 h, and injected the neutrophils inside the tumor (5 × 10^{6}). Tumor volume was calculated using the formula length (mm) × width2 (mm) × 0.5. These leucine-treated and control samples were sent for single-cell RNA-seq. In each group of each cancer type, tumors were merged for sequencing. As for the lifetime of neutrophils staying in the tumor microenvironment, we first bear the Cd45.2 C57BL/6 mouse models with MC38, Hepa 1-6, and LLC cells (5 × 10^{6}) subcutaneously. We then delivered neutrophils from Cd45.1 C57BL/6 mice into Cd45.2 C57BL/6 mouse tumors, and assessed the Cd45.1^{+}Ly6G^{+} cells proportion at day 0 to 5. Each condition was performed with 5 replicates.

Patient-derived tumor fragment

We followed a well-established protocol for the processing and preservation of HCC samples treated with neoadjuvant immunotherapy.[62] Tumors were cut into 1–2 mm^{3} pieces and then gradually frozen using a gradient in cryovials containing 1 mL of freezing media (FBS with 10% DMSO). Fragments from different regions of tumor were mixed to reduce heterogeneity. After pathological assessment, samples from 5 patients with pathologic nonresponse (residual viable tumor rates of 95%, 95%, 90%, 90%, and 90% respectively; treatment: anti-PD-1 plus anti-VEGF agent) were selected for further experimentation. The tumor fragments were mixed with ice-cold matrigel (BD Biosciences; Matrix High Concentration, Phenol Red-Free, 4 mg/mL final concentration) and transferred to a 96-well flat-bottom plate. Autologous neutrophils of each patient from blood were separated by staining with CD66b Biotin antibody (Biolegend, 305120), added with biotin magnetic beads, sorted with MS columns (Miltenyi Biotec, 130-042-201), and stimulated with leucine. Autologous antigen-presenting neutrophils were added to the media and cultured for 3 days. Flow cytometry analysis of T cells was then performed. Each condition was performed with 5 replicates.

Web server

We used Apache and Shiny to construct the web server as previously described.[37,102,103] We tested different functions covering common browsers including Chrome, Safari, and IE. Users are not required to register or log in to access features in the web server.

Data visualization

We utilized the following software packages for visualization: Seurat (V4.0.4), ggplot2 (V3.3.5), dittoSeq (V1.5.2), ggrepel (V0.9.1), ggpubr (V0.4.0), ggsignif (V0.6.3), pheatmap (V1.0.12), ComplexHeatmap (V2.15.1), and cowplot (V1.1.1) in R, as well as sctour (V0.1.3) and TooManyCells (V3.0.0) in Python.

QUANTIFICATION AND STATISTICAL ANALYSIS

We defined statistical significance as $P < 0.05$ and performed all statistical analyses using R (V4.1.0) and RStudio ("Elsbeth Geranium" Release). Group comparisons were conducted using Student's t-tests, Wilcoxon rank-sum tests, and ANOVA, while paired t-tests were utilized for paired comparisons. Unless otherwise specified, bar plots were presented as mean± standard deviation. Each experiment was repeated three or more times using biologically independent samples. For correlation analyses, we used Spearman rho or Pearson r. Survival analyses were performed using log-rank tests and the proportion of HLA-DR$^+$CD15$^+$ neutrophils of CD15$^+$ neutrophils and SPP1$^+$CD15$^+$ neutrophils of CD15$^+$ neutrophils were used for analysis. We utilized the ggsurvplot function in the R package survminer (V0.4.9) to determine the cutoff value of proportion and generate Kaplan-Meier survival curves.

CellPress

Supplemental figures

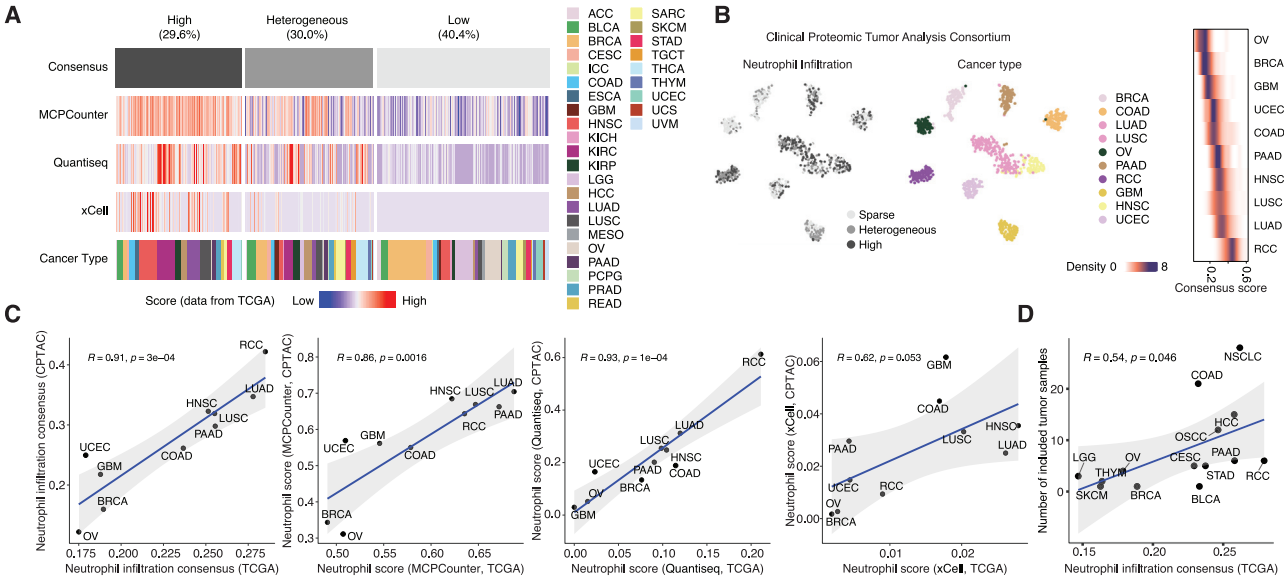

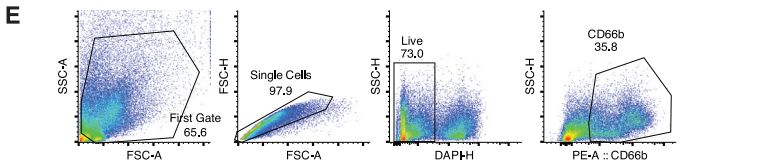

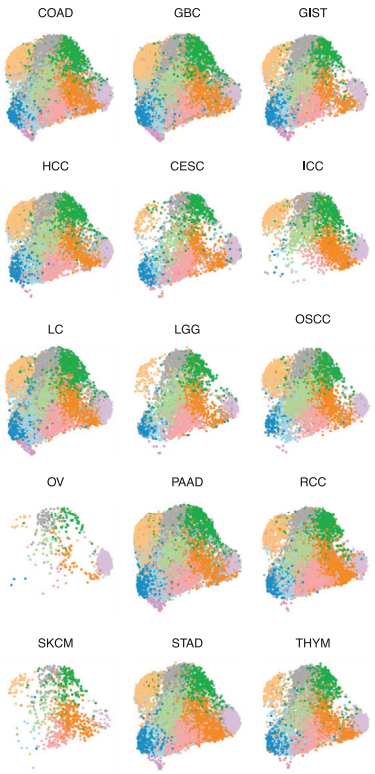

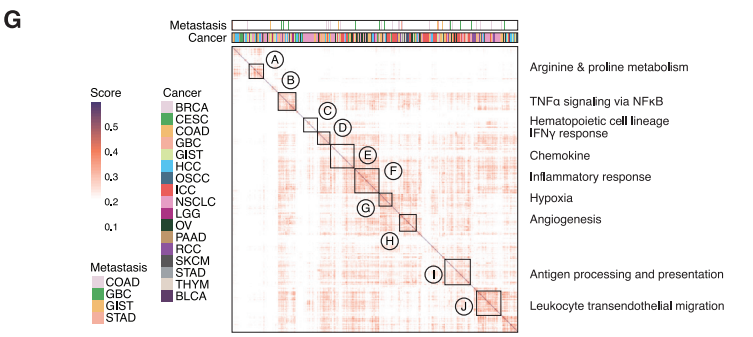

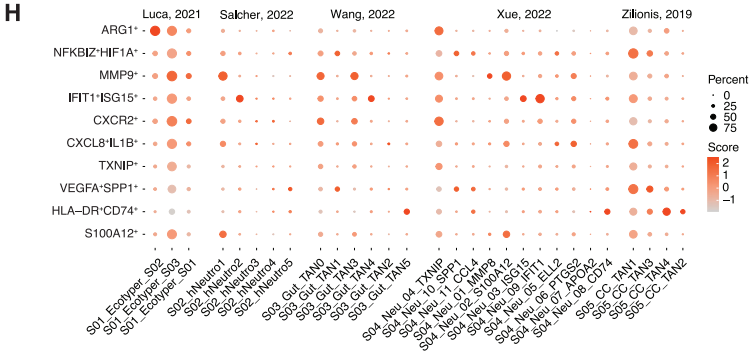

(legend on next page)

Figure S1. Pan-cancer single neutrophil generation, sampling strategy, and program decoding, related to Figure 1

(A) Neutrophil infiltration level of pan-cancer samples from TCGA dataset. n = 8,766. See Table S1 for cancer type abbreviation.

(B) Validation of neutrophil infiltration level of pan-cancer samples from CPTAC dataset. n = 1,033. See Table S1 for cancer type abbreviation. The left panel represents the neutrophil infiltration across pan-cancer samples. The middle panel represents the cancer types. The right panel represents the ranked neutrophil infiltration consensus score across pan-cancer.

(C) Correlation between neutrophil infiltration levels in two cohorts (TCGA and CPTAC). The x axis and y axis represent the mean neutrophil infiltration level in TCGA and CPTAC data by using neutrophil infiltration consensus, MCPCounter neutrophil score, Quantiseq neutrophil score, and xCell neutrophil score, respectively.

(D) Correlation between neutrophil infiltration levels between the number of included tumor samples in our study and TCGA data. The x axis represents the median neutrophil infiltration level in TCGA data. The y axis represents the included patients in our study.

(E) Neutrophil gating strategy of flow cytometry sorting.

(F) UMAP plots of neutrophil subsets from different cancer types. The color represents each neutrophil subset. Cancer types with neutrophils lower than 500 were removed for visualization.

(G) Neutrophil transcriptional programs by using NMF (see STAR Methods). The upper panel represents the metastasis status and cancer types. The color represents the correlation value of each program. The right text represents the enriched terms for each program.

(H) Comparison between neutrophil subsets in this study with published human neutrophil states.[7,22–25]

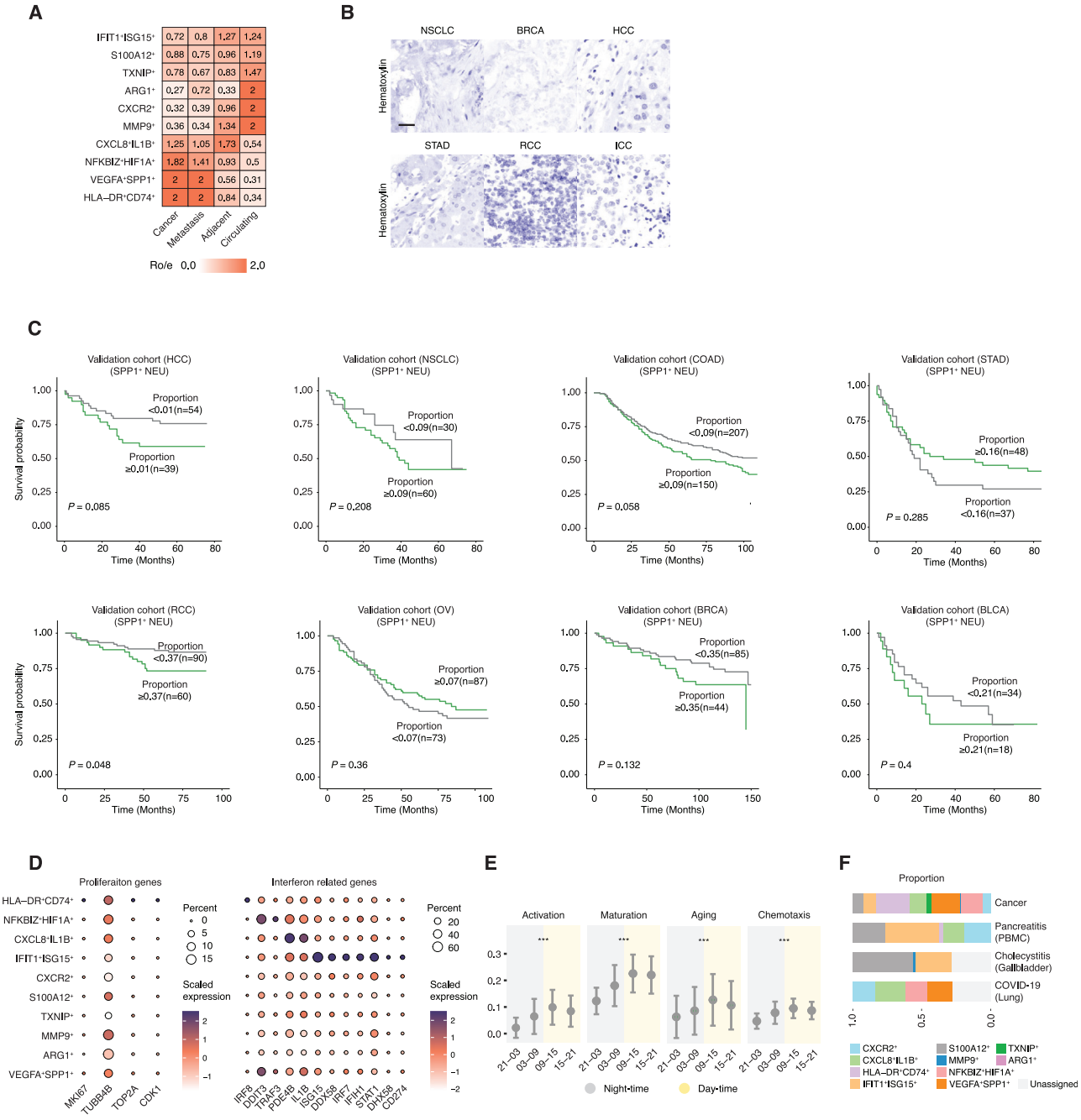

Figure S2. Transcriptome features of neutrophil subsets, related to Figure 2

(A) Neutrophil subset infiltration level of different sample types. The color represents the Ro/e (ratio of observed cell number to expected cell number). Larger Ro/e value means increased infiltration. Ro/e values larger than two were normalized to two.

(B) Matched hematoxylin staining regions as shown in Figure 2D in NSCLC, BRCA, and HCC (HLA-DR$^+$ neutrophil enriched cancer types) with STAD, RCC, and ICC (SPP1$^+$ neutrophil enriched cancer types). Scale bars, 30 μm.

(C) Validation of the prognostic value of SPP1$^+$CD15$^+$ neutrophils in COAD, NSCLC, HCC, STAD, RCC, OV, BRCA, and BLCA quantified by mIHC in 8-cancer-TMA cohort. The cutoff value of SPP1$^+$CD15$^+$ to CD15$^+$ neutrophil proportion was determined by R package survival and survminer, and p value was determined by log-rank test.

(D) Expression profile of differentially expressed proliferation genes and interferon-related genes among neutrophil subsets.

(E) Circadian profile of neutrophil-related signatures according to sampling time. The signature was from the GO and KEGG gene set databases (STAR Methods). ***p < 0.001; Wilcox test.

(F) The proportion of neutrophil subsets within cancer, pancreatitis, cholecystitis, and COVID-19 samples.

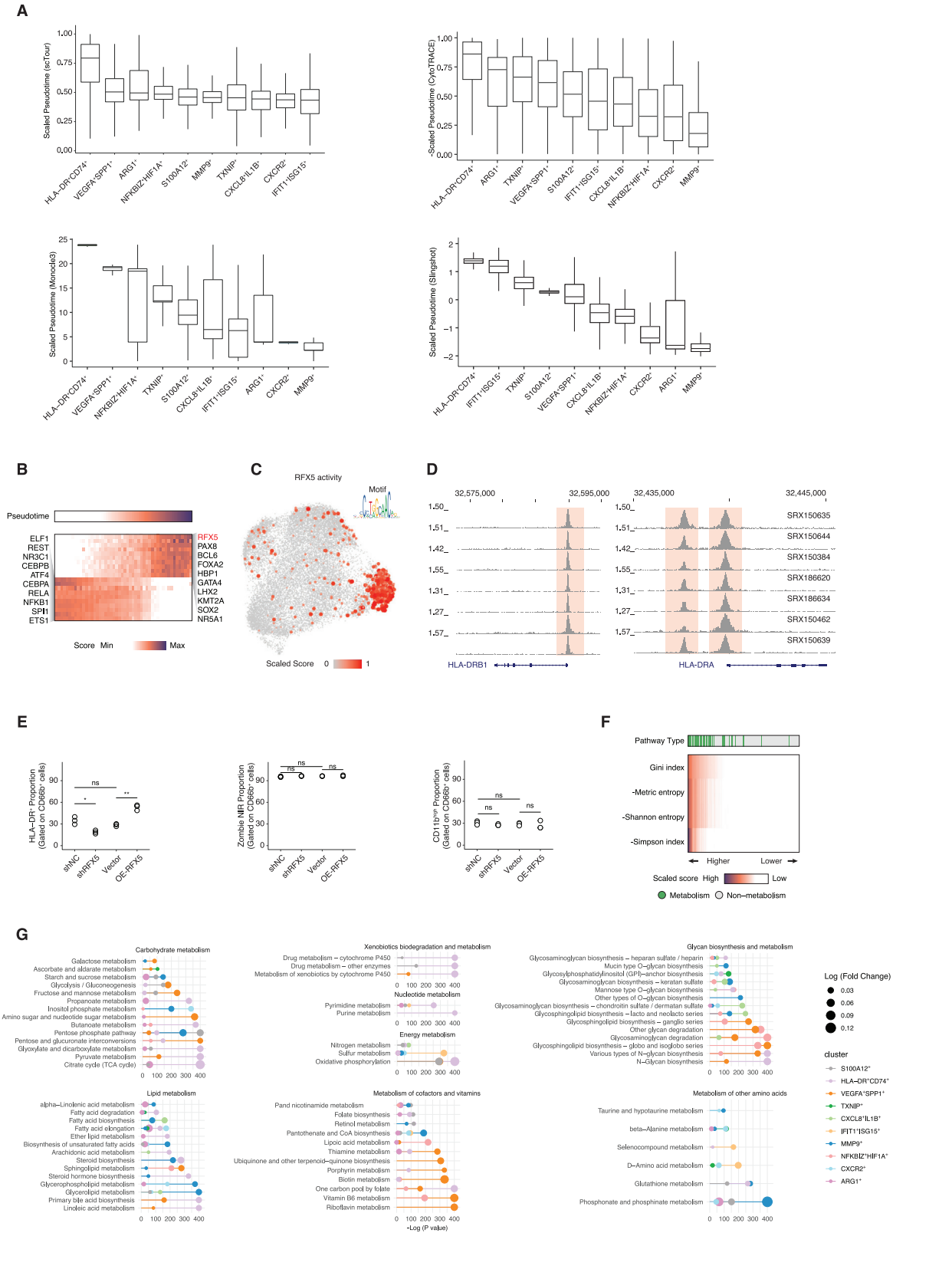

(legend on next page)

Figure S3. Terminal differentiated HLA-DR$^+$ neutrophils, its transcription factor RFX5, and metabolic features, related to Figure 3

(A) Pseudotime estimated by scTour, CytoTRACE, monocle3, and Slingshot of single neutrophils according to neutrophil subsets.

(B) Transcription factor activity associated with pseudotime showing RFX5 as a potential transcription factor in HLA-DR$^+$ neutrophils.

(C) UMAP plot of RFX5 activity and its binding motif in neutrophils based on our scRNA-seq data. The size and color represent the value of the RFX5 activity score.

(D) RFX5 binding intensity around HLA-DRA and HLA-DRB1 locus. The data source was marked on the right panel of the plot. The y axis represents the ChIP-seq intensity of DNA binding of RFX5.

(E) Flow cytometry intensity of HLA-DR, Zombie NIR, and CD11b^{high} cells based on RFX5 status in neutrophil cell line dHL-60. n = 3. ns, not significant, *$p < 0.05$, **$p < 0.01$; Student's t test.

(F) Pathway activity of neutrophil subsets based on our scRNA-seq data showed metabolic pathway ranked higher among all pathways.

(G) Carbohydrate metabolism pathway, xenobiotics biodegradation and metabolism pathway, nucleotide metabolism pathway, energy metabolism pathway, glycan biosynthesis and metabolism, lipid metabolism pathway, cofactors and vitamin metabolism pathway, and other amino acid metabolism activity of neutrophil subsets. The dot size represents the log (fold change) of each neutrophil subset compared with the remaining cells. The y axis represents the log (p value) of each neutrophil subset compared with the remaining cells. The color represents different neutrophil subsets. The metabolic pathway activity was determined by scMetabolism[37] (parameter: imputation = T, metabolism.type = "KEGG").

See Table S3 for metabolic pathway data.

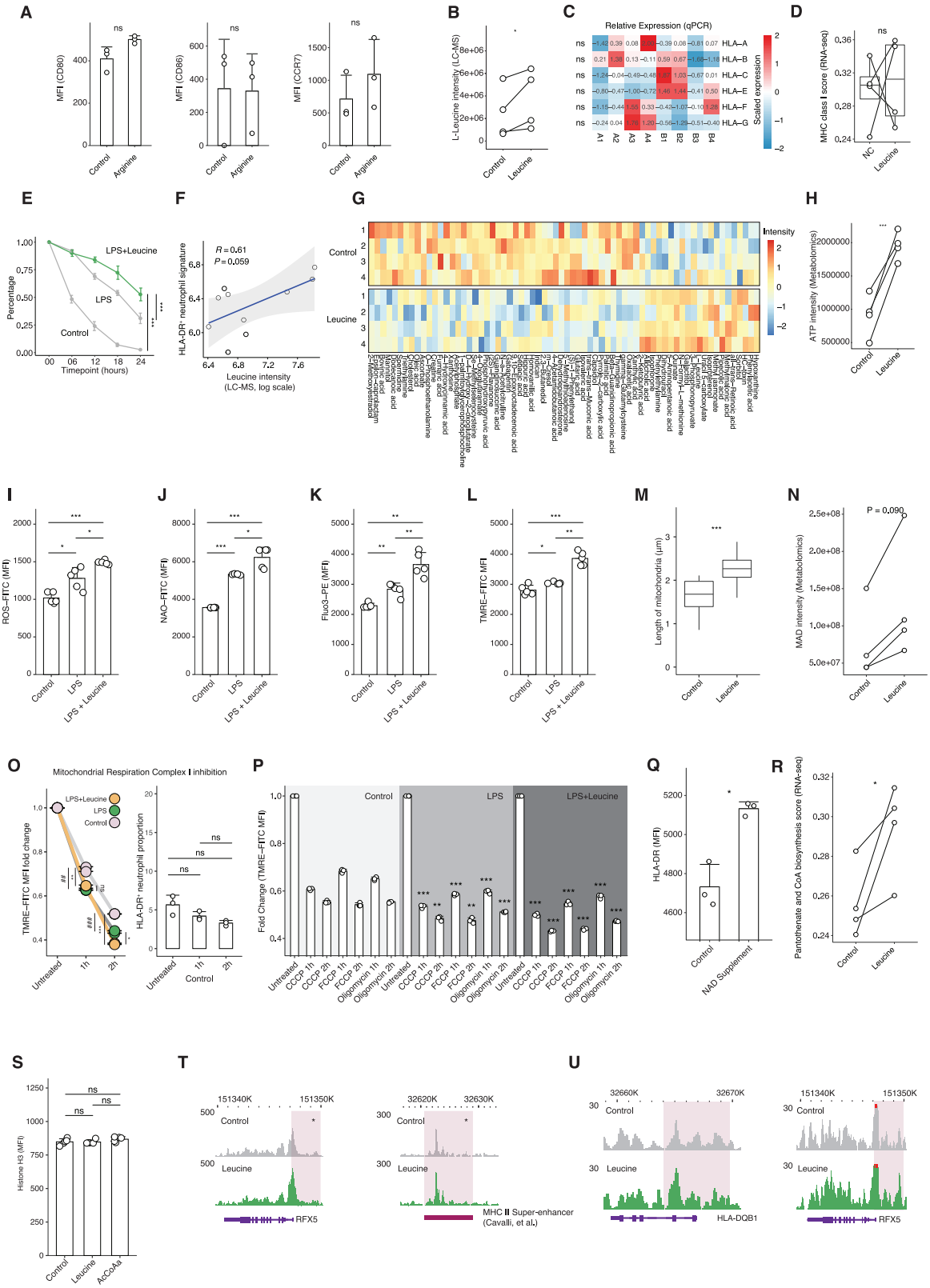

(legend on next page)

Figure S4. Leucine upregulates HLA-DR in neutrophils through the acetyl-CoA/H3K27ac/MHC-II axis, related to Figure 4

(A) MFI of CD80, CD86, and CCR7 between arginine-treated neutrophils and control group. Neutrophils were sorted from healthy donors' blood. The bar plot is mean ± standard deviation. n = 3.

(B) Leucine intensity of leucine-treated neutrophils and control group determined by LC-MS. n = 4.

(C) Relative RNA expression of MHC-I genes (HLA-A, HLA-B, HLA-C, HLA-E, HLA-F, and HLA-G) based on PCR array. HLA-D was not detected and was hence excluded for the analysis. n = 4.

(D) Signature of MHC class I based on RNA-seq of leucine treated and control group. The signature was from GO gene set database (STAR Methods). n = 4.

(E) Live neutrophil rate according to culture time. n = 3.

(F) Correlation between leucine intensity and HLA-DR$^+$ neutrophil signature of matched tumor samples (HCC, n = 4; NSCLC, n = 2; OV, n = 3; STAD, n = 1). The leucine intensity was evaluated by LC-MS from matched samples and was log scaled. n = 10. Pearson R was calculated to evaluate the correlation.

(G) Differential metabolite analysis of leucine-treated neutrophils and control group. n = 4. See Table S4 for the exact metabolite intensity.

(H) ATP intensity of leucine treatment and control group. n = 4.

(I) Mitochondrial ROS MFI of leucine treatment, lipopolysaccharides (LPS), and control groups. n = 5.

(J) Mitochondrial quality (NAO) MFI of leucine treatment, LPS, and control groups. n = 5.

(K) Mitochondrial Ca^+ (Fluo3) MFI of leucine treatment, LPS, and control groups. n = 5.

(L) Mitochondrial membrane potential comparison between leucine-treated neutrophils and control group. n = 5.

(M) Comparison of mitochondria length between leucine-treated neutrophils and control groups. The length was measured by transmission electron microscopy and calculated with ImageJ analysis.

(N) Comparison of NAD intensity between leucine-treated neutrophils and control group. n = 3.

(O) Left panel: MFI of mitochondrial membrane potential (TMRE) according to mitochondrial respiration complex I inhibition (untreated, 1 h, and 2 h). Right panel: HLA-DR$^+$ neutrophil proportion according to mitochondrial respiration complex I inhibition in each group (untreated, 1 h, and 2 h). n = 3.

(P) Fold change of mitochondrial membrane potential (TMRE) MFI upon mitochondrial respiration complex inhibition including carbonyl cyanide m-chlorophenylhydrazone (CCCP), oligomycin, and carbonyl cyanide 4-(trifluoromethoxy)phenylhydrazone (FCCP). n = 3.

(Q) HLA-DR MFI between NAD-supplemented neutrophils and control group. n = 3.

(R) Signature of pantothenate and CoA biosynthesis based on RNA-seq data in leucine treated and control group. The signature was from the KEGG database. n = 4.

(S) Histone H3 MFI of leucine treatment, acetyl-CoA activation, and control groups. n = 5.

(T) H3K27ac modification on transcription factor RFX5 locus and MHC-II super-enhancer locus of leucine and control groups. n = 3. Replicates were merged for visualization.

(U) Chromatin accessibility on HLA-DQB1 and transcription factor RFX5 locus of leucine and control groups. The chromatin accessibility was determined by ATAC-seq.

Data in the bar plots are presented as mean ± standard deviation (A, I–L, O–Q, and S) and mean ± standard error (E). ns, not significant, *$p < 0.05$, ## and **$p < 0.01$, ### and ***$p < 0.001$; Student's t test (A, C, E, I–M, O, P, Q, and S), paired Student's t test (B, D, H, N, and R), and Wilcox test (T).

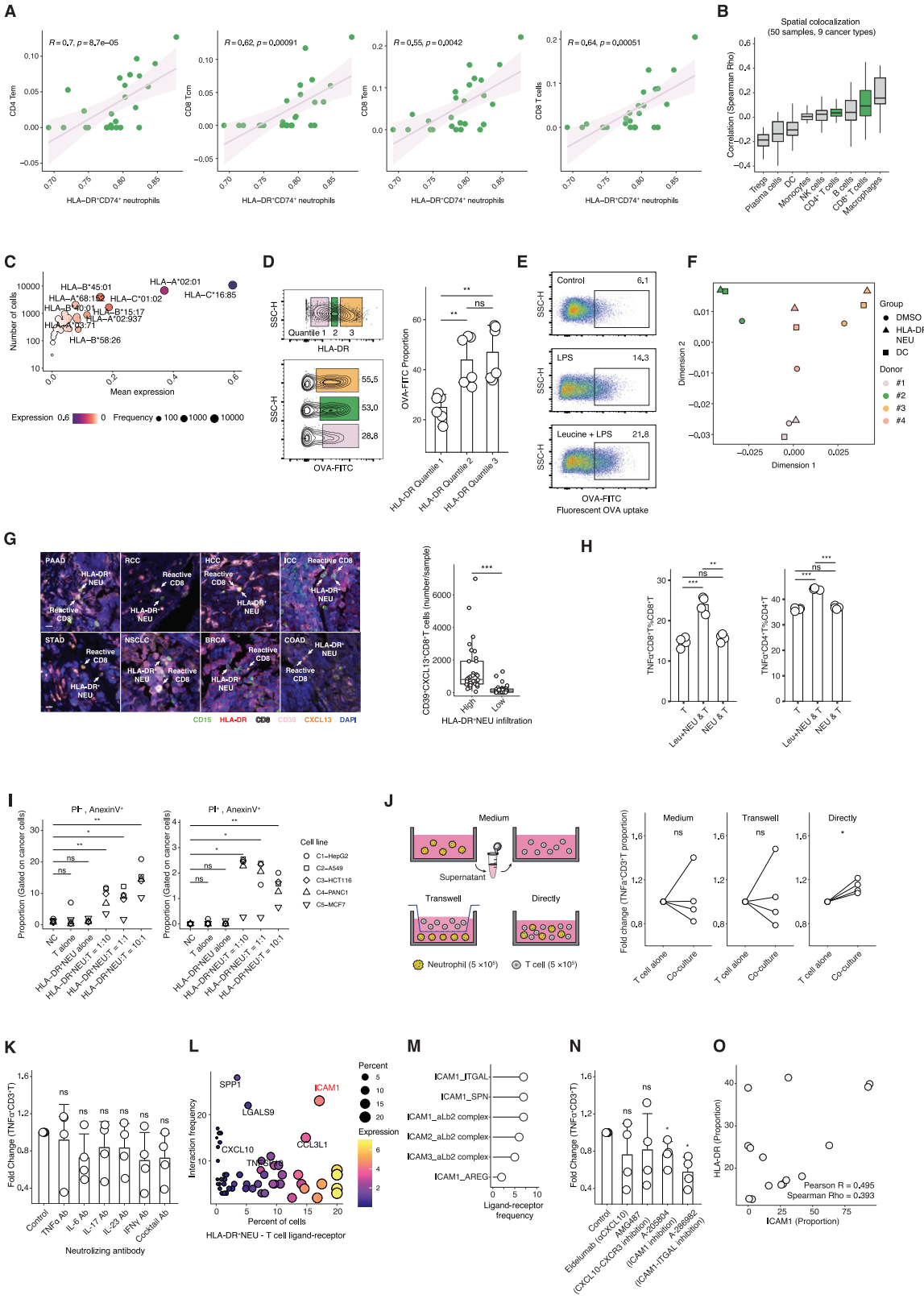

(legend on next page)

Figure S5. HLA-DR$^+$ neutrophils link with T cell infiltration and stimulate T cells, related to Figure 5

(A) Correlation between HLA-DR$^+$ neutrophil signature and CD4$^+$ T effector memory (em), CD8$^+$ T central memory (cm), CD8$^+$ Tem, and CD8$^+$ T cell signature. The signature score was estimated using xCell (STAR Methods) based on the RNA-seq of matched samples. The signature was estimated by xCell algorithm (STAR Methods).

(B) Spatial co-localization between HLA-DR$^+$ neutrophil signature and other major immune lineages. Data sources and accession were summarized in Table S5.

(C) MHC-I allele quantification of tumor-infiltrating neutrophils based on scRNA-seq data. The analysis pipeline was summarized in STAR Methods. The x axis represents the mean expression of MHC-I molecules. The y axis represents the number of cells.

(D) Fluorescent (FITC)-labeled OVA positive cells among HLA-DR low, HLA-DR medium, and HLA-DR high neutrophils. Neutrophils were sorted from healthy donors' blood. n = 6.

(E) Fluorescent (FITC)-labeled OVA positive cells among HLA-DR low, HLA-DR medium, and HLA-DR high neutrophils. Neutrophils were sorted from healthy donors' blood.

(F) Dimension reduction analysis of TCR repertoire of T cells stimulated by HLA-DR$^+$ neutrophils or DCs fed with neoantigens of *KRAS*^{G12V} (MTEYKLVVVGAVGVGKSALTIQLI). The TCR was performed on the T cells in the coculture system.

(G) Association between HLA-DR$^+$ neutrophils and reactive CD8 T cells estimated by mIHC. The left panel represents the representative mIHC images of HLA-DR$^+$ neutrophils (HLA-DR$^+$CD15$^+$ cells) and reactive CD8 T cell responses (CXCL13$^+$CD39$^+$CD8$^+$ cells) in multi-cancer-TMA cohort covering 8 cancer types. Scale bars, 30 μm. The right panel represents the number of CD39$^+$CXCL13$^+$CD8$^+$T cells among HLA-DR$^+$ neutrophil high/low samples. n = 62. Samples with low-quality mIHC were excluded.

(H) T cell cytotoxicity (TNFα intensity) when cocultured with leucine-treated neutrophils, untreated neutrophils, and negative control without antigen. Autologous neutrophils and T cells were sorted from healthy donors' blood. n = 3.

(I) The apoptosis of cancer cell lines induced by HLA-DR$^+$ neutrophil-activated T cells. Neutrophils and T cells were sorted from healthy donors' blood.

(J) T cell cytotoxicity (TNFα intensity) when cocultured with HLA-DR$^+$ neutrophils in different coculture methods, including medium, transwell, and direct coculture. Neutrophils and T cells were sorted from healthy donors' blood. n = 4.

(K) The proportion of TNFα$^+$CD3$^+$T cells cocultured with HLA-DR$^+$ neutrophils when treated with TNFα, IL-6, IL-17, IL-23, and IFNγ neutralizing antibodies, cocktail neutralizing antibodies, and control. Neutrophils and T cells were sorted from healthy donors' blood. n = 4.

(L) HLA-DR$^+$ neutrophils and T cell ligand-receptor analysis inferred from scRNA-seq data. The ligand-receptor results were generated by using CellPhoneDB (STAR Methods).

(M) Ligand-receptor analysis of ICAM gene family inferred from scRNA-seq data.

(N) T cell cytotoxicity (TNFα intensity) in HLA-DR$^+$ neutrophil coculture system when inhibiting the ligand-receptor interaction of CXCL10 or ICAM1. Neutrophils and T cells were sorted from healthy donors' blood. n = 4.

(O) Correlation between HLA-DR$^+$ neutrophil proportion and ICAM1$^+$ neutrophil proportion examined by flow cytometry. The correlation analysis was evaluated by Spearman-Rho and Pearson R analysis.

Data in the bar plots are presented as mean ± standard deviation (D, H, K, and N). ns, not significant, *$p < 0.05$, **$p < 0.01$, ***$p < 0.001$; Student's t test (D–E, G–I, K, N), paired Student's t test (J).

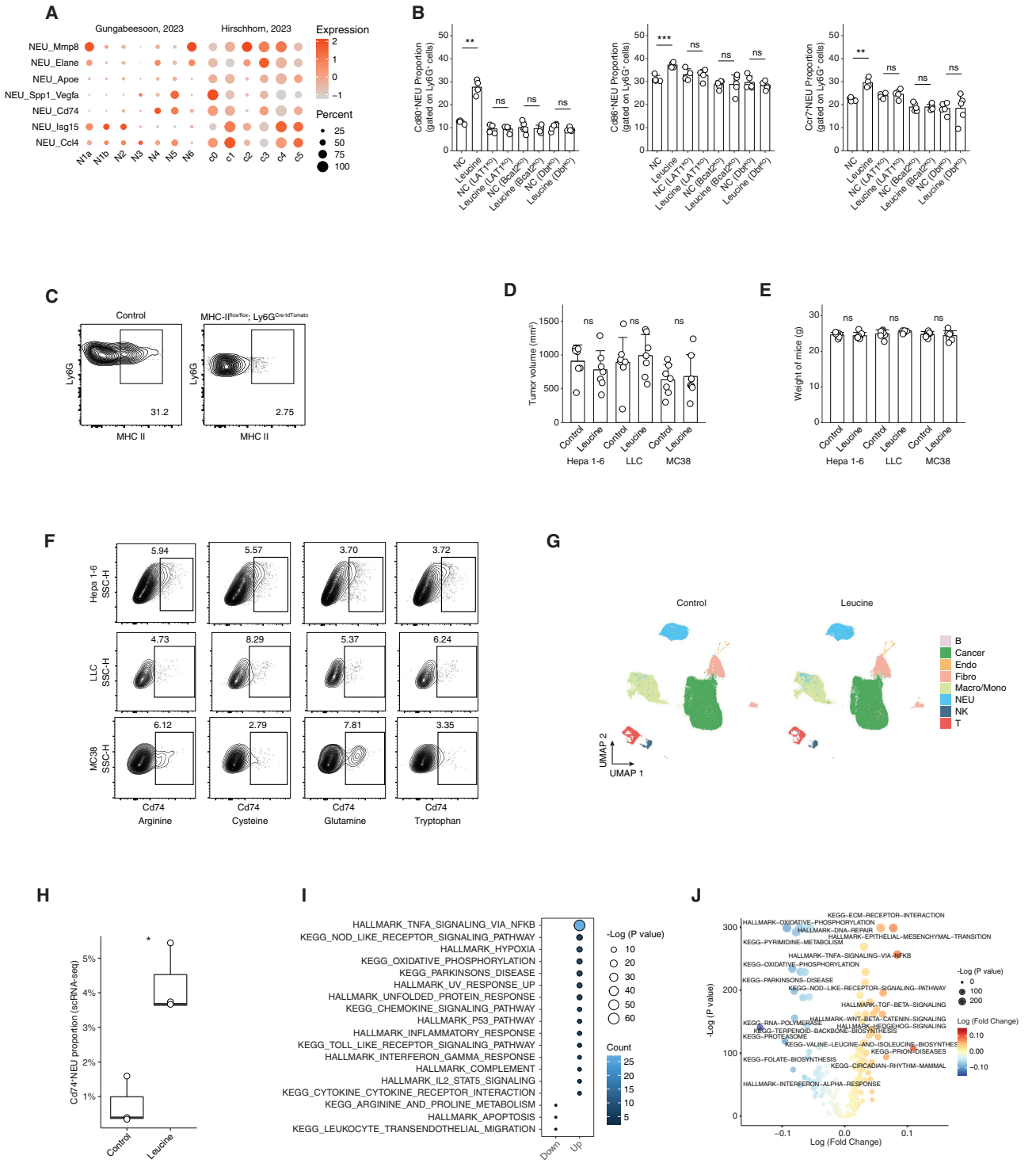

Figure S6. Leucine diet reprograms tumor microenvironment and associates with altered T cell response *in vivo*, related to Figure 6

(A) Comparison between neutrophil subsets in this study with published mouse neutrophil states.[11,14]

(B) Cd80^{+}, Cd86^{+}, and Ccr7^{+} neutrophil proportion between leucine treated and control neutrophils from blood of LAT1^{KO}, Bcat2^{KO}, Dbt^{KO}, and wild-type mice. The bar plot is mean ± standard deviation. ns, not significant, $^{**}p < 0.01$, $^{***}p < 0.001$; Student's t test.

(C) MHC-II intensity on intratumor neutrophils from the MHC-II$^{flox/flox}$; Ly6G$^{Cre\text{-}tdTomato}$ mice and wild-type mice.

(D) Tumor volume from leucine diet and control group in LLC, MC38, and Hepa 1–6 bearing mice. ns, not significant; Student's t test. The samples were collected on day 12.

(legend continued on next page)

(E) The weight of mice from the leucine diet and control group in LLC, MC38, and Hepa 1–6 bearing mice. ns, not significant; Student's t test. The samples were collected on day 12.
(F) Flow cytometry of Cd74 in tumor-infiltrating neutrophils from mouse models (LLC, MC38, and Hepa 1–6 bearing mice) fed with each amino acid (arginine, cysteine, glutamine, and tryptophan) diet. The samples were collected on day 12.
(G) UMAP plot and cell proportion based on scRNA-seq data from leucine diet and control group. The samples were collected on day 12.
(H) Proportion of $Cd74^{+}$ neutrophils among all neutrophils based on scRNA-seq data from leucine diet and control group in LLC, MC38, and Hepa 1–6 bearing mice. *$p < 0.05$; Student's t test. The samples were collected on day 12.
(I) Pathway enrichment analysis of differentially expressed genes of neutrophil between leucine diet and negative control based on scRNA-seq data. The size of dot represents the log (p value).
(J) Cancer cell signature comparison between leucine diet and control group based on scRNA-seq data in LLC, MC38, and Hepa 1–6 bearing mice. The signature was from the cancer hallmark gene set database.

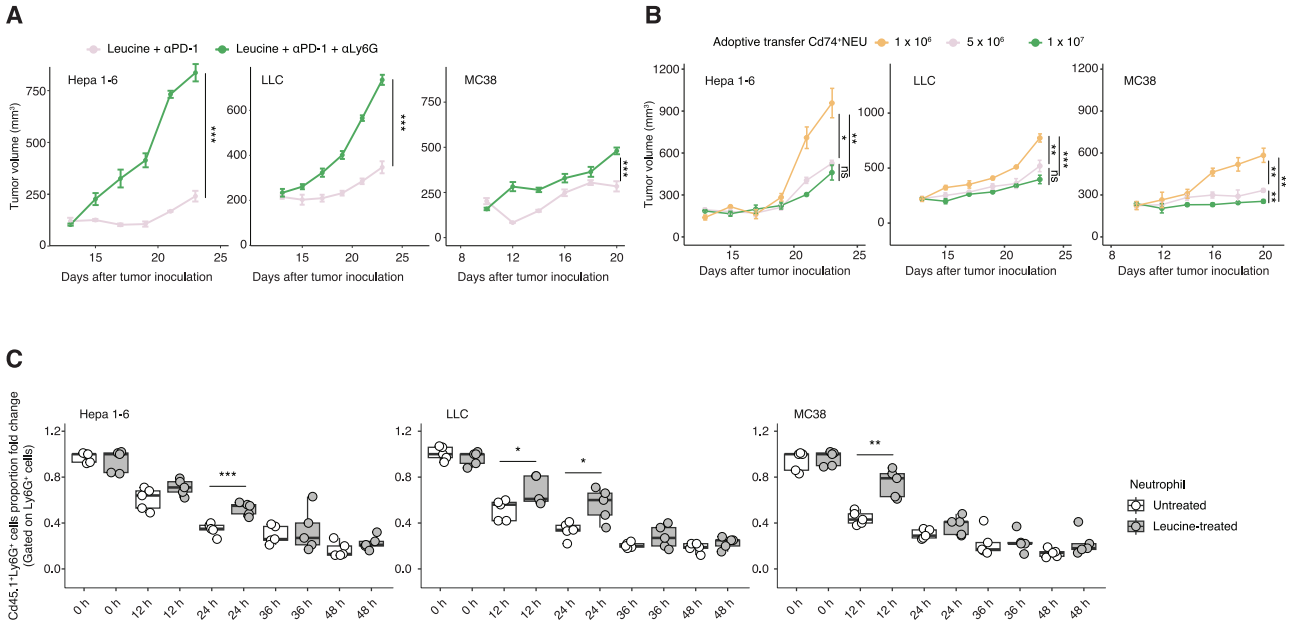

Figure S7. The therapeutic value of antigen-presenting neutrophils, related to Figure 7

(A) Comparison of tumor volume between leucine + PD-1 antibody group and leucine + PD-1 antibody + Ly6G antibody group. n = 5. ***p < 0.001; Student's t test.

(B) Comparison of tumor volume of adoptive transferring $Cd74^+$ neutrophils at different cell numbers (1×10^6, 5×10^6, and 1×10^7). n = 5. ns, not significant, *p < 0.05, **p < 0.01, ***p < 0.001; Student's t test.

(C) $Cd45.1^+Ly6G^+$ cell proportion of $Ly6G^+$ cells by delivering leucine-treated and untreated $Cd45.1^+$ neutrophils into Cd45.2 mouse tumors at different time points (0, 12, 24, 36, and 48 h). n = 5. *p < 0.05, **p < 0.01, ***p < 0.001; Student's t test.